Multi-Modal Approach to Localizing Sources in the Human Brain

by
Kevin S. Whittingstall

Submitted in partial fulfillment of the
requirements for the degree of
Doctor of Philosophy

at

Dalhousie University
Halifax, Nova Scotia
December 5, 2005

Your file Votre référence
ISBN: 978-0-494-16720-5
Our file Notre référence
ISBN: 978-0-494-16720-5

DALHOUSIE UNIVERSITY

To comply with the Canadian Privacy Act the National Library of Canada has requested that the following pages be removed from this copy of the thesis:

Preliminary Pages

Examiners Signature Page (pii)

Dalhousie Library Copyright Agreement (piii)

Appendices

Copyright Releases (if applicable)

Pour ma belle maman

and dedicated to my dear dad

Table of Contents

List of Tables

List of Figures

Abstract

In the past 20 years, research in brain functionality has substantially increased. Tools such as the electroencephalogram (EEG) and functional magnetic resonance imaging (FMRI) have made it possible to non-invasively measure brain function. The temporal resolution of EEG is superior to that of FMRI, and it is generally believed that the spatial resolution of FMRI is superior to that of the EEG. The combination of these two modalities in neuroimaging studies is therefore important, as it may provide complimentary information regarding brain function. Although EEG and FMRI are sensitive to very different physiological phenomena (synaptic and hemodynamic events, respectively) the exact relationship between the sources of EEG and FMRI remains unknown. This raises an important question: is EEG blind to events detected by FMRI or vice-versa? It is anticipated that a better understanding of this relationship will lend additional insight into brain function.

The focus of this thesis is to study the relationship between the sources of EEG and FMRI. This was done by making two sets of visual evoked potential (VEP) and FMRI measurements on healthy participants, and one set of VEP/FMRI measurements on patients with uni-lateral glaucoma. The results from the first set of VEP/FMRI measurements show that the location of the N75 VEP source is near the positive FMRI response (**+BOLD**), while the P100 source is near the negative FMRI response (**-BOLD**). In the second set of VEP measurements, we show that the location of the N75 and **+BOLD** source are more sensitive to changes in stimulus position than the P100 and **-BOLD** source. In the final set of measurements, the results show that both VEP & FMRI are sensitive to visual field impairment brought on by glaucoma. It is also shown that the N75 component of the VEP and the **+BOLD** response of FMRI are the best markers for identifying the effects of glaucoma in the visual cortex. Taken together, the results from this thesis show that there exists a strong relationship between the sources that elicit the VEP and FMRI responses.

List of Symbols and Abbreviations

au	MRI signal, arbitrary units
EEG	Electroencephalogram
FMRI	Functional Magnetic Resonance Imaging
PSP	Postsynaptic Potential
EPSP	Excitatory Postsynaptic Potential
IPSP	Inhibitory Postsynaptic Potential
GABA	Gamma-Amino Butyric Acid
j^p	Primary Current
j^v	Secondary Current
$J(r)$	Current Density
$E(r)$	Electric Field
σ	Conductivity
Φ	Electric Potential
∇	Gradient Operator
ERP	Event Related Potential
VEP	Visual Evoked Potential
SNR	Signal to Noise Ratio
NMR	Nuclear Magnetic Resonance
S	Angular Momentum
I	Quantum Number
$\hbar$	Planks Constant/2π
γ	Gyromagnetic Ratio
μ_s	Magnetic Moment
B	Magnetic Field
K	Boltzmans Constant
T	Temperature
τ	Torque
ω	Larmor Frequency

$T1$	Spin-lattice Relaxation Time
$T2$	Spin-spin Relaxation Time
M	Net Magnetization
τ_c	Correlation Time
G	Gradient Magnetic Field
$T2^*$	Spin-spin Relaxation Time
χ	Magnetic Susceptibility
H	Total Magnetic Field
μ	Permeability
Hb	Oxyhemoglobin
dHb	Deoxyhemoglobin
BOLD	Blood Oxygenation Level Dependence
+BOLD	Positive BOLD Response
-BOLD	Negative BOLD Response
EFP	Extracellular Field Potential
LFP	Local Field Potential
LGN	Lateral Geniculate Nucleus
COA	Center of Activity
PAL	Pre-auricular Left
PAR	Pre-auricular Right
NAS	Nasion
ROI	Region of Interest
CC	Correlation Coefficient
EPI	Echoplanar Imaging
CG	Capsular Glaucoma
MD	Mean Deviation
CAG	Closed Angle Glaucoma
IOP	Intraocular Pressure

Acknowledgements

I would first and foremost like to thank my mentor and dear friend, Gerhard Stroink. I owe much of my success, both in and outside of the Physics department to your wisdom, patience and dedication. Thank you so very much.

Thanks to Dr. Ryan d'Arcy, Dr. John Conolly and Dr. Michael Hale for their helpful suggestions.

Thanks to Dr. Michael Noseworthy, Dr. Matthias Schmidt, Dr. Balwantray Chauhan, Dr. Marcelo Nicolela, Dr. David Clarke, Ron Hill, Dr. Gail Eskes, Jim Chisholm & Anne-Marie Jeffrey for their support and assistance.

This thesis was a mixture of hard work, luck and the invaluable support I received from many people:

To Connie, for making me a very proud & lucky brother. To gran, gramps & grandmaman, for remaining so close while being so far away. To my army of wonderful aunts, uncles and cousins, merci pour votre support. To Matt, for taking some time out of your life in order to help rebuild mine. To Mike, for our lunch hour breakfast sessions. To Andrew, for your devotion to the 80's movement. To Shane, enough said. To Jeremy, for your enthU2siasm. To Joyia, for all the coffee breaks. To Doug & Christine, for all the help in making this thesis possible. To the MRI guys: Mark, Greg and Matt, thanks for being so good at what you do. To the lovely Catherine, for your very much appreciated thesis-writing interruptions. To Meredith, for all the 'slices'. To Tom's Little Havana, for making this thesis last much longer than it should have. To Kiwi, for listening...over, and over again. To Morgs & Ali, thanks for all the support & food. To Janie, for being the greatest Cape Bretoner I've ever known. To Jack & Terry, for our annual run-ins. To Kate, for all the showbiz gossip. To Rob-O, for all of our business lunches. To Wojciech and Amy, for their eternal love and support. To Rob and Mandy, for constantly reminding me of how great it is knowing the both of you. To Cory and Amy, for all the laughs and epic croquet battles. To my Richmond crew, for making it interesting every time I come home. And finally, to my 7^{th} grade math teacher, Mr. M^{c}Gee: Thanks.

Chapter 1

Introduction

Since its discovery in the early 1990's, Functional Magnetic Resonance Imaging (FMRI) has dramatically changed the way in which the human brain is studied. Its non-invasive nature has made it possible to localize centers of brain function without the need of surgery. FMRI has therefore become one of the more frequently used functional neuroimaging tools, leaving behind other modalities such as Positron Emission Tomography (PET) and Electroencephalography (EEG). However, there remain limitations to FMRI that reduce its role as a routine clinical tool. The temporal resolution of FMRI is low compared to that of the EEG, and therefore makes it difficult for FMRI to capture fast transient neural activity (such as interictal spikes associated with Epilepsy). It is reasonable to assume that with increasing technical advances, the temporal resolution of FMRI may improve and perhaps become comparable to EEG. However, there are several questions regarding FMRI that still remain elusive. One fundamental question is: What precisely does the FMRI signal reflect? Even with the recent surge in integrative EEG/FMRI studies, the manner in which the sources detected by these two modalities are related remains unknown. Moreover, it may be possible that activity measured by one modality is not detectable by the other. The purpose of this work is to address the sensitivity of these two modalities to brain activity, and to show that both FMRI and EEG are needed to accurately study brain dynamics.

This thesis begins by comparing the locations of the N75 and P100 VEP components with the locations of the peak positive and negative FMRI responses. From there, we study how these VEP and FMRI sources respond under different visual stimulus conditions. We then implement VEP and FMRI measurements in a clinical setting by observing whether or not these modalities are sensitive to visual impairment in four patients with uni-lateral glaucoma.

Chapter 2

Theory

2.1 Introduction

Electroencephalography (EEG) and Functional Magnetic Resonance Imaging (FMRI) are two commonly used methods for indirectly studying neural activity in the brain. These modalities are sensitive to different physiological processes, and the exact nature of how their calculated sources of activity are related remains unknown. In order to fully explore this so-called neurovascular relationship, it is necessary to review the general mechanisms from which these two signals originate. An overview of the literature devoted to the relationship between neural and hemodynamic activity is presented at the end of the chapter.

2.2 Origin of electrical activity in the human brain

The human brain contains about 10^{10} nerve cells or neurons that are interconnected by numerous nerve fibers that form an extremely complicated network. Each neuron consists of a cell body (soma), many small extensions of the soma (dendrites), and a long nerve fiber (axon). The axon makes contacts with neighboring nerve cells via specialized junctions called synapses.

Like any other biological cell, the soma is surrounded by a membrane, which is selectively permeable for ions. When the cell is at rest, the concentration of potassium (K^+) and sodium (Na^+) ions is different inside the cell from that of the outside. This unequal distribution of charge results in an approximate -70 mV potential difference between the inside and outside of the cell. This is referred to as the *resting potential*. If the resting potential is reduced beyond a certain threshold, the voltage-gated ion channels will open, allowing the membrane to become permeable to Na^+. The influx of Na^+ ions will result in a sudden change in membrane potential, otherwise known as the *action potential* (or spike). The action potential is conducted down the

presynaptic cell's axon to the axon's terminals, where the action potential initiates communication with the postsynaptic cell at the synaptic junction (fig 2.1). This communication is achieved by the release of neurotransmitters to the ligand-gated channels of the postsynaptic neuron. This once again changes the permeability for certain ions, resulting in a change in the postsynaptic membrane potential (PSP). Whether this potential will add to or subtract from the existing postsynaptic membrane potential depends on the nature of the synapse. In the excitatory synapse, an input action potential propagating down an axon branch of the presynaptic cell will induce a small depolarization across the membrane of the postsynaptic cell. In the inhibitory synapse, the action potential induces a postsynaptic membrane hyperpolarization. If, as a result of the cumulative addition of synaptic activity, the cell becomes sufficiently depolarized, it will generate it's own action potential. The elicited action potential will travel along the postsynaptic axon until it reaches a nearby synapse, where neural transmission is once again attempted.

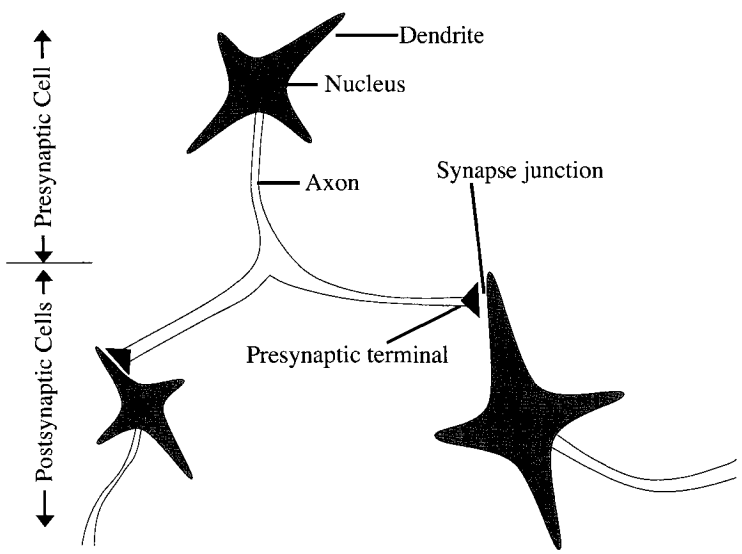

Figure 2.1: As an action potential from the presynaptic cell reaches a synapse junction in the postsynaptic cells, it provokes the release of neurotransmitters which cause ion channels in the postsynaptic membrane to open. The degree with which the postsynaptic potential is altered depends on the nature of the synapse (see text for details).

Postsynaptic depolarizations and hyperpolarizations, while of smaller magnitude, are much longer lasting (10-200 ms) than the propagating action potentials (1-2 ms) [1]. The longer lasting postsynaptic currents produce net effects if a large number of dendrites are arranged in a parallel fashion such as, e.g., the pyramidal cells of the cortex. In fact, approximately 75-85% of the neurons in the cortex are pyramidal cells, characterized by a broad base at the bottom, and an apex that points upwards to the cortical surface. The neurotransmitter of pyramidal neurons is glutamate, which is excitatory. Non-pyramidal neurons in the cortex are referred to collectively as interneurons. Most of these interneurons (smooth stellate, basket cells, chandelier cells and double bouquet cells) use the inhibitory neurotransmitter gamma-amino butyric acid (GABA).

Since it is not very likely for action potentials to occur synchronously in large numbers as PSPs, it has been suggested that action potentials contribute little to the extracranial magnetic fields or surface potentials recorded at the scalp [2, 3]. Instead, studies correlating surface potentials and intracellular potentials in cortical neurons have shown a direct relationship of PSPs and EEG [4]. Other studies have confirmed this, and it is generally believed that the potentials measured at the scalp via the EEG are mainly attributed to extracellular currents from summed PSPs [5, 6, 7, 2, 8].

The source of the PSP can be modelled as a current dipole [9, 10]. Dipole generators do not only impress a current at the source location, but also cause currents to flow through the surrounding tissue, so-called volume currents. Consequently, the currents can be separated into two components, the *primary* current term $j^p(r)$, representing the impressed neural activity from microscopic cellular events, and a *secondary* volume-current term $j^v(r)$ representing the macroscopic events. Assuming an infinite and homogeneous volume conductor, the total current density $J(r)$ is given by

$$J(r) = j^p(r) + j^v(r) = j^p(r) + \sigma E(r) = j^p(r) - \sigma \Delta \Phi \tag{2.1}$$

where $E(r)$ is the electric field, σ is the conductivity and Φ is the electric potential. The PSP from one activated neuron does not render a measurable electric potential or magnetic field at the surface of the scalp. However, the postsynaptic volume currents of a large number (~ 1 *million*) of active synapses will generate a measurable potential at the scalp [11]. This region of synaptic activation usually covers a small

area ($\sim 1\ mm$) and is excited almost synchronously [8].

2.2.1 Solving the bioelectric inverse problem

Dipole models, which are frequently used in attempts to solve the bioelectric inverse problem (see [12] for a detailed review of factors affecting the accuracy of the inverse solution), require explicit a priori assumptions about the cerebral current sources. That is, a single dipole model is only applicable when one assumes that only a small portion of the cortex is activated so that a single, point-like source can describe it. In cases where the number of active cortical areas are small (such as in a motor task or in the analysis of epileptic spikes), the single dipole approach has been shown to be an accurate representation of cortical activity [13, 14]. If this assumption is uncertain, there is no guarantee of the reliability of the solution. For example, it has been shown that a single dipole analysis of binaural auditory evoked potential (AEP) data can converge on a solution which is found in the middle of the brain, which is physiologically incorrect [15]. It has therefore been suggested that incorrectly identifying the number of active sources is perhaps the most serious of all dangers with the single dipole model [16].

In view of the intrinsic problem that it is often difficult to determine the exact number of dipole sources a priori, methods that do not need this a priori assumption have received increased attention. These methods are generally referred to as distributed source models, and they do not require a-priori knowledge regarding the number of active sources. Several approaches can be used such as *Minimum norm (MN)* [17], *Laplacian weighted minimum norm (LORETA)* [15] and *Local autoregressive average (LAURA)* [18]. Distributed models are advantageous for the localization of poorly known activity distributions [16].

2.3 Visual Evoked Potentials

Generally, EEG signals are analyzed by identifying their different frequency components, or rhythms. The alpha rhythm for example is one of the most prominent normal brain rhythms in humans. It is defined by its frequency range of 8 to 13 Hz. Gamma activity on the other hand is defined as a much faster rhythm (40 Hz). While the analysis of brain rhythms make it possible for clinicians to observe the rate of

brain activity in different conditions (i.e. eyes opened vs. eyes closed), it is difficult to monitor the brain's response to a particular stimulus from these recordings. This is because the neuroelectric signal changes associated with the presentation of stimuli are not readily apparent in the ongoing scalp EEG. Instead, it is more favourable to extract signal changes in the EEG that are time-locked to the presentation of a stimulus, or, event related potentials (ERPs). Examples of such stimuli, or 'events' may be a series of sensory stimuli (such as a visual flash or an auditory sound) or mental events (such as recognition of a specified target stimulus). The brain's response to these stimuli are extracted from the EEG by recording temporal windows, or 'epochs' of EEG activity that is time-locked to the presentation of each stimuli. All epochs from the same stimuli are averaged together, creating a single epoch reflecting the brain's response to that particular stimulus. The spontaneous background EEG fluctuations, which are random relative to when the stimuli occurred, are therefore averaged out, resulting in a signal with a relatively high signal-to-noise ratio (SNR). The ERP thus reflects, with high temporal resolution, the patterns of neuronal activity evoked by a stimulus.

Visual evoked potentials (VEPs) are ERPs in response to visual stimuli. Two general classes of visual stimuli are typically used: flashes and patterns. Pattern stimulation is generally obtained using a checkerboard pattern of black and white squares that periodically contrast-reverse without a change in the overall luminance. Several factors affect the pattern-reversal VEP such as gender [19], rate of reversal [20], check size [21], luminance [22] and check contrast [23]. A pattern-reversal rate of 1 to 2 Hz is useful for recording the transient VEP, while reversal rates greater than 10Hz are useful for eliciting steady-state signals that are most appropriately analyzed in the frequency domain. The transient VEP evoked by pattern stimulus typically has three components: a negative going deflection at 75ms (N75), a positive going deflection at 100ms (P100) and a negative going component at around 150ms (N150).

It is generally believed that the N75 generator is located in the primary visual cortex, or V1 (the neuroanatomy of the visual cortex is described in more detail in chapter 3) [24, 25, 26]. The location of the P100 generator remains debatable. Several VEP reports have indicated that the P100 generator is located in area V1 [25, 26], but other VEP studies have argued that it may also originate in area V2/V3 [27],

V3/V4 [28] and V5 [29]. Invasive studies using subdural electrodes by Noachtar et al. [30] reported that the P100 is most probably generated by a dipole source localized in close proximity of the calcarine fissure. The study by Bonmasser et al. [31] localized the N75 and P100 within close proximity of one another using an inverse solution whose solution space spanned a $10mm^3$ grid (each grid point served as a test site for a possible dipole solution). It is possible the spatial resolution of this dipole solution is unable to account for the relatively small distance that may exist between the N75 and P100 sources. Bonmasser et al. [31] also reported a low VEP SNR, which can affect the accuracy of the inverse solution. Lastly, this study used a 32 electrode montage, which may not be sufficient in sampling the potential distribution, and thus lead to dipole localization errors [32, 33]. Invasive recordings in humans have shown that the N75 and P100 have distinct physiological structures [34]: the N75 is driven by EPSP and the P100 is driven by IPSP [35]. An excellent review of VEPs can be found in [36].

2.4 Functional Magnetic Resonance Imaging (FMRI)

Although a thorough explanation of the events that shape the FMRI signal is beyond the scope of this thesis, the fundamental basics of the FMRI signal can be sufficiently described without an in-depth analysis of biological systems/events. Generally, the basic principles of the FMRI signal can be explained by directly examining the fundamental properties of the nuclear magnetic resonance phenomena (NMR).

2.4.1 Semi-classical Description of Nuclear Magnetic Resonance

To maintain consistency, the term NMR will be used instead of MRI throughout this section since this chapter will focus on the physical phenomena of NMR. The theory of NMR begins with a quantum analysis of the magnetic dipole moments of the nuclei within atoms. The Hydrogen atom (^{1}H) for example, contains a positively charged nucleus (made up of one proton, p^+) with a single orbiting electron, e^-. Aside from their orbital motion, electrons posses their own intrinsic angular momentum (or *spin*) S, which is characterized by the spin quantum number I. The magnitude of the spin

angular momentum is given by

$$|S| = \sqrt{I(I+1)}\ \hbar \tag{2.2}$$

where $\hbar$ is Planks constant divided by 2π. Protons in the nucleus also have this property. In fact it is the net spin of the nuclei that is of interest in NMR studies. As far as medical applications are concerned, the ^{1}H proton is the nucleus of most interest because of both its high natural abundance and large concentration in human tissue (table 2.1).

Table 2.1: Nuclear Spin Quantum number of biologic nuclei (natural abundance values are given in percentages of an element occurring on earth in its specified isotopic form)

Nucleus	Spin Quantum number I	Natural Abundance (%)
(^{1}H)	1/2	99.9
(^{13}C)	1/2	1.1
(^{23}Na)	3/2	100.0
(^{35}Cl)	3/2	75.4

A particles spin S results in a tiny magnetic moment μ_s, and is given by

$$\mu_s = \gamma S \tag{2.3}$$

where γ is the gyromagnetic ratio. This proportionality constant is a property of the particular nucleus and has a value of 42.58 MHz/T for protons. The energy associated with the magnetic moment μ_s in a magnetic field B_0 is

$$E = -\mu_s \cdot B_0 \tag{2.4}$$

In the classical description, the magnetic moment can assume any orientation with respect to the direction of the applied magnetic field. Quantum mechanics on the other hand dictates that the projection of μ_s is limited to a finite set of values m. A general expression for the permitted values of S is

$$S = m\hbar \tag{2.5}$$

where

$$m = I, I-1, I-2, ..., -I+1, -I \tag{2.6}$$

In general, a nucleus with spin quantum number I can have $2I+1$ energy levels (one for each value of m). In the case of the proton, which has been found experimentally to have $I = \frac{1}{2}$, there will only be two allowed states identified by $m = \pm\frac{1}{2}$. The energies associated with these two states are given by

$$E = -m\gamma\hbar B_0 \tag{2.7}$$

Thus, the energy of the ^{1}H nuclei will consist of two levels ($E_{m=-\frac{1}{2}}$, $E_{m=+\frac{1}{2}}$). If we assume the field is applied in the $+z$ direction (B_{0_z}), then these distinct energy levels may be thought of as representing the two possible orientations the magnetic moment μ_s can take on in the static magnetic field B_{0_z}. This is referred to as Zeeman splitting, and is shown in figure 2.2. In NMR, we are primarily concerned with the net magnetic

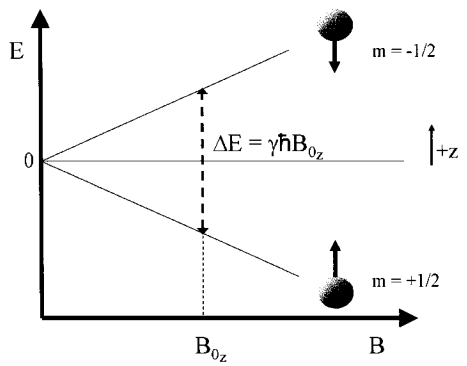

Figure 2.2: In the lower energy state ($m = +\frac{1}{2}$), the magnetic moment is aligned parallel to the applied field. In the higher state ($m = -\frac{1}{2}$), the magnetic moment is aligned anti-parallel to the applied field. Quantum mechanics dictates the ^{1}H nucleus is limited to the parallel or anti-parallel state in the presence of a magnetic field.

moment of a large number of nuclei. In normal conditions, the net magnetization is effectively zero since all nuclei are directed in a random fashion. In the presence of a magnetic field, the nuclei will orient themselves either parallel or anti-parallel to the applied field. The ratio of the population of the two states ($m = \pm\frac{1}{2}$) can be calculated from Boltzmann statistics. Consider a sample with N number of nuclei in a static field. The ratio of nuclei N in each state is

$$\frac{N(m=+\frac{1}{2})}{N(m=-\frac{1}{2})} = \exp\frac{-\Delta E}{KT} \tag{2.8}$$

where $\Delta E = \gamma\hbar B_0$ is the energy difference between the two allowed states, K is Boltzmans constant and T is temperature in degrees Kelvin. At room temperature, it can be shown that at in a 1.5 T field, there are only approximately 10 extra protons per million in the lower parallel energy state than there are in the higher antiparrallel energy state. At first glance, this may seem quite small for NMR detection, however, given Avogadro's number (6.023×10^{23}), it can be shown that in one gram of water, there are approximately 6.688×10^{17} excess spins in the parallel state. It is this excess that serves as the net magnetization and is what is measured in NMR. Since the net magnetization increases as the population difference between the energy levels increases, the NMR signal will strengthen with increasing field strength [37].

Aside from the two distinct orientations the ^{1}H nucleus spin can take on in an applied magnetic field, its magnetic moment will also experience a torque

$$\tau = \mu_s \times B \tag{2.9}$$

A classical treatment shows that the time rate of change of angular momentum $\frac{dS}{dT}$ is equal to the torque. Hence, from eq.2.9 and eq.2.3, it is found that the magnetic moment in a magnetic field will experience a time rate of change of angular momentum given by

$$\frac{d\mu_s}{dt} = \gamma(\mu_s \times B) \tag{2.10}$$

The resulting motion is a precession of μ_s about the magnetic field B (figure 2.3). The angular frequency of this precession can be found by examining the difference in energy between lower and higher states.

$$\Delta E = \gamma\hbar B_0 = h\nu \text{ where } \nu = \frac{\gamma}{2\pi} B_0 \tag{2.11}$$

Expressing this frequency ν in angular terms give what is known as the *Larmor frequency*, which is the single most fundamental expression in NMR (eqn. 2.12).

$$\omega_0 = \gamma B_0 \tag{2.12}$$

In a 1.5T field for example, a proton will precess at a rate of 63.9 MHz.

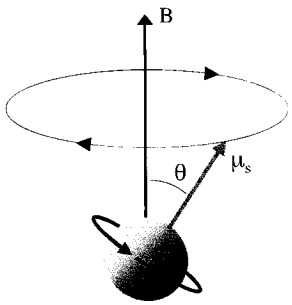

Figure 2.3: Clockwise precession of a proton's spin about an applied magnetic field B

2.5 Measuring the FMRI signal

2.5.1 Image contrast

In humans, the MR-sensitive hydrogen atom, as a constituent of the water molecule H_2O, can virtually be found in every form of tissue (table 2.2). This varying range of

Table 2.2: Water content of tissue in the human body

Tissue	Water content(%)	Fat content (%)
Brain-gray matter	84-86	5.3
Brain-white matter	68-77	18
CSF	99	-
Fat	-	99

water concentration within the brain allows NMR to use the ^{1}H proton as a contrast agent for different tissues. Another form of image contrast lies in the exploitation of the *relaxation* time differences between tissue types.

2.5.2 T1 weighted contrast

Following the application of a static field B_0, a second field B_1 can be applied to displace the magnetic moment of the nuclei. If B_1 is set to the same frequency with

which the nuclei are precessing (eq. 2.12), an efficient transfer of energy will occur and the net nuclear magnetic moment will flip into the direction of B_1. In a 1.5T field, the frequency required by the excitation pulse B_1 is usually in the MHz range, and therefore usually referred to as a radio frequency (RF) pulse. The flip angle is directly proportional to the applied field B_1

$$\Delta\theta = \gamma B_1 t \tag{2.13}$$

where $\Delta\theta$ is the change in the net magnetic moment angle over t seconds. For example, the strength of B_1 required for a 90° flip angle over 1 ms is 5.9 μT. For similar imaging experiments using electrons instead of protons, a B_1 field in the microwave spectrum is required, which would deposit too much energy, and thus can not used for human studies. Upon termination of the RF pulse (but with the static field B_0 still active), the nuclei will begin to relax back to their original equilibrium position M_0 (figure 2.4).

The manner in which this restoration of equilibrium manifests itself is called T1 relaxation

$$M_z = M_0(1 - e^{-(\frac{t}{T1})}) \tag{2.14}$$

where M_z is the magnitude of the magnetization vector at time t. Upon investigation of eqn. 2.14, one can see that it takes approximately $t = 5T1$ for the magnetization vector to restore 99% of its original position. The spin's return to equilibrium is characterized by the T1 relaxation parameter. That is, upon termination of the RF pulse, the spins will dissipate their newly acquired energy throughout their local environment, or lattice. T1 relaxation is therefore often referred to as *spin-lattice* relaxation. There are some factors that can alter this relaxation process. As molecules tumble and move around throughout the lattice (due to thermal vibrations), their local magnetic environment is always changing. If these fluctuating fields are in close proximity of the spin of interest, a transfer of energy between the molecule and nuclei of interest can occur. The probability of such energetic transfers happening depends on the *correlation time*. The correlation time τ_c, is the time it takes a molecule to rotate by 1 rad. If $\frac{1}{\tau_c}$, the frequency of the rotation, is close to the Larmor frequency ω_0 of the nucleus of interest, then the probability of a energetic transition is increased [38]. Hence, a favorable energetic pathway is created, leading to a faster return to the

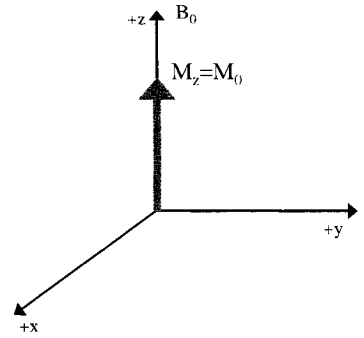

(a)

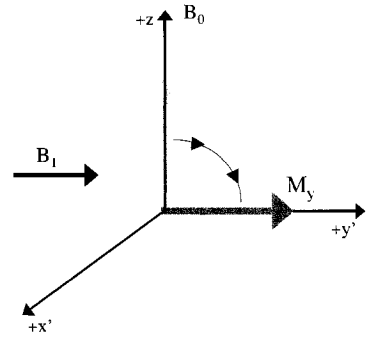

(b)

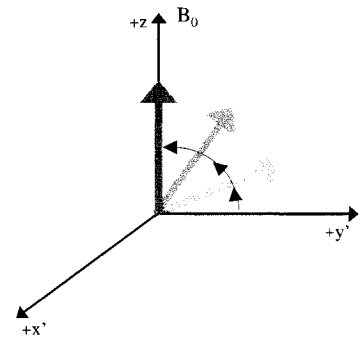

(c)

Figure 2.4: (a) In a static field, the magnetization vector is $M_z = M_0$. (b) At $t = 0$, an RF pulse is applied. The magnetization vector is tipped in the direction of B_1 ($M_z = 0$). (c) After some time following the RF pulse ($t \sim 5T1$), the magnetization vector returns to its original equilibrium position.

equilibrium state. The correlation time of a molecule depends on its size - mid-sized molecules such as fat move slowly, while small molecules such as water vibrate quickly. For example, the correlation time of a water molecule is $\tau_c \sim 10^{-12}s$ [38]. Therefore, since $\frac{1}{\tau_c} >> \omega_0$, there is a poor efficiency at stimulating transitions, resulting in a long T1. The motional frequency of fat molecules are very close to that of the Larmor frequency for the ^{1}H nuclei, which results in an efficient transfer of energy and a faster restoration of equilibrium (i.e. short T1, (table 2.3)). This variation of T1 across the

Table 2.3: T1 tissue constants at 1.5T

Tissue	T1(ms)
Fat	259
Brain-white matter	786
Brain-gray matter	921
CSF	3000

brain assists in creating excellent contrast between tissue such as fat and cerebral spinal fluid (CSF, fig. 2.5).

Figure 2.5: In T1 weighed images, regions of significant fat content (white matter) appear bright, while regions of low fat content (CSF) appear dark.

2.5.3 T2 weighted contrast

The preceding section dealt with interactions between the system of nuclear spins and its lattice. In addition, each individual precessing spin interacts with neighboring spins through their respective magnetic fields. The total magnetic field at any single nucleus consists not only of the applied field B_0, but also the resultant local fields produced by neighboring magnetic dipoles. This is referred to as *spin-spin* interaction. The additional field 'felt' by a local spin will vary depending on its position in the lattice. At a distance of 1 angstrom, the field is approximately 1 gauss. According to the Larmor relation (eq. 2.12), this will lead to a spread of values of the precession frequency at different nuclei throughout the sample. Following an RF pulse, the magnetization vector among different nuclei in a sample will become out of phase with one another (figure 2.6). The rate of the M_{xy} decay is referred to as T2 relaxation. It can be expressed as:

$$M_{xy} = M_0(e^{-(\frac{t}{T2})}) \tag{2.15}$$

where M_{xy} is the net magnetization in the transverse plane. In most cases, spin-spin relaxation occurs faster than spin-lattice relaxation ($T2 < T1$, table 2.4).

Table 2.4: T2 tissue constants at 1.5 T

Tissue	T2(ms)
Fat	85
Brain-white matter	90
Brain-gray matter	100
CSF	1400

2.5.4 T2* weighted contrast

Perhaps of more significance to FMRI is $T2^*$ relaxation. Consider a group of nuclei in a sample where a static field $B = B_0$ is applied. Assuming an ideal system, all nuclei will rotate at the same Larmor frequency $\omega = \omega_0$. In addition to the applied field, a linear field gradient G_x is applied along the x axis, such that

$$B(x) = B_0 + G_x \tag{2.16}$$

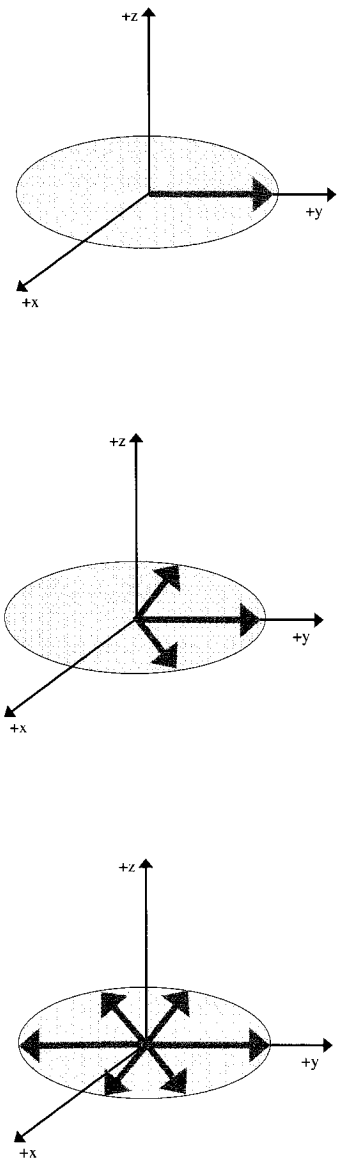

Figure 2.6: (Top) At time $t = 0$ after a RF pulse, all spins are in phase. (Middle) Soon after, random field fluctuations cause some spins to lag behind or ahead of the resonant frequency ω_0. (Bottom) Eventually, the majority of phase coherence among nuclei is lost, resulting in a zero net magnetization in the transverse plane.

The nuclei will thus precess at a different rates depending on their position within the sample (fig. 2.7). In general, this spread of Larmor frequencies across the sample

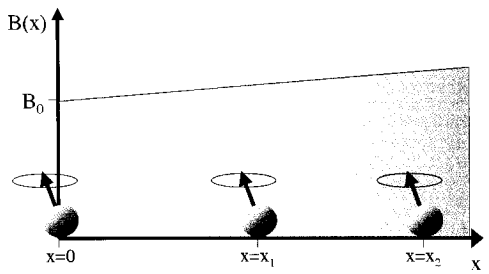

Figure 2.7: Larmor frequency as a function of linear field gradient G_x. Field strength is minimal at $x = 0$ (clear region), and maximal at $x = x_2$ (shaded region). The Larmor frequency is thus ω_{x_1}, ω_{x_2} and ω_{x_3} at points x_1, x_2 and x_3, respectively.

will be

$$w(x) = \gamma B(x) = \gamma(B_0 + G_x) \tag{2.17}$$

This field variation will also result in the nuclei losing phase coherence with one another, and lead to an additional decay rate termed $T2^*$. $T2^*$ relaxation is considered to be a secondary form of $T2$ relaxation. As discussed previously, the $T2$ relaxation time depends primarily on spin-spin interactions, which are random and therefore non-reversible: we have no control over them. $T2^*$ depends on both spin-spin interactions and the homogeneity of the external magnetic field, which can in part be controlled externally. For example, $T2^*$ processes can be refocused using a 180° RF pulse, while $T2$ processes cannot. $T2^*$ can be written as

$$1/T2^* = 1/T2 + \gamma\pi\Delta B_0 \tag{2.18}$$

where ΔB_0 is the magnetic field variation across the sample (or voxel). Thus, if the field variations across the voxel approaches zero, the value of $T2^*$ approaches $T2$. We can express the $R2^*$ ($R2^* = \frac{1}{T2^*}$) process as the sum of these effects:

$$R2^* = R2 + R2' \tag{2.19}$$

where $R2$ reflects the $T2$ decay rate and $R2'$ is the secondary dephasing term due to field inhomogeneity effects. There are several sources of $R2'$ that can affect the $R2^*$ decay rate. First, the magnet may not be completely uniform due to imperfections in the windings of the superconducting coils. This effect is usually minimal due to routine maintenance and shimming. For FMRI studies, a more pertinent source of the $R2^*$ decay rate is due to the magnetic properties of blood.

2.5.5 Spatial encoding of the MR signal

Just as the images we view in MR are two-dimensional arrays or matrices of intensities, the coil voltages collected from the scanner are stored in two-dimensional arrays, or *k-space* (k_x and k_y in 2D):

$$k_x(t) = 2\pi\gamma G_x t \tag{2.20}$$

$$k_y(t) = 2\pi\gamma G_y t \tag{2.21}$$

The application of a G_x gradient for a time t moves the k-space coordinate along the k_x direction by an amount $2\pi\gamma G_x t$. If no gradients are applied, then the k-space coordinate remains stationary. An example of how k-space is filled in a routinely used high-resolution anatomical scan (such as a Spoiled Grass (SPGR) sequence) is shown in figure 2.8. Only when all the lines of k-space have been sampled can an image be reconstructed. So, for an $N \times N$ image, NG_y steps must be performed, resulting in a total image time of NTR seconds. For high-resolution images, N is usually 256 and TR is typically between 10-50ms, resulting in an imaging time of 2.6-13.0 seconds per slice. As it will be shown in the next section, functional imaging generally requires that an entire brain volume is acquired within 2-5 seconds. This can be achieved by using fast echo-planar imaging (EPI) pulse sequences (figure 2.9). In EPI, each line of k-space is acquired by using short 'blips' of the G_y gradient to bump the k-space coordinate up a line, followed by a positive or negative G_x gradient to drive the trajectory forewords or backwards along k_x until all the points in k-space have been collected. In EPI, the entire brain volume is acquired following a single RF excitation pulse (B_1). Since the MR signal is decaying with T2 (and T2*), there generally are only a certain number of k-space lines that can be acquired before the signal vanishes. This means that only a limited image resolution is possible. Typically, a 64×64 pixel

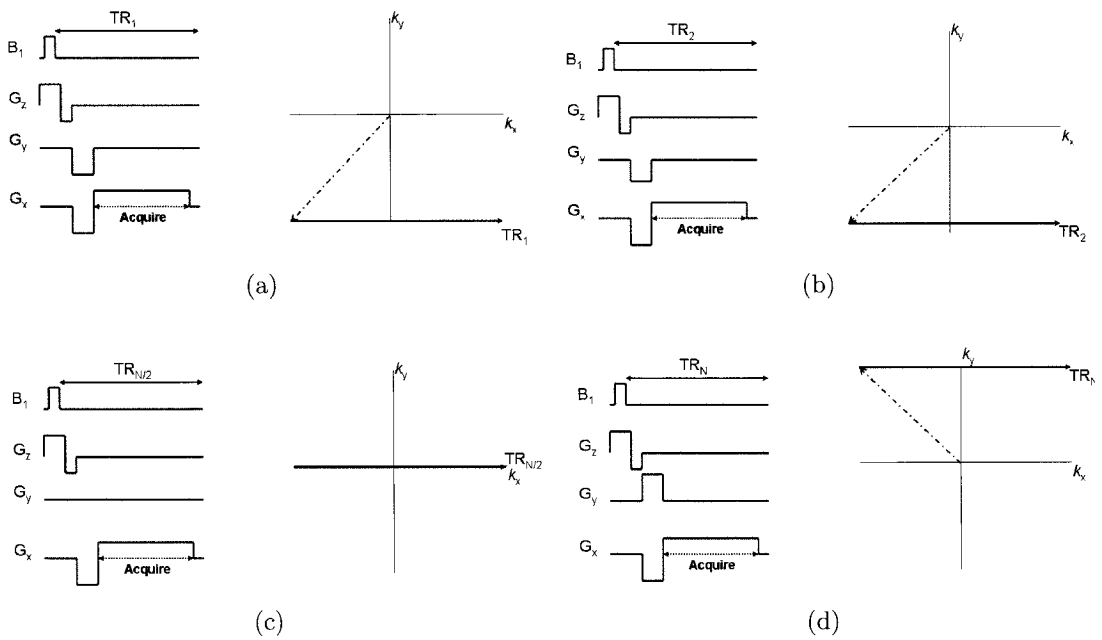

Figure 2.8: Pulse sequences (left) and their accompanying k-space navigation (right) for a general SPGR pulse sequence. Positive G_x and G_y gradients moves the k-space coordinate in the positive k_x and k_y direction, respectively. (a) Initially, the k-space coordinate moves from the origin to $-k_x$ and $-k_y$ (dashed arrow). After this, G_y is set to zero and $+G_x$ is applied, resulting in the encoding from $-k_x$ to $+k_x$ after a time TR_1. In (b), the G_y gradient is reduced, thus filling a different line of k-space after a time TR_2. In (c), the G_y is zero throughout (TR) and is positive in (d).

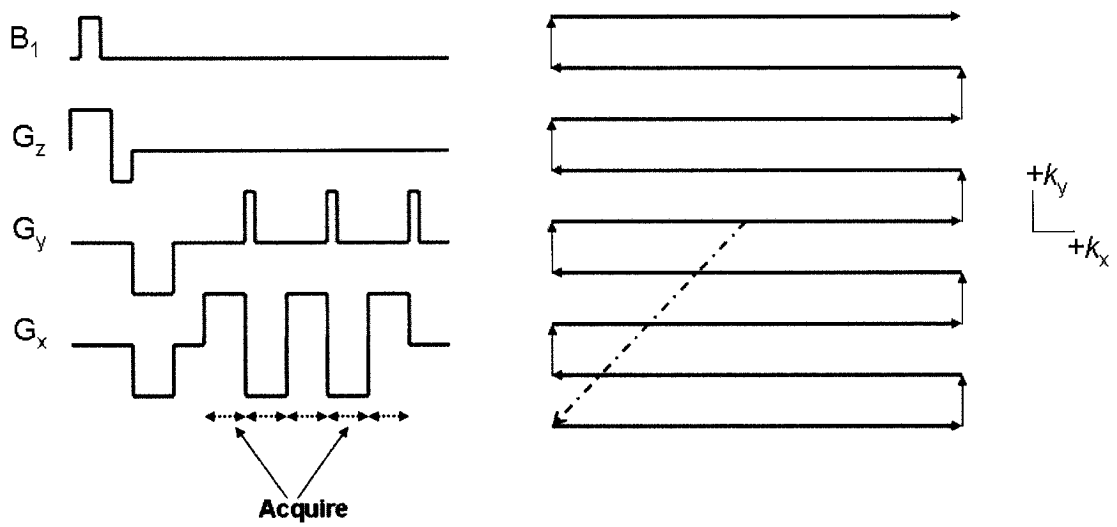

Figure 2.9: Pulse sequences (left) and the accompanying k-space navigation (right) of an echo-planar imaging sequence (EPI). EPI sequences only require one excitation pulse (B_1) and use short G_y gradients to bump the k-space coordinate after each acquisition along $\pm k_x$.

image using EPI can be acquired in about 80ms, or 2 seconds for a 24-slice full brain volume.

The coordinates of k-space are referred to as spatial frequencies. Spatial frequency describes the rate at which image features change as a function of position. The MR image signals from a large, fairly uniform object essentially do not change over a long range of spatial positions. Such objects are said to produce an abundance of low-spatial-frequency signals. However, when the edge of the object is encountered, image signal changes rapidly as a function of position. Edges are represented by high spatial frequencies. Low amplitude and/or short-duration gradient events encode low-spatial-frequency information; these data are mapped to the center of k-space. Conversely, high-amplitude and/or long-duration gradient events encode high-spatial-frequency information; this information is mapped to the periphery of k-space. In fact, most image information, including contrast and general shape, is contained in the low-spatial-frequency data mapped to the center of k-space. Spiral imaging sequences take advantage of this by heavily sampling the center of k-space relative to the periphery. Spiral trajectories typically either start or end at the origin of k-space and trace out a spiral path as shown in figure 2.10. This early sampling of the center of k-space minimizes several significant artifacts such as those due to flow and motion [39].

2.6 BOLD contrast

The fundamental factor giving rise to the FMRI signal has to do with the intrinsic properties of the two main constituents of human blood; Hemoglobin (Hb) and De-oxyhemoglobin (dHb.) Hemoglobin, the predominant macromolecule in blood, is the main carrier of oxygen throughout the body. It consists of two pairs of polypeptide chains, each of which is attached to a heme group, which is a complex form of iron and protoporphyrin. It has been shown by magnetic measurements that the deoxyhemoglobin molecule consists of four unpaired electrons per heme. Molecules with unpaired electrons have relatively large magnetic moments, and are referred to as being *paramagnetic*. Experimental studies have found the magnetic moment of deoxyhemoglobin to be approximately 5.46 Bohr magnetons per heme [40, 41]. Oxyhemoglobin on the other hand, does not contain any unpaired electrons (*diamagnetic*)

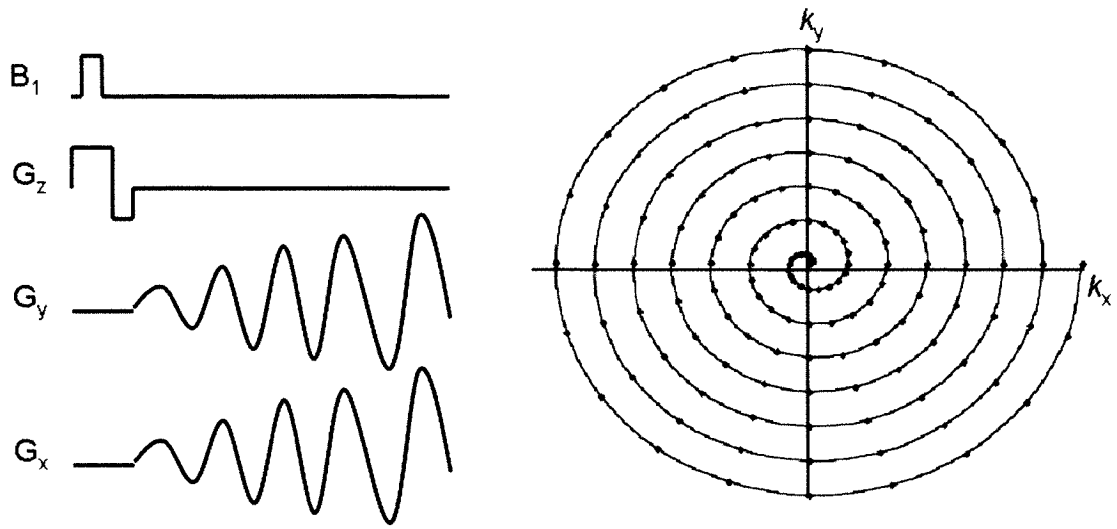

Figure 2.10: Pulse sequence (left) and the accompanying k-space navigation (right) of a spiral imaging sequence. In spiral sequences, the gradients are changed in a sinusoidal fashion, thus putting less strain on the MR hardware compared to the quickly changing gradients in the rectilinear sequence shown in figure 2.9. Spiral trajectories heavily sample the center of k-space where the low-spatial frequency data, encoding general shape and contrast, is mapped.

and has no significant net magnetic moment. An NMR sample rich in oxyhemoglobin in the presence of an external field will experience a field at the nucleus different than a sample rich in deoxyhemoglobin. This is characterized by the sample's magnetization M in response to a magnetic field H

$$M = \chi_m H \tag{2.22}$$

where

$$H = \frac{B}{\mu} \tag{2.23}$$

and μ is the permeability of the material. The magnetic susceptibility χ_m is a dimensionless quantity that varies from one substance to another - positive for paramagnets and negative for diamagnets. That is, the applied magnetic field is opposed in diamagnets, but is reinforced in paramagnetic materials. M in part, determines the effective magnetic field at a nucleus. Therefore, even in a perfectly uniform static magnetic field, nuclei in regions with different magnetic susceptibilities will react differently. The human head for example consists of regions with greatly varying magnetic susceptibility. This variation is particularly steep at the boundaries such as the air/tissue interfaces. These boundaries can lead to rapid dephasing of the nuclear spins, resulting in a rapid T2* relaxation. These magnetic susceptibility differences are not only found at air/tissue interfaces, but also in blood. FMRI is a modality that is sensitive to the changes in the ratio of oxyhemoglobin to deoxyhemoglobin within a sample. The paramagnetic deoxyhemoglobin molecule can distort a local magnetic field on a microscopic scale causing neighboring spins within this region to experience different Larmor frequencies. The variation in precessional frequencies among the excited nuclei results in a loss of phase coherence which results in shortening of the T2* relaxation parameter. Generally, a short relaxation parameter results in quick signal decay, resulting in a smaller detected NMR signal. The differences in relaxation times can be used to identify regions with high and low oxy-deoxyhemoglobin concentrations. The imaging of these differences is often referred to as blood-oxygenation level-dependent (**BOLD**) imaging [42, 43, 44].

2.6.1 Metabolic demands of neural activity

The amounts of oxy-deoxy hemoglobin throughout the brain are dependant on its energetic demands. The activation of neurons through establishment of PSPs and action potentials all require energy. Since the bulk of this activity occurs in the cortical layers, the gray matter consumes approximately 4 times more energy than the white matter. Energy is supplied in the form of adenosine tri-phosphate (ATP) generated in the mitochondria within cells. Under normal conditions, the formation of ATP requires glucose and oxygen for metabolism. The results of a large number of experiments have in fact revealed a clear relationship between local brain activation and glucose consumption [45, 46] and oxygen uptake [47]. Shulman et al. showed a linear relationship between brain metabolism and glutamate cycling [48]. The relationship between the change in blood flow and the change in ATP generation on the other hand appears to be highly variable, with some studies reporting a 1:1 ratio [49] and others reporting a 20:1 ratio [50]. Interestingly, the increased blood flow to activated brain regions supply an amount of oxygen that exceeds the amount necessary for local consumption [51, 52]. This increased supply of fresh blood leads to an increase in the $\frac{[Hb]}{[dHb]}$ concentration. This change in concentration results in a change in the local magnetic properties of the surrounding tissue, thus locally altering the image intensity on the MR image (figure 2.11). It has been since shown that the **BOLD** contrast depends not only on blood oxygenation but also on cerebral blood flow and volume [53, 54, 55]. The **BOLD** signal can be elicited with the onset of various external stimuli (visual, somatosensory etc.). The onset of a stimulus-induced hemodynamic response is typically delayed by approximately 2 seconds [44], reaches a plateau after 6-12 seconds and returns to baseline after a prolonged post-stimulus undershoot [56, 57, 58]. The main drawback of BOLD-based neuroimaging is its temporal resolution (the temporal resolution of EEG is on the order of ms).

2.6.2 Neural basis of +BOLD and -BOLD

Generally speaking, the areas of the brain showing significant **BOLD** effects can be found by comparing the signal in a voxel to a model of the stimulus profile. In its most simplistic form, this model takes the shape of a square wave consisting of 'on' and 'off' periods. Areas of the brain that correlate with this model can be referred to

as **+BOLD**; the measured signal goes above baseline during the stimulus period, and returns to baseline during the rest period. However, it has also been shown that some areas of the brain will do the opposite; the signal will peak below baseline during stimulation. This can be referred to as **-BOLD**. Studies have indicated that the **+BOLD** response is largely due to excitatory synaptic activity [59, 60, 61]. Initial studies argued that the **-BOLD** response was be due to 'vascular stealing'. This theory suggests the elevation of blood flow at the activated location causes reductions in blood supply in nearby areas sharing the same blood vasculature, suggesting that negative hemodynamic changes have no neural correlate [62, 63]. More recent studies have provided evidence against this hypothesis [64], suggesting it is mostly due to neuronal inhibition [65, 66].

2.6.3 Effects of venous blood flow on BOLD contrast

Approximately 75% of the cerebral blood volume is contained in venous vessels and only 5% in the capillary bed [67, 3]. Aside from blood oxygention, flow and volume within intracortical veins, the MR signal from within the larger vessels is also affected by the paramagnetic properties of deoxygenated hemoglobin. Hence venous drainage can be a dominant component of the BOLD signal, particularly at low field strength [68]. Consequently, the true site showing increased neuronal activity is likely to be contaminated by the downstream effects of these draining veins. For example, using high resolution FMRI, Lai et al. [69] found that activation induced by finger movements precisely matched the vein in the central sulcus, rather than the gray matter tissue of the precentral gyrus. Similiar vascular artifacts have also been shown at field strengths up to 4 Tesla [70, 71].

One method of suppressing vasculature effects is by using a cross-correlational analysis to determine differences in the delay of the signal between activated venous and gray matter tissue. The delay of the response may reflect the transit time through the vasculature, with voxels overlying draining veins having longer delays. Lee et al. [67] reported that the signal in voxels anatomically associated with gray matter was delayed between 4 and 8 s compared with the stimulus, whereas the signal in voxels correlated with visible vessels was generally delayed from 8 to 14 s. This larger delay is consistent with the longer time required for blood to reach the larger vessels. Since

the correlation-coefficient is sensitive to temporal differences between two datasets, the vasculature effects may be suppressed by limiting the analysis to voxels with a relatively high correlation coefficient. Another method of suppressing this effect is to make use of pulse sequences that are relatively insensitive to blood flow all together, such as spiral sequences.

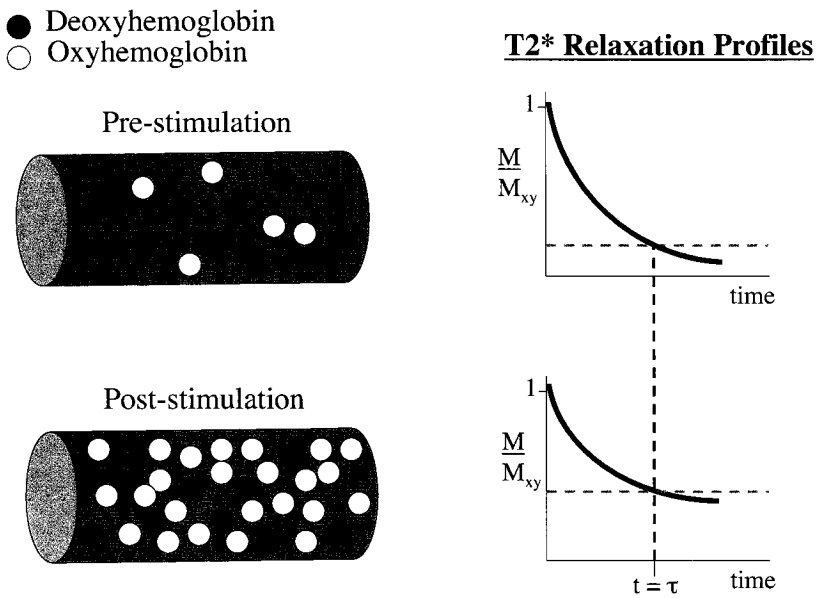

Figure 2.11: *Top:* In the unstimulated condition, there is little activation of neurons; blood flow is not increased and a relatively large portion of the hemoglobin is in deoxy form. Since deoxyhemoglobin is a paramagnetic substance, it creates a local field inhomogeneity which results in rapid dephasing among nuclei. The $T2^*$ curve is thus steep and at $t = \tau$, the ratio of the net and transverse magnetization vector ($\frac{[M]}{[M_{xy}]}$) is relatively small. *Bottom:* In the stimulated condition, neurons become active; blood flow increases and the proportion of deoxyhemoglobin within the sample decreases. As a result, the dephasing of the nuclei is slower; the $T2^*$ curve is less steep and $\frac{[M]}{[M_{xy}]}$is large at $t = \tau$ (adapted from [72]).

2.7 Neurovascular coupling

The interpretation of **BOLD**-based functional imaging of the brain is critically dependent on understanding the relationship between observed hemodynamic responses and the underlying neural changes. MR imaging is able to identify the magnetic susceptibility differences between the paramagnetic deoxyhemoglobin and diamagnetic oxyhemoglobin. That is, FMRI does not directly reflect neural activity as the EEG does. In fact, the exact nature of the neural-hemodynamic relationship remains largely unknown. A recent study by Kim et al. [73] showed that at the scale of several mm (3-5mm^2), the **BOLD** signal correlates linearly with the underlying neuronal activity. However, at the level of smaller recording sites (sub-millimeter), the correlation between the two signals varied substantially. The study suggested that FMRI activation resulting from large voxels (as routinely used in human studies) may indeed accurately reflect the underlying neuronal activity. However, this study did not explicitly address what constituents of total neural activation (such as action potentials or synaptic activity) correlated better with the **BOLD** signal. To address this aspect of the neuro-vascular relationship, single unit recordings can be made if a microelectrode is placed close to the soma or axon of a neuron. The measured extracellular field potential (EFP) will directly report the spiking of action potentials of that neuron [74]. If the microelectrode is placed further away from the spike-generating sources so that local action potentials do not dominate the measured signal, then the measurement is referred to as the mean EFP (mEFP). The mEFP is therefore related to both synaptic events *and* to spikes generated by neurons. The two different signal types can be segregated by frequency band separation. A high-pass filter cutoff of 300Hz is used in most recordings to obtain spiking activity, and a low-pass filter cutoff of 300Hz is used to obtain the so-called local field potentials (LFPs). Studies have shown that such a band separation does indeed measure different neural events [75].

The LFPs, the low-frequency range of the mEFP signal, represent mostly slow events reflecting synchronous activity in neural populations. Until recently, these signals were thought to represent exclusively excitatory and inhibitory synaptic events. Evidence for this came from combined (EEG) and intracortical recordings showing that the slow wave activity in the EEG is largely independent of neuronal spiking

[76, 77, 78]. Later studies however provided evidence of the existence of other types of slow activity unrelated to synaptic events, including voltage-dependent membrane oscillations and spike afterpotentials [79].

Studies using invasive recording techniques in animals have suggested that areas of increased blood flow found in FMRI represent neuronal populations with increased synaptic input as opposed to increased axonal output [80]. This has also been reported at the single-unit level [81, 82] as well as regionally in the visual and somatosensory cortices [83, 84]. More specifically, a recent study based on theoretical interpretation of the **BOLD** signal has suggested that the activation seen in functional imaging studies probably results from excitatory synaptic activity rather than inhibitory synaptic activity [59]. Using Transcranial Magnetic Stimulation (TMS), Waldvogel et al. [60] reported a similar finding, stating that inhibitory synapses, being less numerous and strategically better located than excitatory synapses, may be more efficient, and therefore less energy-consuming, than excitation. Taken together, the majority of these results suggest that the **BOLD** signal is correlated to neural activation, and that it is the changes in the LFPs that are more closely related to the evolution of the **BOLD** signal than changes in the spiking activity of neurons. As discussed before, the EEG signal is also due to synaptic events, and not spiking. In theory, it may therefore be reasonable to assume that changes in the measured EEG may also be observed in the measured FMRI.

2.8 Combined FMRI/EEG studies

The majority of the studies described in the previous section are based on invasive recordings of cortical activity. While the results shed some light on the microscopic relationship between neuron and vasculature, the relationship between macroscopic measures of cortical neural and hemodynamic activity (as measured by EEG and FMRI, respectively) remains unknown.

One method of estimating the spatial locations of EEG and FMRI sources is to merge the two datasets together. Ideally, this approach would take advantage of the varying temporal and spatial resolutions of the two modalities. The most common approach to combine hemodynamic and electromagnetic data is to constrain EEG

dipole solutions to the area of activity obtained by FMRI [85, 86]. This is advantageous from an inverse solution vantage point as it imposes limits on possible dipole solution sites and may also aid in better estimating the number of dipolar sources. This approach has been used in several VEP/FMRI studies [87, 24, 29]. However, this method strongly relies on the assumption that dipolar sources of EEG activity are indeed located within regions exhibiting a **+BOLD** response. Such a finding was reported by DiRusso et al. [24], who, through VEP and FMRI measurements, found a better correspondence between the location of the *N75* dipole and the **+BOLD** compared to the correspondence of the *P100* and the **+BOLD** location [24]. A recent study by Vitacco et al ([88]) attempted this sort of data fusion by comparing unconstrained EEG inverse solutions (using the LORETA algorithm [89]) with the **+BOLD** response. They found a significant correspondence between FMRI activity and the LORETA maps in only half of the subjects, suggesting that a correspondence between EEG and FMRI cannot always be assumed. It should be noted that all of these studies did not take into account the **-BOLD** response, which may be be initially driven by the same sources of that of the EEG.

Chapter 3

Physiology of the Human Visual Cortex

3.1 Introduction

The steps leading to the formation of images in humans is a complex path beginning at the eye and ending in the brain. The human eye and its relationship to cortical activity has been studied extensively in the past and therefore has a well established physiological basis. The research in this thesis is largely dependent on cortical responses to visual stimulation, and therefore a brief review of the anatomy and physiology of human vision is presented.

3.2 Visual pathway

The human eye is a slightly asymmetrical sphere with a volume of about 6.5 cc. The very back of the eye is lined with a membrane containing photoreceptor nerve cells, or, the retina. Figure 3.1 shows a cross-section of the human eye, as well as the anatomical terms used in this section. The retina contains millions of light sensitive cells, called rods and cones. The center of the retina is called the macula. The area within the macula, the fovea, is the region of highest visual acuity and cone cell density. Despite its small size relative to the rest of the retina, the fovea is very important for our ability to see fine detail and color.

When light hits rods or cones, a biochemical reaction occurs, which initiates the transmission of signals to the ganglion cells, which then in turn signal to the brain. There are about 1.2-1.5 million retinal ganglion cells in the human retina. A remarkable difference between foveal and peripheral retina can be seen in its increased packing-density of ganglion cells in the cone-dominant foveal retina as compared the rod-dominant peripheral retina. The ganglion cells are the final output of the retina. The portion of retinal ganglion cells axons that are outside the eye form the optic nerve.

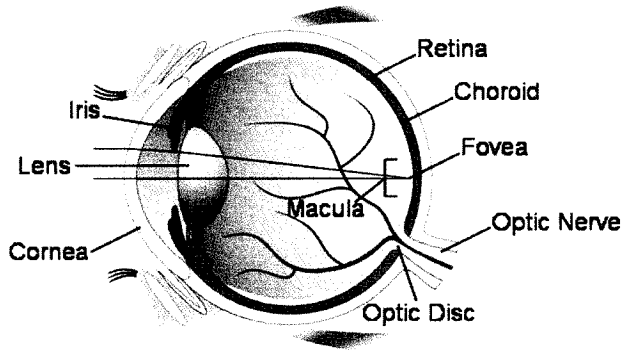

Figure 3.1: A cross-sectional view of the eye shows three different layers: The external layer, formed by the cornea. The intermediate layer, divided into two parts: anterior (iris) and posterior (choroid). The internal layer, or the sensory part of the eye, is called the retina

The region of the retina from which the ganglion cell axons exit, the optic disc, contains no photoreceptor cells and therefore is insensitive to light. The pathway from optic disc to brain is achieved via the optic nerve. The nerve fibers from both eyes stay intact until they reach the optic chiasm; a partial crossing of the ganglion cell axons from both eyes.

Here, the left and right visual worlds are separated. After the chiasm, the fibers are referred to as the optic tract. While each optic nerve carries all the visual information from one eye, the optic tract carries a complete representation of one half of the visual field. Therefore, if one of these tracts is damaged, vision will be lost in one side of each eye. The optic tract wraps around the midbrain to get to the lateral geniculate nucleus (LGN), where all the ganglion cell axons must synapse. From there, the neurons in the LGN send their axons directly to the primary visual cortex. These are called optic radiations (figure 3.2).

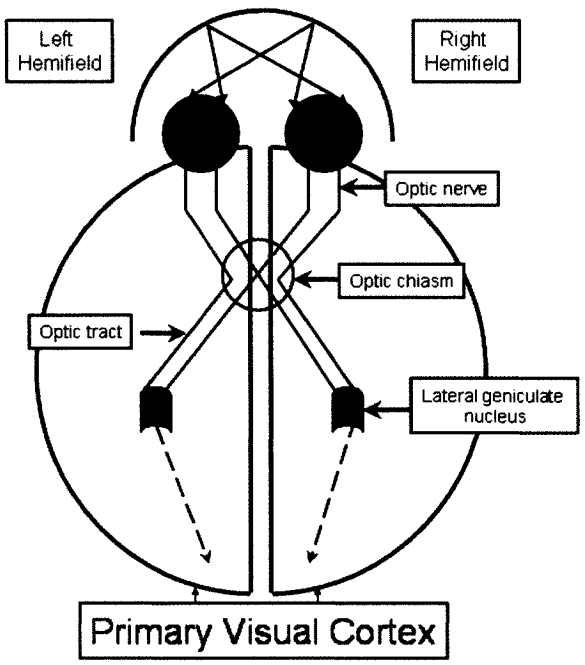

Figure 3.2: The left and right visual field is processed in opposite cortical areas based on the pathway of the nerve fibres leaving the retina. All of the visual information is initially carried via the optic nerve. The visual fields are independently segregated at the optic chiasm, and it is this information that is directly sent to the primary visual cortex via optic radiations (dashed arrows).

3.3 Visual cortex

All visual information that the eye receives is processed by a part of the brain known as the visual cortex. The visual cortex is located at the very back of the occipital lobe. The visual cortex consists of six layers of cells (layers 1-6) between the cortical surface (layer 1) and the underlying white matter (layer 6). These six cortical layers introduced by Brodmann [90] have been subdivided time and time again as new information regarding the neural networks of the visual cortex have been revealed.

Layer 1 is nearly aneuronal, composed mainly of dendritic and axonal connections of pyramidal cells from the lower layers. Even though it contains almost no neuron cell bodies, it is a networking layer that has a direct affect on the firing properties of pyramidal cells in deeper layers [91]. Layers 2 & 3 contain many small and medium sized, densely-packed pyramidal neurons, respectively. They receive output from other cortical layers and can either connect with deeper cortical layers or send their outputs to other cortical areas. The principle layer for inputs from the LGN is layer 4, which is so thick and specialized that it is further subdivided into into three sub-layers: 4A, B and 4C. The input into layer 4 propagate the excitement up to layers 2 and 3, and from there either down to layers 5 and 6 or to other cortical areas. Layers 5 & 6 contain the largest pyramidal neurons, which send outputs to the brain stem, thalamus and spinal cord.

These division of cortical layers are not specific to the visual cortex. All cortical areas in the brain are composed of six basic layers, but different areas of cortex may contain modifications of layers to best serve its function. It was on the basis of layer appearance and cell types alone that Brodmann first subdivided the cortex into over 50 functionally distinct areas. The visual cortex is broken down into five functionally distinct areas, labeled V1, V2, V3, V4, and MT. The latter is on occasion is referred to as V5. The primary visual cortex (or V1, area 17) is often referred to as the *striate* cortex. The other areas of the visual cortex are referred to as being *extrastriate* (figure 3.3).

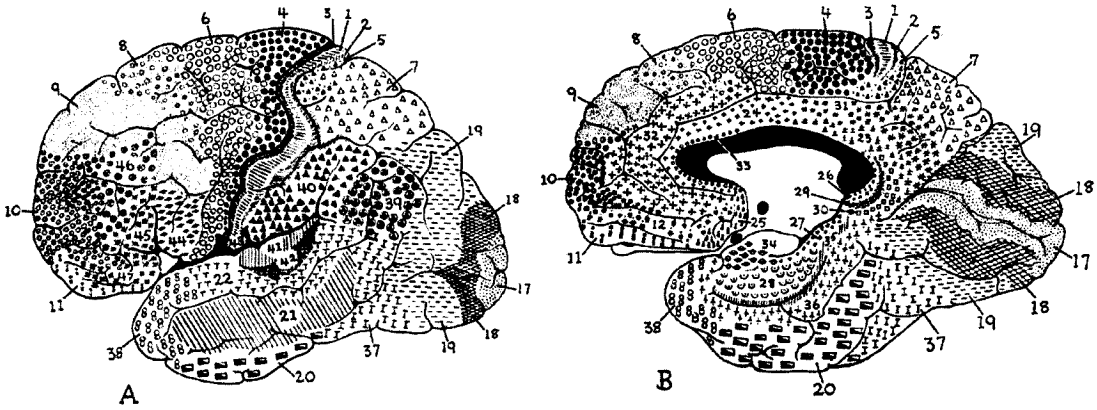

Figure 3.3: The division of neurological functioning based on anatomical regions of the brain. (a) Lateral and (b) medial views are shown. Area 17 is the primary visual cortex (V1). Area 18 is V2, 19 is V3. The motor cortex is in area 1-5. Taken from [90].

3.3.1 Striate cortex

V1 (striate cortex, area 17) is one of the most extensively studied and understood areas of the human brain. V1 lies in the fold of the calcarine fissure (figure 3.4). Although a small part of V1 is located on the lateral surface, most of it occurs on the medial surface of the occipital lobe. There is a point-to-point representation of the retina onto V1. This is called the retinotopic organization of the primary visual cortex. The fovea is represented at the posterior end of the calcarine fissure. The fovea has an expanded representation, which occupies about half of the primary visual cortex. This is due to the high density of ganglion cells in the retinas fovea relative to its periphery, and is referred to as cortical scaling. The most anterior portion of V1, on the medial surface of the occipital lobe, represents the peripheral portion of the visual field. Objects above the line of sight are represented on the lower half of the calcarine sulcus. The lower visual field is represented on the upper half of the calcarine fissure (figure 3.5 & 3.6). Cell density is also very high in V1: 250,000 neurons per square millimeter, versus 100,000 in the rest of the cortex. In primates, area V1 plays a critical role in visual information processing, since most visual information ultimately reaching the rest of visual cortex is first funneled through V1 [92].

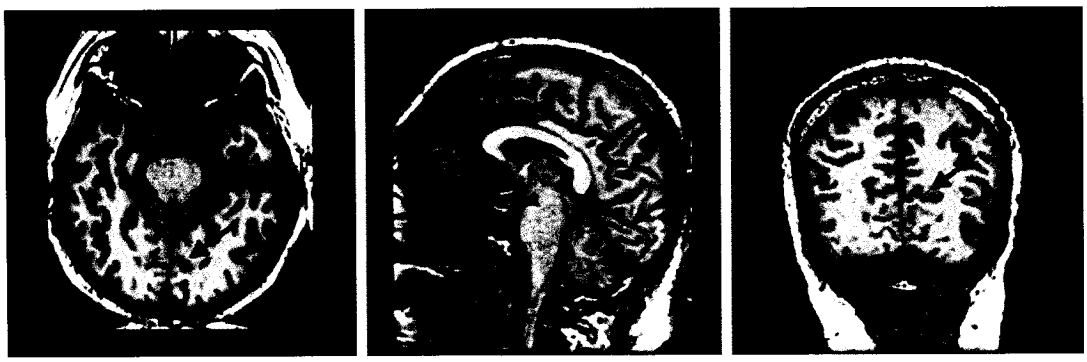

Figure 3.4: The black arrow points to a portion of the calcarine fissure in an axial (left), sagittal (middle) and coronal MRI slice (right).

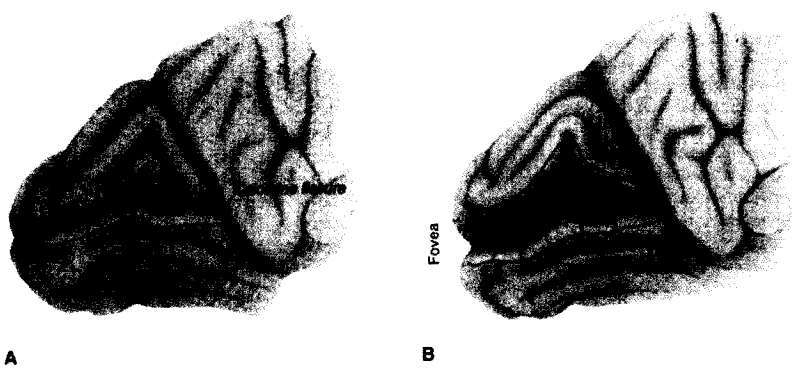

Figure 3.5: Retinotopic mapping of V1. (a) Objects viewed in the upper or lower portions of the visual field are mapped on the lower and upper banks of the calcarine fissure, respectively. (b) Objects viewed in the central and peripheral portions of the visual field are mapped onto the more posterior and anterior regions of the calcarine fissure, respectively. The visual angle is displayed below the calcarine fissure to show how visual eccentricity maps onto to the calcarine fissure. Taken from [93] with permission of the author.

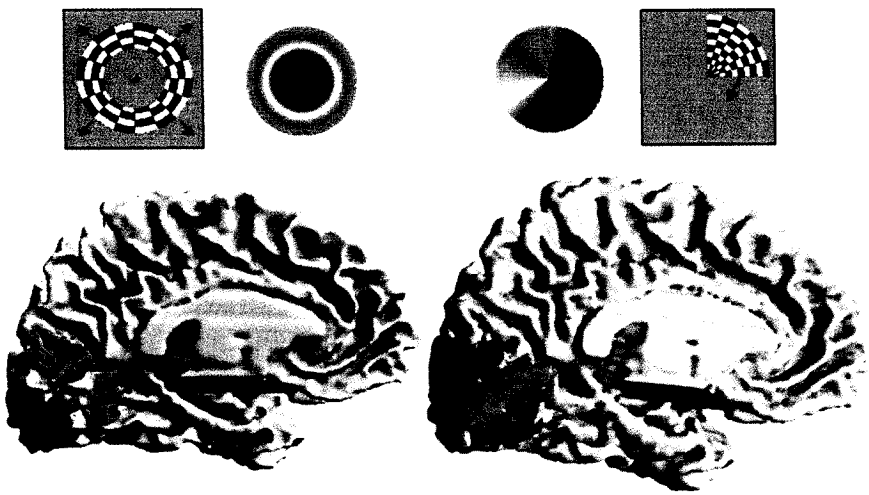

Figure 3.6: Retinotopic mapping of visual cortex through FMRI measurements. The image on the left shows how stimulus in the fovea (blue) is activated near the occipital pole and extends anteriorly along the calcarine fissure with increasing stimulus eccentricity (green). The image on the right shows the upper and lower banks of the calcarine fissure being activated given the position of the stimulus wedge. Taken from [94] with permission of the author.

3.3.2 Extrastriate cortex

Adjacent to V1 are the visual association cortical areas V2, V3, V4 and V5 (MT). These areas are modulated by different effects such as motion [95], attention [96] and working memory [97]. Injury to the extrastriate area does not necessarily disturb the visual field, that is visual sensation remains intact, though it can impair higher forms of visual perception, such as hue perception and visual attention [98].

Chapter 4

Spatial Relationship of ERP and FMRI Sources-I

4.1 Abstract

The integration of EEG and FMRI can provide considerable insight in brain functionality. However, the direct relationship between neural and hemodynamic activity is still poorly understood. Of particular interest is the sensitivity of FMRI to different event related potential (ERP) components. In the current study, we localize sources generated by a checkerboard stimulus presented to eight subjects using both EEG and FMRI. The location of the sources of the visual evoked potential (VEP) are estimated at each VEP time point and compared to the location of peak FMRI activity. In the majority of participants, we found a direct correspondence between the N75 source location and positive **BOLD** activation (**+BOLD**), and a direct correspondence between the P100 and negative **BOLD** activation (**-BOLD**). These findings suggest that both the positive and negative FMRI response need to be considered when comparing FMRI to the different VEP components.

4.2 Introduction

Two commonly used modalities for the non-invasive study of human brain function are the electroencephalogram (EEG) and Functional Magnetic Resonance Imaging (FMRI). The EEG is sensitive to neural activity in the brain, and can measure changes in electric potential at the surface of the scalp with a time resolution of milliseconds. In order to estimate the source location of event related potentials (ERP), one must solve the so-called inverse problem. However, only by introducing assumptions about the sources and volume conductor can accurate solutions to the inverse problem be attained. An example of such constraint is to limit the spatial extent of the solutions to a particular region of the volume conductor, the brain. The simplest way to model the human head is by using a spherical model. Although commonly used, the spherical

model can lead to source localization errors as its geometry is a poor representation of actual head geometry [99, 100, 101, 102, 103]. For a more accurate approximation, a realistically shaped head model can be constructed via MRI [104, 105]. Lastly, to obtain realistic results, the solution space is often constrained to broad regions where neurophysiologic activity is expected or areas where FMRI activation is detected [87].

The most commonly used method to image brain function using magnetic resonance imaging (MRI) is by using the Blood-Oxygenation-Level-Dependence (BOLD) contrast [42]. Here, signals are acquired based on the magnetic susceptibility differences in the brain caused by the change in oxy and deoxy hemoglobin. Such changes generally occur with a time resolution of seconds.

Several studies have probed the neuro-vascular relationship using similar experimental tasks across subjects undergoing sequential or simultaneous EEG/FMRI measurements. Correspondence of EEG-FMRI sources has been reported in auditory [106, 107, 108], visual [24, 109, 87], somatosensory [110] and visual language tasks [88]. Despite the large number of these studies, many questions remain about the nature of the sources responsible for specific ERP components and FMRI activation. It is possible that the straight forward localization of a particular ERP component may correspond well to an active FMRI site, while others may not. A recent study investigating language processing by Vitacco et al. [88], studying the **+BOLD** response only, reported a direct correspondence of ERP-FMRI sources in only half of the subjects, concluding that ERP and FMRI source correspondence cannot be assumed in all cases.

In this study, we employ a pattern reversal stimulus that elicits robust ERP signals with a high signal to noise ratio (SNR). This is doubly advantageous since the inverse problem has been shown to be sensitive to signal quality[111, 112]. It has been suggested that the first three major visual evoked potential (VEP) components (N75, P100 & N150) are not only localized in different areas of the visual cortex [113, 24, 29], but are also physiologically distinct [113, 114, 25, 115]. We report the correspondence between the location of specific VEP components with positive and negative FMRI responses in order to further evaluate the relationship between neurological and vascular sources.

4.3 Methods

4.3.1 Subjects and stimulus

Eight healthy subjects with no history of neurological impairment were recruited for both EEG and FMRI recording sessions (mean age 20.3, range 20-28 years, 5 males). All subjects where right handed and had normal vision. Subjects were instructed to fixate on a red fixation point located in the center of a black screen. The experimental task was a block design, consisting of 3 'on' and 4 'off' periods (figure 4.1). During the 'on' block, a checker board was presented in either right or left hemifield and reversed at a rate of 2Hz. The visual stimulus was developed using the *STIM* software (Neuroscan©) for EEG recordings and *Presentation* (Behavioral Systems©) for FMRI recordings. For FMRI, the stimulus was projected onto a screen and viewed via a mirror placed approximately 2-3 cm from the subjects eyes (*Avotec* ©). This reversal rate was chosen in order to allow for sufficient time for VEP components to fully return to baseline. The checkerboard subtended approximately 6° x 6° of the visual field. This stimulus size and spatial frequency has been shown to result in robust VEP components [116] that elicit VEP and FMRI activation within area V1 [31]. The 'off' block consisted of a black screen with fixation point. The block design was presented twice and averaged for each participant. FMRI and EEG data were acquired in separate sessions using the same experimental task. The sessions were balanced such that four subjects completed the FMRI first, while the remaining completed the EEG first. Sessions were no more than one week apart. Ethics approval was granted by the local regional ethics board.

4.3.2 ERP Measurements

The EEG was acquired using a 64 channel Ag/AgCl electrode cap (Neuroscan©). Electrode placement followed the International 10-20 System [117], and were all referenced to a frontal central electrode (FCz). An electrode placed at AFz was used as a common ground. Inter-electrode impedances were kept below 10kΩ. Horizontal and vertical eye movements were recorded using an elector-oculogram (EOG) with electrodes placed over the outer canthus of the right and left eye as well as above and below the right eye. Subjects were comfortably seated in a soundproof, dimly lit

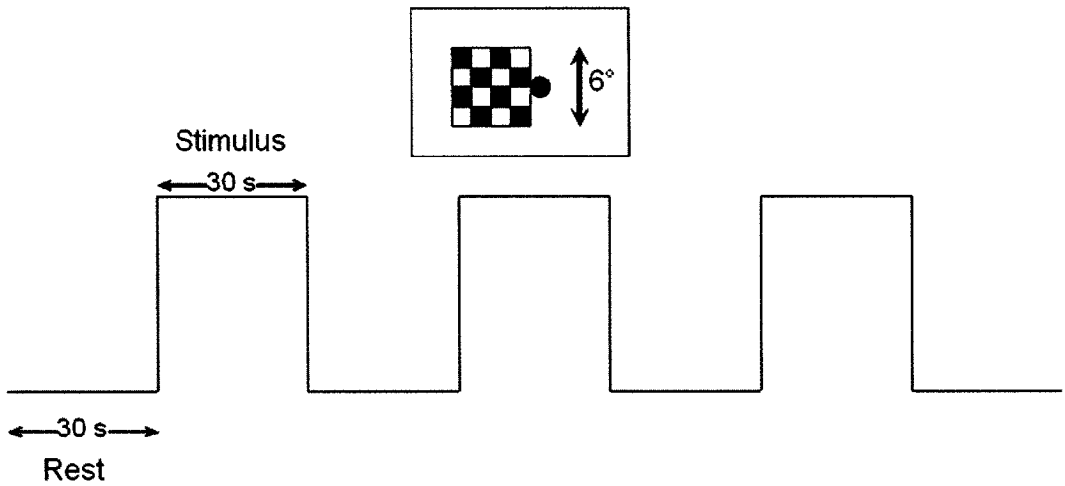

Figure 4.1: Experimental setup used for both EEG and FMRI recording sessions. Stimulus consisted of a 2Hz pattern-reversal checkerboard in either right or left visual field. Subjects were instructed to maintain fixation on a small point in the center of the screen.

room. EEG recordings were digitally recorded at 500Hz with a bandpass of 0.1-100 Hz together with a 60Hz notch filter and stored for off-line analysis. The recording session was repeated for all subjects. Post-processing was performed using the SCAN analysis software (Neuroscan©). EEG epochs (-10-300ms temporal range) were created based on the onset of triggers recorded during the recording session. The data was bandpass filtered within 1-35Hz. An EOG artifact correction algorithm was used to remove all trials with amplitudes that exceed 75mV. The trials were de-trended using a 2nd order polynomial correction and then averaged for right and left stimulus conditions. This resulted in two VEP datasets (left hemifield and right hemifield) per participant. Each dataset consisted of at least 250 sweeps out of a maximum of 360, which has been shown to be an appropriate number of sweeps for VEP analysis [118]. Subsequently, each dataset had a relatively large SNR (>20 in all subjects).

4.3.3 VEP source analysis

Source analysis of VEP data was carried out using the CURRY V4.5 software (Neuroscan©). Individually shaped realistic head models were created for each subject

using a semi-automated boundary element algorithm [104]. These head models were tessellated with approximately 3000 triangles per compartment with a triangle edge length of 8, 7 and 6 mm and conductivities of 0.33, 0.0042 and 0.33 S/m for the scalp, skull and brain regions, respectively. Electrode positions were determined by locating fiducial landmarks placed on the subject prior to FMRI scanning. A coordinate system using the vectors joining the right and left pre-auricular points (PAL, PAR) and Nasion (NAS) landmarks was created. In order to localize the generators of the pattern-reversal stimulus, a single current dipole was used as a source model. This has been shown to be an appropriate source model for similar VEP studies [119, 120]. A single current dipole was fitted at every time instant between 0-200ms. The dipole position was initially seeded at the origin of the brain model (where the PAL/PAR and NAS vectors meet). The best-fit dipole position and residual variance (RV) was calculated, as was its distance from the center of the FMRI cluster for each time instant. To determine how robust the inverse solution was, the inverse procedure was repeated by constraining dipole solutions to the visual cortex. This was done by segmenting the visual cortex with voxels that matched those used during FMRI recordings (figure 4.2). This resulted in approximately 2000 elements per segmented volume. A dipole was placed at the center of each voxel, and the best-fit magnitude and orientation together with the residual variance was recorded. The center of VEP activity was calculated by retaining 1% of the solutions with the least variance and implementing a center of mass algorithm, using the location of each solution weighted by its explained variance. The $x, y, \& z$ component of the N75 and P100 dipole solutions from each subject in the left visual field stimulus condition was compared to the x, y, z components of the dipole solutions obtained in the right visual field stimulus condition. A Student's t-test was used to test for differences.

4.3.4 FMRI measurements & analysis

Anatomical scans

FMRI recording sessions were made on a 1.5T unit (GE Healthcare, Milwaukee WI., Signa) using a quadrature head coil. Prior to FMRI scanning, 120 high resolution axial images were taken using an Inversion Recovery (IR) prepped fast spoiled grass (SPGR) sequence. The field of view was 24cm resulting in slices with a 256 x 256 x

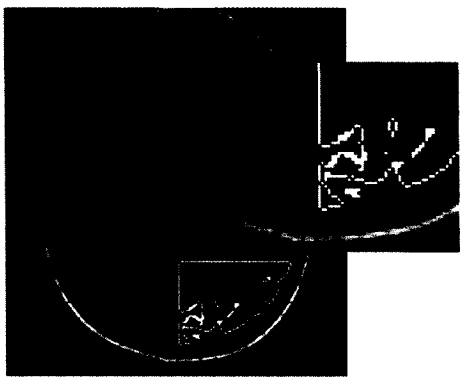

Figure 4.2: Segmentation of visual cortex (magnification shown on right). The segmented volume was divided into a 3D grid of voxels with dimensions matching those used during FMRI recordings. Each voxel served as a testing site for possible VEP solutions.

120 pixel dimension (pixel dimension = 0.937 x 0.937 x 1mm) with a 0.5mm gap in between axial slices.

Functional scans

A fast gradient echo imaging sequence with a spiral readout [121] was employed for functional scans. The field of view was 24 cm, with a 64 x 64 pixel dimension along with a 5 mm gap between axial slices (24 slices in total). Imaging parameters were as follows: TR/TE: 2000/40ms, flip angle: 90, temporal points: 105. Headphones where placed on the subject to suppress noise from the switching gradients. Head padding was also used to suppress head movements. Prior to Fourier transformation, spiral k-space data was re-gridded to Cartesian based coordinates [121] giving a final voxel size of 3.75 x 3.75 x 5 mm thick. Spiral acquisition was used rather than a rectilinear trajectory because it is less sensitive to subtle motion and as it acquires the low spatial frequency information of k-space first, resulting in greater **BOLD** contrast, relative to rectilinear (e.g., EPI) methods [122]. FMRI analysis was carried out using the AFNI software [123]. Motion correction was carried out by registering all functional volumes to the first collected volume. The raw signal in each voxel was Fourier filtered with a bandpass of 0.15-2Hz, de-trended using a 2nd order polynomial and then averaged across both trials. Correlation analysis was carried out using the

processed FMRI signal with a box-car stimulus profile. Correlation values below $\pm$ 0.3 ($p \leq 10^{-4}$) were discarded. These activation maps were smoothed using a Gaussian filter (FWHM = 5mm). The center of the activated cluster was computed with a center of mass algorithm, weighed by the correlation coefficient. This coordinate was ported into EEG source localization software for direct comparison (discussed below) with VEP source modeling estimates. The group average N75 and P100 dipole positions were averaged over all subjects were overlaid onto the group average FMRI dataset. Spherical regions of interest (ROI) with a 7mm radius were placed around these N75 and P100 locations. The FMRI signal over all voxels within these ROIs was extracted and graphically displayed (see Results section). Similar ROIs were used to investigate the correlation coefficient of the FMRI signal and stimulus profile as a function of distance between the N75 and P100 dipole position. ROIs were placed along the line joining the N75 and P100 locations. Correlation coefficient values within each ROI were averaged and graphically displayed.

4.4 Results

4.4.1 VEP analysis

The VEP from one subject during left and right field stimulation is shown in figure 4.3. The average topographic maps over all participants are shown in figure 4.4. The VEP responses elicited the three main components associated with pattern reversal visual stimulation [118]: (latency values averaged over all participants and hemifields are also given): N75 (74.2$\pm$2.4ms), P100 (107.8$\pm$9.8ms) and N150 (166.7$\pm$21.2ms). For all subjects, the amplitude of the N75 component was highest in electrodes ipsilateral to the stimulated field. The amplitude of the P100 component was maximal over the contralateral side of the stimulated field. To detect possible habituation in our data, the first 15 seconds of the VEP data recorded during stimulation was averaged and compared to the lasts 15 seconds. No significant difference in latency or amplitude was detected, indicating that neural habituation was not a factor in our measurements. These habituation results are in agreement with a similar study by Singh et al. [124].

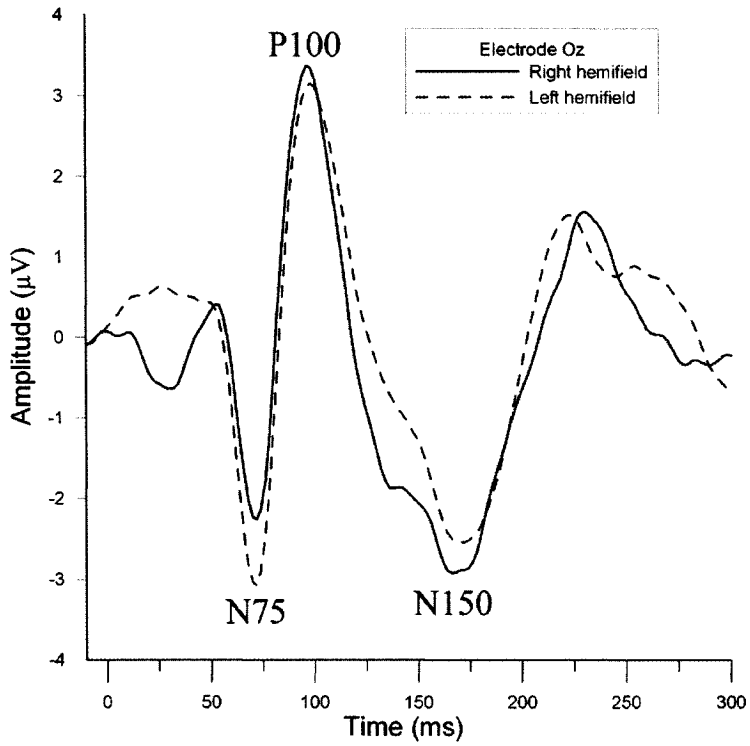

Figure 4.3: VEP waveform measured from electrode site Oz from one participant. The dark line represents the VEP response obtained during right hemifield stimulation. The lighter dashed line is the VEP response obtained during left hemifield stimulation. The three main VEP components are seen at 75ms (N75), 100ms (P100) and 150ms (N150). The peak SNR exceeded a value of 20 in each participant.

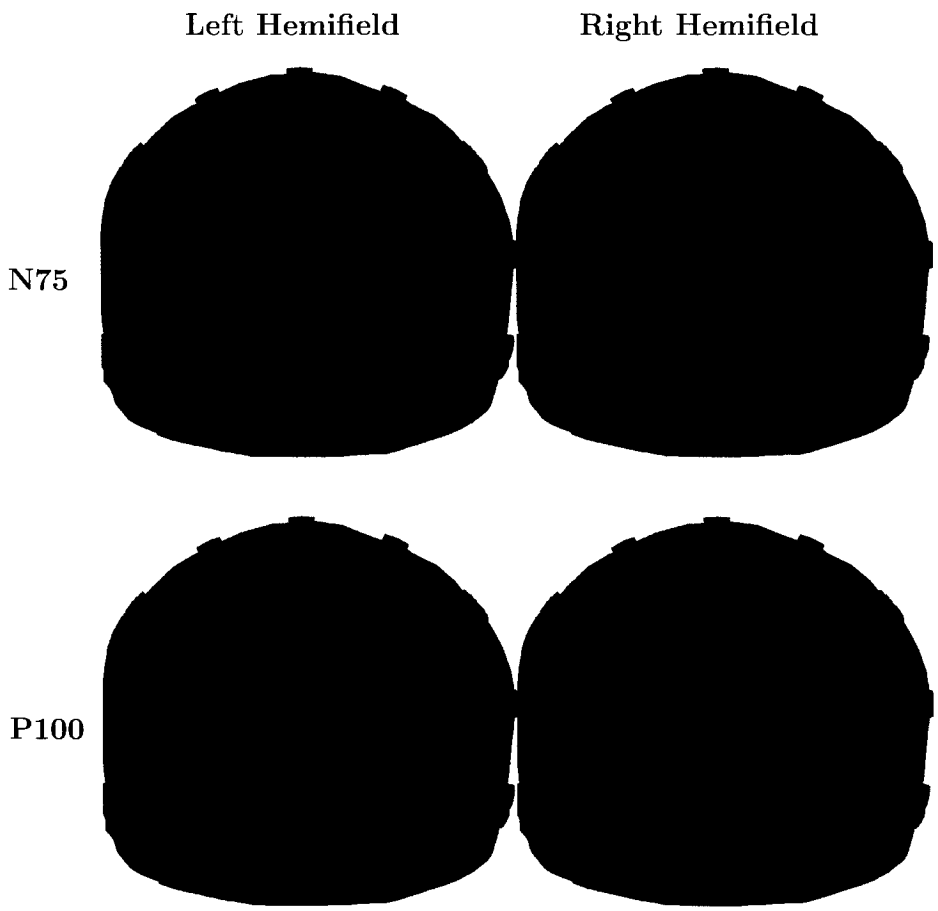

Figure 4.4: Occipital view of group average potential maps of N75 and P100 VEP components. Blue indicates negative potential, red indicates positive potential. Top row: N75 potential map during left and right hemifield stimulation. Bottom row: P100 potential map during left and right hemifield stimulation.

4.4.2 VEP and FMRI source analysis

Results showing the VEP dipole localization and FMRI results from one participant are displayed in figures 4.5-4.9. Dipole localization of left and right hemifield VEP from one participant is shown in figure 4.5 and figure 4.6, respectively. The calculated topographical maps from the N75 and P100 dipole solutions (fitted maps) from the same participant are shown in figure 4.7 and figure 4.8. The difference between the fitted maps and the raw maps is also shown (residual maps). The FMRI response from this participant is shown in figure 4.9.

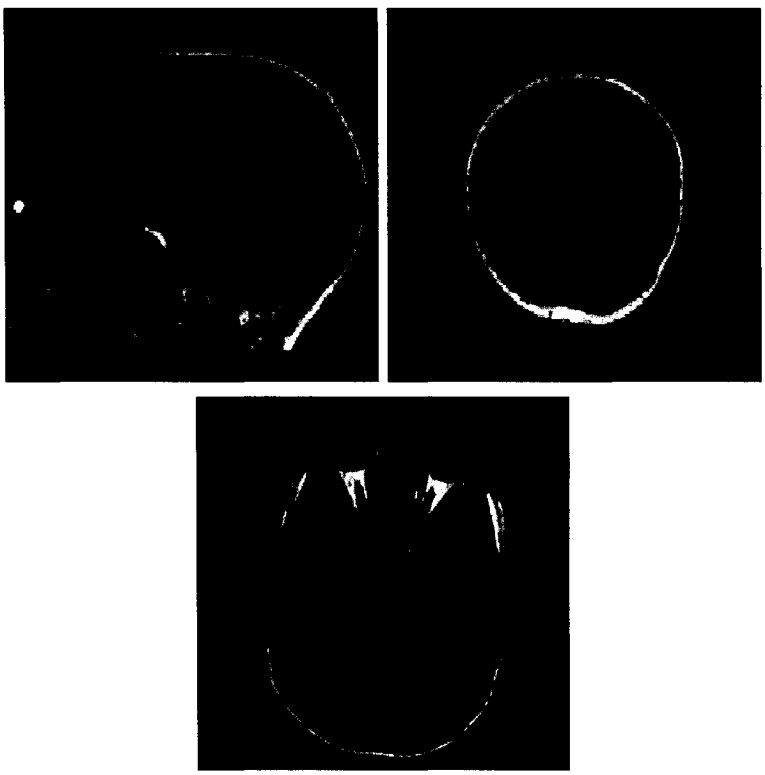

Figure 4.5: Dipole localization of N75 (orange dipole) and P100 (yellow dipole) from one participant during left hemifield stimulation.

The N75 and P100 dipole localization results from all subjects shown in figure 4.10. Group average FMRI maps showing the peak positive and negative response are shown in figure 4.11 and figure 4.12. Dipole locations and FMRI centers of activity (COA) averaged over all subjects are displayed in figure 4.13. Details are listed in Table 4.1. For display purposes only, results are superimposed on the MRI of one of

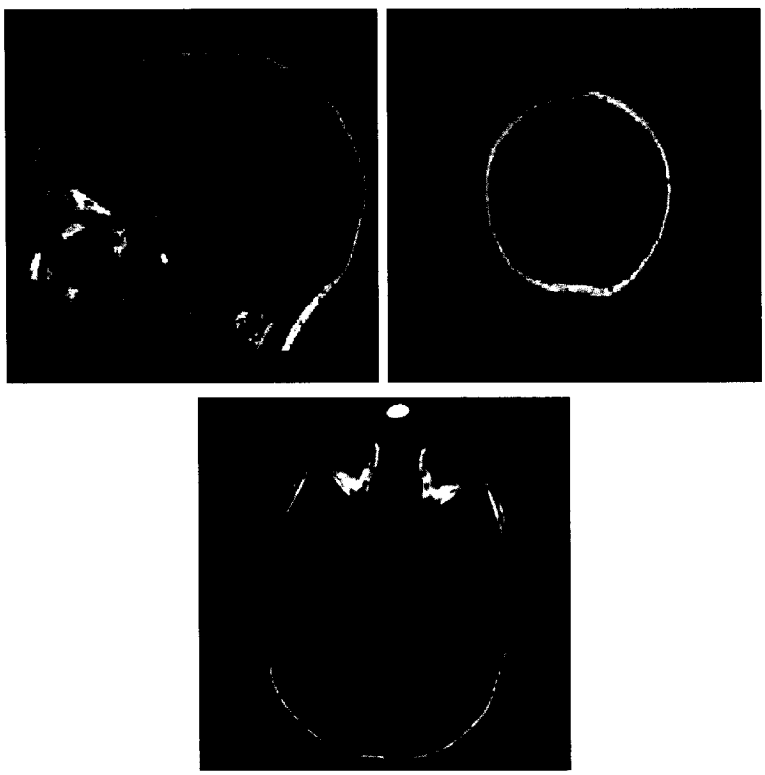

Figure 4.6: Dipole localization of N75 (orange dipole) and P100 (yellow dipole) from one participant during right hemifield stimulation.

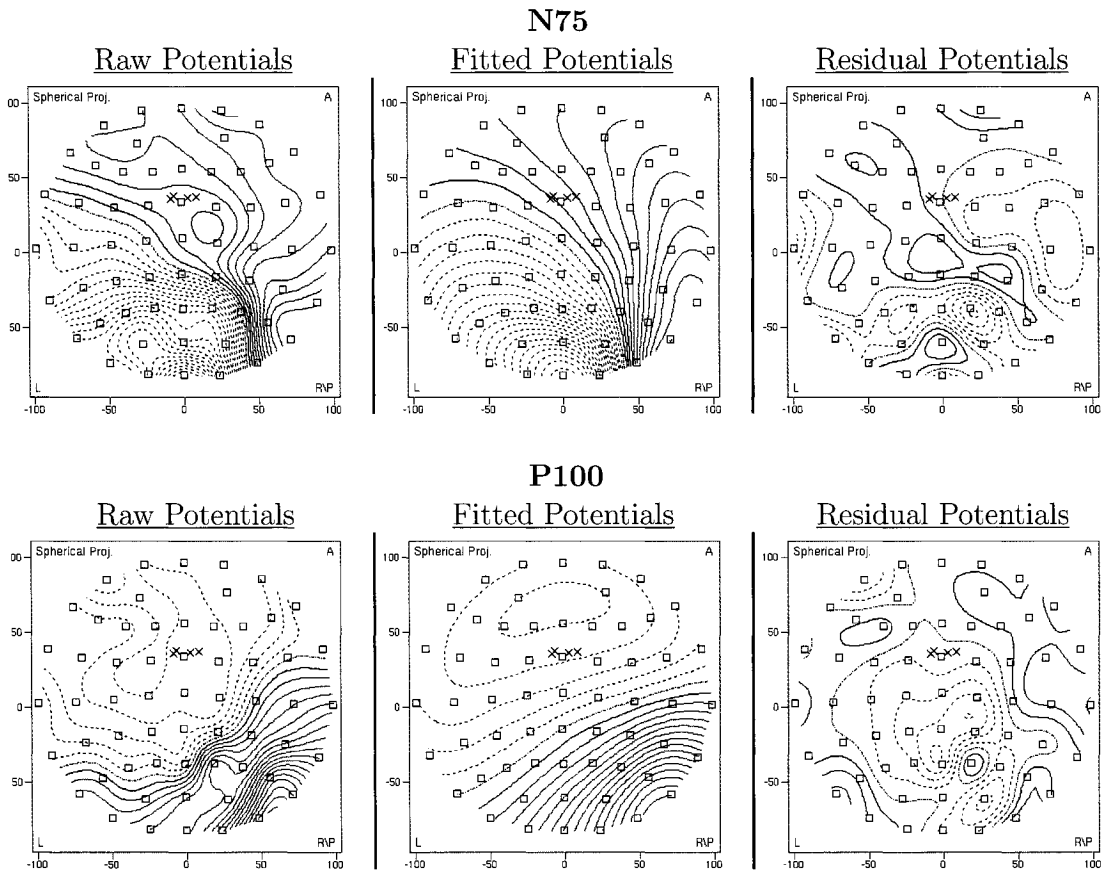

Figure 4.7: Overhead view of raw, fitted and residual potential maps of the N75 and P100 after dipole localization from one participant during left hemifield stimulation. The raw potentials are shown on the left, the fitted potentials are shown in the middle and the residual potentials are shown on the right. For this participant, the fitted maps of the N75 and P100 explained 94% and 96% of the raw maps, respectively.

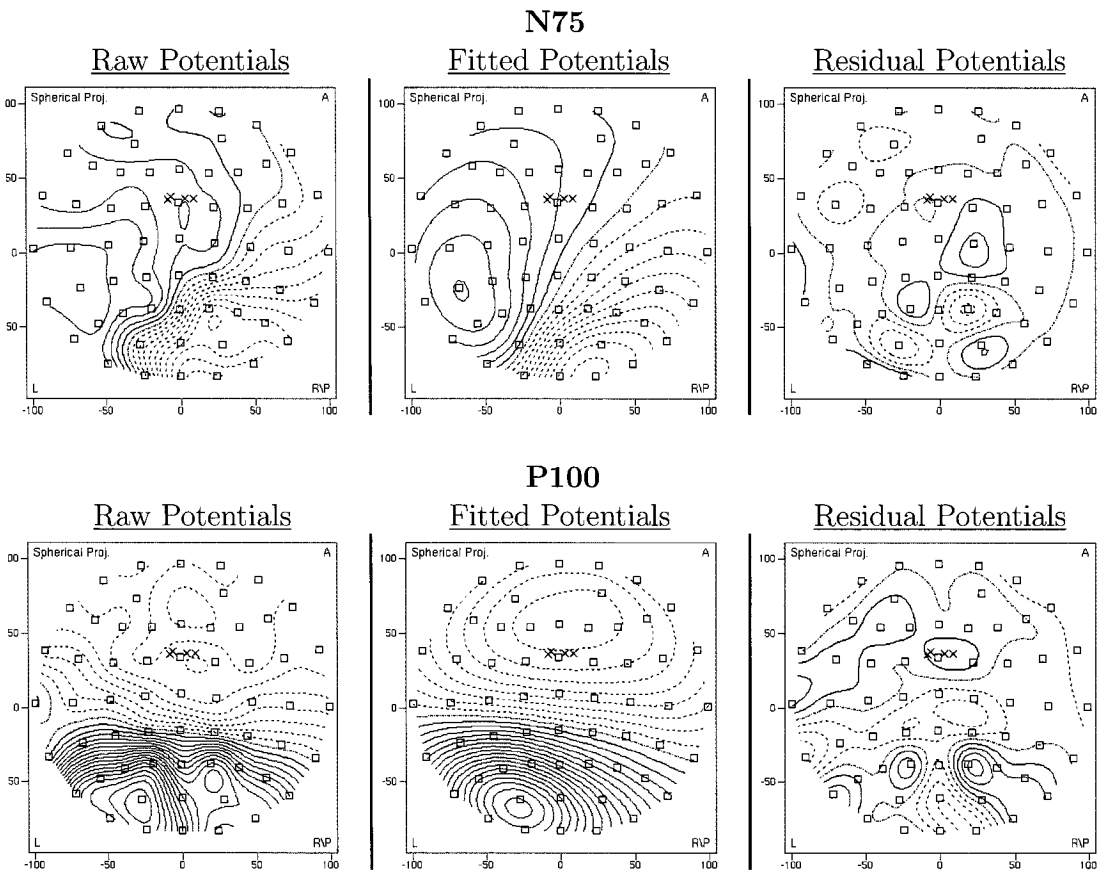

Figure 4.8: Overhead view of raw, fitted and residual potential maps of the N75 and P100 after dipole localization from one participant during right hemifield stimulation. The raw potentials are shown on the left, the fitted potentials are shown in the middle and the residual potentials are shown on the right. For this participant, the fitted maps of the N75 and P100 explained 96% and 97% of the raw maps, respectively.

Figure 4.9: FMRI response showing the positive **BOLD** (red) and negative **BOLD** (blue) from one participant during left hemifield stimulation. Results are similar for right hemifield stimulation (not shown). The FMRI map is thresholded to $p \leq 10^{-4}$

the participants. The generator(s) representing the N150 component is not displayed (see discussion).

	Left Hemifield Stimulation (x, y, z)	**Right Hemifield Stimulation** (x, y, z)
N75	-26.4, 61.3, 44.2 (11.7, 12.3, 18.5)	7.5, 65.7, 49.6 (11.7, 11.3, 17.1)
P100	-25.6, 52.0, 62.4 (7.5, 14.7, 11.3)	9.5, 55.0, 53.1 (12.5, 17.2, 22.5)
+BOLD	-17.1, 69.3, 49.0 (11.7, 6.8, 5.5)	23.3, 69.4, 46.6 (9.1, 11.6, 8.8)
-BOLD	-9.0, 54.9, 54.6 (5.9, 7.2, 7.6)	6.5, 56.1, 48.1 (6.1, 8.7, 6.6)

Table 4.1: Locations (mm) of N75 and P100 VEP components and positive and negative FMRI COA averaged over all subjects. Standard deviations are shown in parenthesis below each mean.

In all participants, the voxels with the highest positive correlation coefficients were found near the most posterior portion of the calcarine fissure, contralateral to the stimulated visual field. Negative correlation values were also greatest on the contralateral side, anterior to the positive correlation values. We also investigated the possibility of FMRI signal habituation due to sustained prolonged visual stimulation. These effects were found to be minimal, and are consistent with previous studies

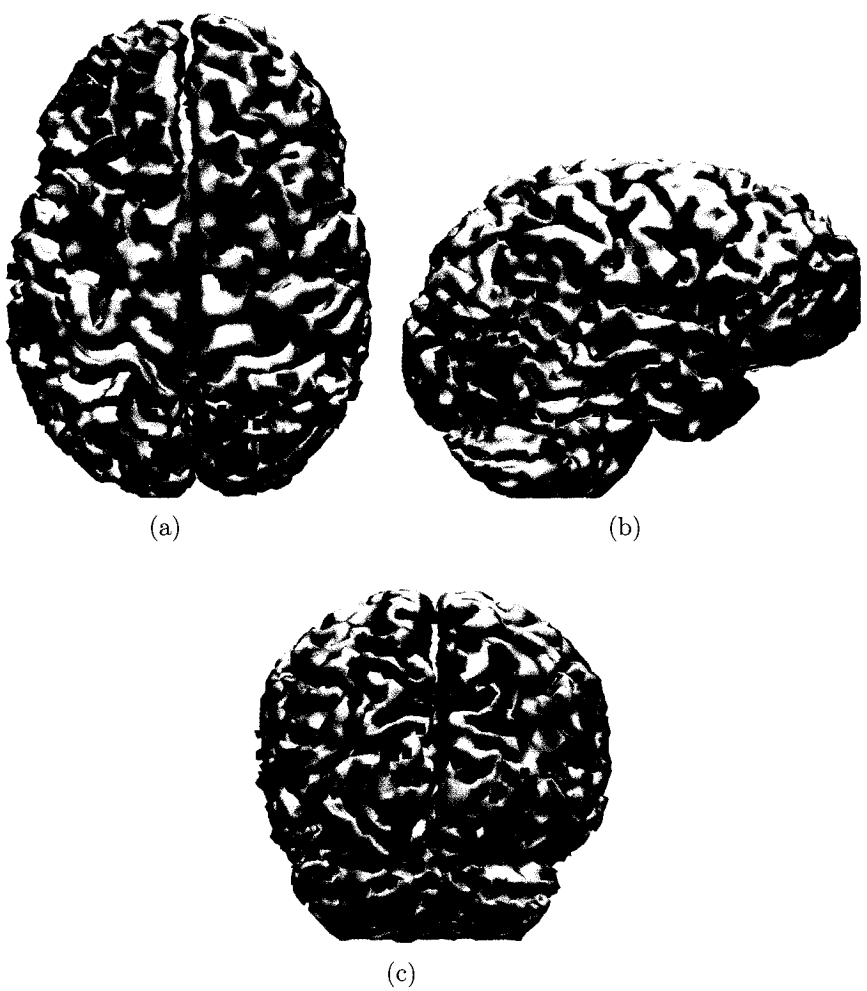

Figure 4.10: Dipole localization of the N75 (green cubes) and P100 (red cubes) VEP components (results from both left and right visual hemifield stimulation are shown). Results are superimposed on a reconstructed brain model. Axial (a), sagittal (b) and coronal (c) views are shown.

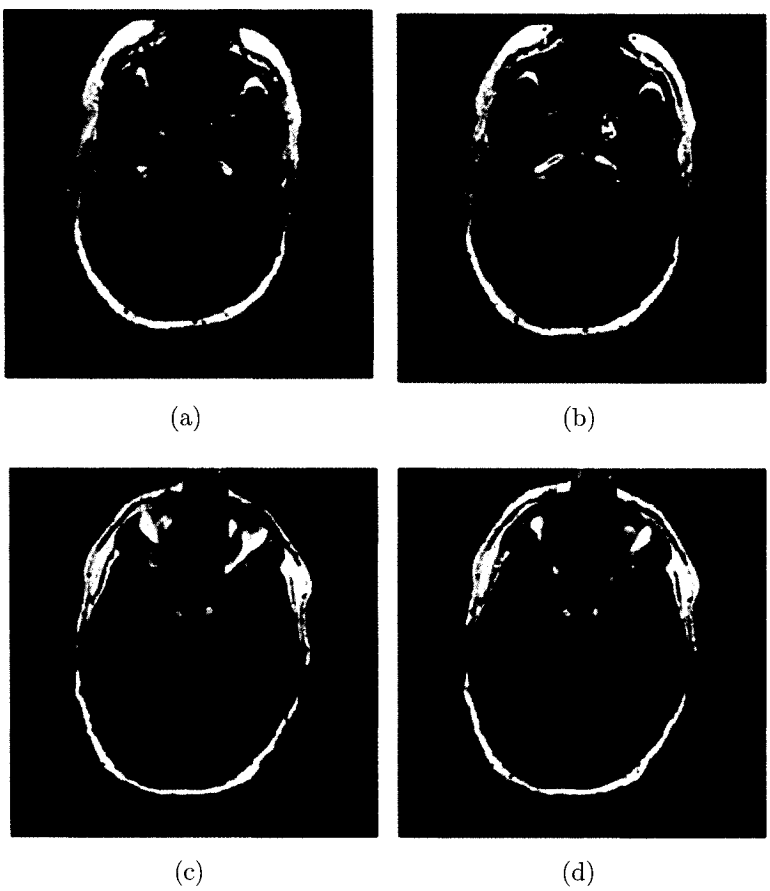

Figure 4.11: Axial views of group average FMRI maps. The peak positive response during left and right hemifield stimulation is shown in (a) & (b), respectively. The peak negative response during left and right hemifield stimulation is shown in (c) & (d), respectively. Maps are thresholded to $p \leq 10^{-5}$.

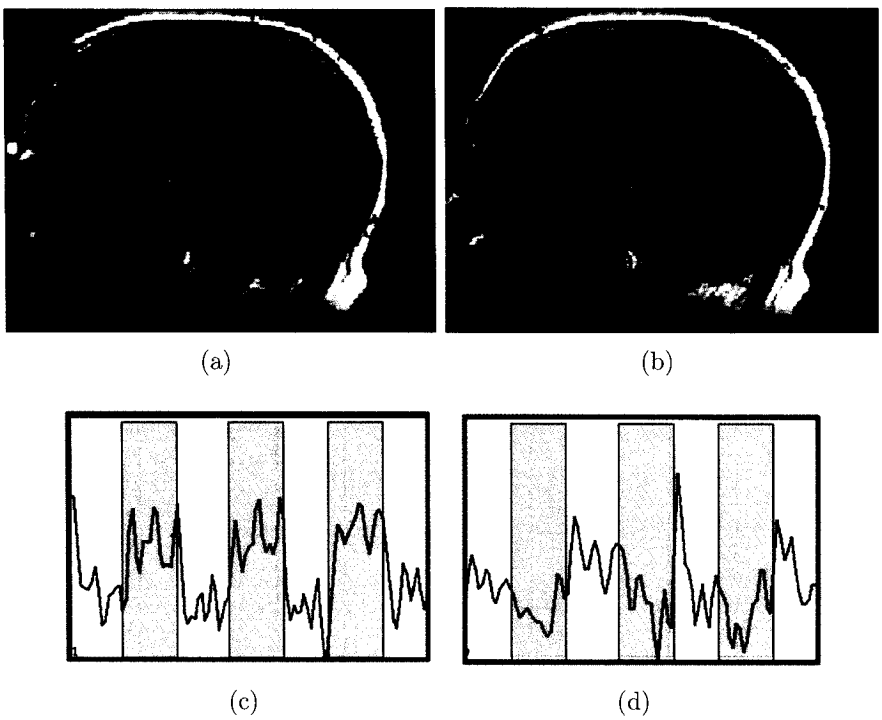

Figure 4.12: Sagittal view of group average FMRI maps showing the peak (a) positive and (b) negative response during left field stimulation (results during right field stimulation are similar, and are not displayed). Maps are thresholded to $p \leq 10^{-5}$. The mean FMRI signals ($\pm$**BOLD** response vs. time) extracted from the (c) positive and (d) negative ROI areas are also shown. Gray bars indicate periods of visual stimulation.

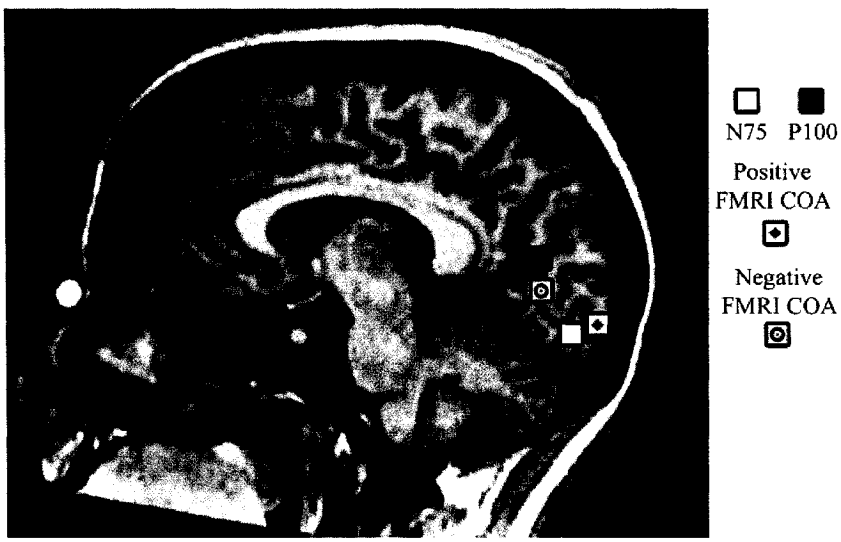

Figure 4.13: Mean localization over all subjects of N75 and P100 dipoles when using a realistic head model (white and black squares, respectively). Mean FMRI center of activity (COA) is shown for positive correlation (square with star) and negative correlation (square with circle). For display purposes only, results are superimposed on a mid-sagittal MRI from one participant.

using a reversing checkerboard stimulus [125, 126]. For the VEP, the y (running from anterior to posterior) and z (running from inferior to superior) coordinates of the N75 and P100 dipole positions were similar for left and right visual field stimulation, while the x (running from right to left) coordinate was significantly closer to midline during right visual field stimulation ($p \leq 0.01$). These VEP results were similar for both when the seed point was in the center of the brain and when limiting the inverse algorithm to the visual cortex. The sources of the VEP were localized in the primary visual cortex (V1), contralateral to visual stimulus field. The N75 component was localized near the most posterior portion of the calcarine fissure. The P100 component was also localized near the calcarine fissure, though significantly more anterior to the N75 source ($p \leq 0.05$). The average explained variance between the forward calculation and measured potentials of the N75 and P100 source was 91% and 94% respectively. The mean distance between the N75 and P100 was approximately 2.5±0.9cm. For comparison with previous VEP localization studies, we also used a spherical head model for localizing the N75 and P100. Here, the N75 source location was comparable to that obtained when using a realistic model. The P100 location obtained by the spherical model however was localized well outside V1, near V2/V3 (results not shown). This difference between results for spherical and realistic head models is not unexpected since spherical models perform worse for sources deeper in the brain [102, 127]. The mean FMRI signal extracted from the ROI surrounding the N75 dipole location is displayed in figure 4.14. Mean FMRI correlation values as a function of distance between N75 and P100 dipole positions are displayed in figure 4.15. The mean distance between the positive FMRI COA and negative FMRI COA was approximately 2.1±1.3cm. The location of positive and negative FMRI COA falls within the standard deviations of the mean N75 and P100 dipole position, respectively. Moreover, in seven of the eight subjects, the N75 was closest to the positive FMRI COA, while the P100 was closest to the negative FMRI COA in five subjects. Overall, the mean distance between the N75 and positive FMRI COA was approximately 2.0±1.0cm, while the mean distance between the P100 and the negative FMRI COA was approximately 3.0±1.6cm.

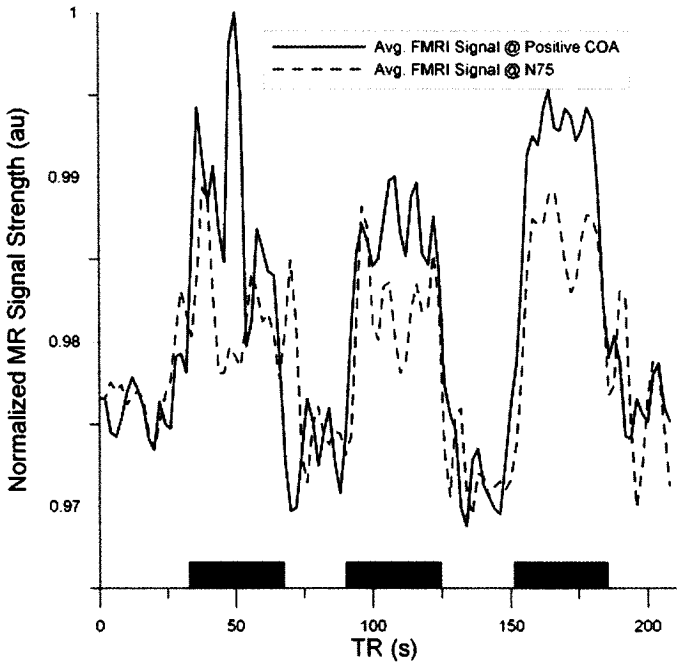

Figure 4.14: MR signal averaged over voxels in the positive FMRI COA (dark line) and N75 dipole ROI (light, dashed line). The ROI was modeled as a sphere with 7mm radius, and consisted of approximately 7 voxels each. Black rectangles indicate periods of visual stimulation. The smaller amplitude of the signal extracted from the N75 ROI is expected as is was not directly overlaid on the peak FMRI response area.

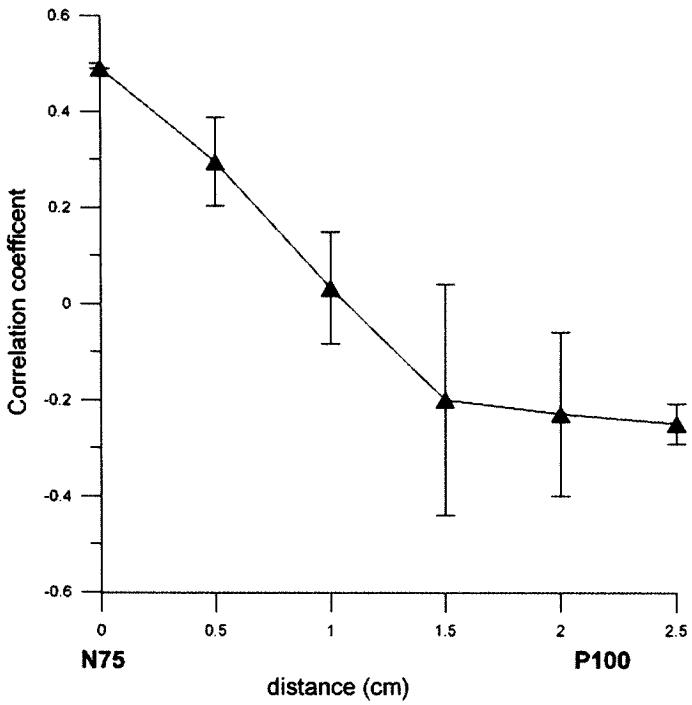

Figure 4.15: Mean correlation coefficient values from within ROI placed along the line joining N75 and P100 dipole position with an average separation of about 2cm. Values are averaged over left and right field stimulation. This mean correlation coefficient is positive for N75, negative for P100.

4.5 Discussion

Despite the large number of integrated ERP/FMRI studies, the spatial relationship of ERP and FMRI sources is still poorly understood. A recent animal study by Kim et al. [73] showed that, for relatively large voxels, the measured FMRI signal may accurately reflect the underlying neuronal activity. The measured ERP more directly reflects neuronal activity, but suffers from its limited spatial resolution, partly due to possible localization errors. In this study, localization errors are minimized by using subject specific VEP recordings with a high SNR, in conjunction with individually constructed realistic head models for dipole source modeling.

The results from this study provides strong support that the N75 generator is localized in area V1 of the visual cortex, confirming previous results [24, 25, 26]. In particular, our results indicate that for a pattern-reversal stimulus spanning 6° of the visual angle, the N75 source is located near the posterior portion of the calcarine fissure.

Several VEP reports have indicated that the P100 generator is located in area V1 [25, 26], but other VEP studies have argued that it may also originate in area V2/V3 [27], V3/V4 [28] and V5 [29]. Invasive studies using subdural electrodes by Noachtar et al. [30] reported that the P100 is most probably generated by a dipole source localized in close proximity of the calcarine fissure. Our results also indicate that the P100 dipolar source is near the calcarine fissure, but significantly anterior and slightly superior to the N75 generator ($p \leq 0.1$). The consistency of these findings across all subjects supports the evidence that the N75 and P100 sources are located in V1, though in substantially different locations within the calcarine fissure [128, 129].

Localizing the N150 component has proven to be difficult in the past. Some reports suggest that there may be up to two pairs of dipoles needed to correctly model this source [24, 29]. Our study was limited to a sole dipole source model only, and consequently localization of the N150 component is left for further study.

Our FMRI results showed areas in the visual cortex consisting of significant positive and **-BOLD** responses. The peak **+BOLD** response was in the posterior portion of the calcarine fissure, contralateral to the stimulus field. This is consistent with similar studies [130, 131]. A portion of the **-BOLD** response was found on the ipsilateral side, but peaked on the contralateral side. This is similar to the findings of Smith et

al. [64].

In seven of the eight subjects, it was found that the dipole source in the 65-85ms time range (N75) was localized closest to the peak positive FMRI activity. In the ROI surrounding the N75, we found voxels with a highly significant **+BOLD** response. The correlation coefficient of the positive FMRI signal quickly decreased as it approached the more anterior P100 dipole position, which is consistent with previous FMRI studies using checkerboard stimuli [131]. The correlation begins to turn negative approximately at the halfway point between N75 and P100 dipole locations. The area surrounding the P100 generator did not show any significant **+BOLD** activity, but contained voxels that exhibited a **-BOLD** response.

The results presented here suggest a strong correspondence between the location of the N75 generator and the **+BOLD** response, but not for the P100 and the **+BOLD** response which was also reported by Di Russso et al. [24]. In this study, we found that in the majority of subjects, the location of the P100 generator corresponded better to the location of the peak **-BOLD** response.

Studies have indicated that the positive FMRI activity seen in **BOLD** based experiments is largely due to excitatory synaptic activity [59, 60, 61]. Initial studies argued that the **-BOLD** response was be due to 'vascular stealing'. This theory suggests the elevation of blood flow at the activated location causes reductions in blood supply in nearby areas sharing the same blood vasculature, suggesting that negative hemodynamic changes have no neural correlate [62, 63]. More recent studies have provided evidence against this hypothesis [64], suggesting it is mostly due to neuronal inhibition [65, 66]. Our study is consistent with this suggestion, as it has been suggested that the N75 and P100 represent excitatory and inhibitory processes, respectively [115].

4.6 Conclusion

The generators of the pattern-reversal visual stimulus were studied using VEP and FMRI measurements. With subject specific data and realistic head models, we were able to reliably separate the generators of the N75 and P100 components in distinct areas of the primary visual cortex. In the majority of subjects, we observed a correspondence between the peak **+BOLD** response and the N75 dipole location. The

location of the P100 on the other hand corresponded to an area in the brain containing a significant **-BOLD** response. The results from this study indicate that the negative BOLD response should be included when comparing ERP and FMRI sources.

Chapter 5

Spatial Relationship of ERP and FMRI Sources-II

5.1 Abstract

Together, Functional magnetic resonance imaging (FMRI) and event related potentials (ERPs) are tools that can be used to study brain activity with relatively good spatial and temporal resolution, respectively. However, the conditions under which the sources obtained by these modalities overlap is still poorly understood. Of particular interest is how a change in the source of a particular ERP component is reflected in the FMRI activation map. In this study, we use a pattern-reversal stimulus presented in the central (0-2°) and peripheral (2-8°) visual field. Dipole localization on the first two visual evoked potential (VEP) components (N75 & P100) is carried out using individually constructed realistic head models. FMRI recordings are carried out as well, and the position of the peak positive and negative response is recorded for both stimulus conditions. The position of the N75 dipole followed retinotopic mapping, as did the positive FMRI response. The P100 dipole position on the other hand, along with the location of the negative FMRI response remained relatively unchanged. These results are consistent with the results of the previous chapter, suggesting that the positive and negative FMRI responses may be linked to N75 and P100 VEP components, respectively.

5.2 Introduction

In the previous chapter, the correlation between the location of the VEP and FMRI sources were investigated. Overall, it was shown that the location of the N75 VEP component correlated well the location of the positive FMRI response, while the location of P100 correlated well with the location of the negative FMRI response. However, it should be noted that the calculated locations of the VEP sources are not without error. Even with the usage of highly refined realistic head models and subject

specific datasets with a high SNR, there still exists sources of error. One of the more dominant sources of error not addressed in the previous chapter is the effect of volume conduction on the inverse problem. It has been shown that dipole localization errors of up to 1cm can be expected if the conductivity and shape of the skull is not properly modeled [132]. This limitation in EEG source accuracy therefore makes it difficult to make definite conclusions about the neuro-vascular relationship through EEG/FMRI measurements, based on the location of such sources. The current study was therefore designed to investigate not only the overlap of the EEG/FMRI source *locations* , but also investigate the correlation between their respective source *sensitivities* to different stimulus conditions. It has been shown that the location of the N75 and P100 components respond differently under different stimulus conditions [133]. There have also been studies showing the sensitivity of the location of the positive BOLD response under different stimulus condition, yet little work to date has investigated such sensitivity profiles of the negative BOLD response. It is therefore of interest to examine how the change in the location of a particular VEP component is reflected in the location of both the positive and negative FMRI response. Based on the findings from the previous chapter, it is hypothesized the N75 and **+BOLD** source will be behave in a similiar fashion (the same is hypothesized for the P100 and the **-BOLD** source).

In this study, we use a pattern-reversal stimulus placed in the foveal and peripheral regions of the visual field. The position of the N75 and P100 VEP sources are estimated in both stimulus conditions, as is the location of the peak positive and negative FMRI responses. The observed displacements in the location of the VEP sources are then compared to the displacement in the positions of the positive and negative BOLD responses.

5.3 Methods

5.3.1 Subjects and stimulus

Ten healthy subjects with no history of neurological impairment were recruited for both EEG and FMRI recording sessions (mean age 23, range 20-28 years, 5 males). All subjects where right handed and had normal vision. Subjects were instructed to

fixate on a red fixation point located in the center of a black screen. The experimental task was a block design, consisting of 4 'on' and 5 'off' periods (figure 5.1). This task was used in order to have more statistical power in the analysis. During the 'on' block, a checker board was presented in the left hemifield and reversed at a rate of 2Hz. The checkerboard stimulus subtended either 2° x 2° (for foveal viewing) or 8° x 8° (for peripheral viewing) of the visual field. The peripheral stimulus was scaled larger than the foveal stimulus in order to target a similar cortical area elicited in the foveal condition [134]. The 'off' block consisted of a black screen with fixation point. The experimental task was repeated for both foveal and peripheral stimulus. FMRI and EEG data were acquired in separate sessions using the same experimental task. The sessions were balanced such that five subjects completed the FMRI first, while the remaining completed the EEG first. Sessions were no more than one week apart. Ethics approval was granted by the local regional ethics board.

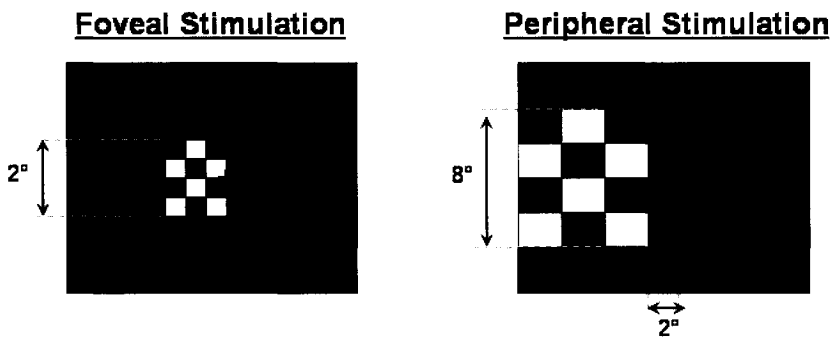

Figure 5.1: Experimental setup used for both EEG and FMRI recording sessions. Stimulus consisted of a 2Hz pattern-reversal checkerboard positioned in the foveal (left) and peripheral (right) regions of the left visual field. Subjects were instructed to maintain fixation on a cross in the center of the screen.

5.3.2 VEP Measurements, analysis and source localization

The VEP data were acquired and analyzed in the same manner as described section 4.3.2. Dipole localization was carried out in the same manner as described in section 4.3.3.

5.3.3 FMRI Measurements & analysis

FMRI measurements and analysis followed the same sequence as described in section 4.3.4. From this, the distance between FMRI COM in foveal and peripheral stimulus conditions for both **+BOLD** and **-BOLD** were calculated on a subject by subject basis.

5.4 Results

5.4.1 VEP Measurements

The mean foveal and peripheral VEP over all subjects for at electrode site Oz is shown in figure 5.2. The latency of the peak N75 was 76.2 $\pm$ 8.4ms and 69.5 $\pm$ 9.7ms for foveal and peripheral stimulation, respectively. The latency of the peak P100 was 104.2 $\pm$ 12.4ms and 97.3 $\pm$ 11.4ms for foveal and peripheral stimulation, respectively. Both N75 and P100 components were significantly shorter ($p \leq 0.005$) during peripheral stimulation, which is consistent with previous findings [21].

5.4.2 VEP source analysis

Dipole locations of the N75 and P100 components during foveal and peripheral stimulus conditions averaged over all subjects are displayed in figure 5.3. Detail are shown in table 5.1. In both foveal and peripheral stimulus conditions, the average location of the N75 and P100 sources were found to be in area V1 of the visual cortex. This is consistent with results from the previous chapter. For foveal stimulation, the N75 dipole was located in the posterior portion of V1, near the calcarine fissure. The P100 was also in V1, though more anterior along the calcarine fissure. In the peripheral stimulus condition, the N75 source was displaced 4.4 $\pm$ 1.2cm from its position in the foveal condition. The bulk of this change was in the anterior and superior directions, which is in accordance with previous VEP retinotopic mapping studies [119]. The P100 source on the other hand was less sensitive to stimulus position, moving an average of 2.4 $\pm$ 1.5cm from its estimated position in the foveal stimulus condition.

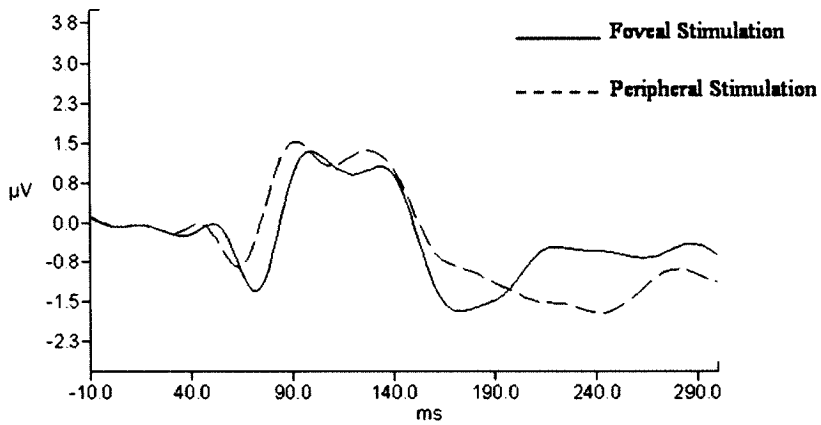

Figure 5.2: Mean VEP over all subjects measured at electrode Oz. The solid line is the response obtained during foveal stimulation, while the dashed line is the response obtained during peripheral stimulation.

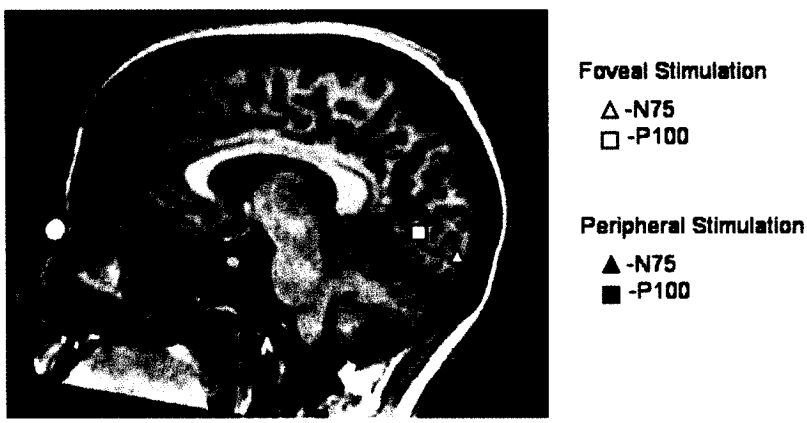

Figure 5.3: Mean localization over all subjects of N75 and P100 dipoles during foveal (white triangle/square) and peripheral (black triangle/square) stimulus conditions. For display purposes only, results are superimposed on a mid-sagittal MRI from one participant.

	Foveal Stimulation (x, y, z)	**Peripheral Stimulation** (x, y, z)
N75	-22.2, 54.9, 49.2 (15.8, 19.1, 18.1)	-25.7, 45.9, 64.2 (16.9, 12.7, 13.8)
P100	-27.6, 39.9, 60.1 (15.1, 16.5, 15.7)	-22.5, 34.6, 66.4 (15.5, 10.3, 11.0)

Table 5.1: Locations (mm) of N75 and P100 VEP components. Standard deviations are shown in parenthesis below each mean. The coordinate system is the same as described in section 4.3.3.

5.4.3 FMRI source analysis

In the majority of cases the subjects demonstrated both a significant positive and **-BOLD** response (figure 5.4 & figure 5.5). The average FMRI signal obtained from 5mm radius spherical ROI surrounding these regions are shown in figure 5.6. Significant **+BOLD** responses were found in all subjects for both stimulus conditions. In the foveal stimulation condition, the average location of the peak positive FMRI response was located contralaterally, near the posterior portion of the calcarine fissure. In the peripheral condition, the peak positive response remained in the contralateral hemisphere, but was displaced 2.3 $\pm$ 0.8cm from its original location in the foveal stimulus condition. The bulk of this change was anteriorly, along the calcarine fissure. Details are shown in table 5.2.

	Foveal Stimulation (x, y, z)	**Peripheral Stimulation** (x, y, z)
+BOLD	-26.2, 54.9, 49.2 (7.7, 7.1, 7.1)	-28.7, 49.9, 64.5 (6.9, 6.4, 8.3)
-BOLD	-24.7, 42.4, 57.1 (5.7, 6.8, 8.4)	-29.4, 43.6, 56.4 (9.9, 11.5, 8.9)

Table 5.2: Locations (mm) of positive and negative FMRI COA averaged over all subjects. Standard deviations are shown in parenthesis below each mean.

Unlike the positive response, the **-BOLD** response varied a great deal in both intensity and extent between subjects. In some cases the negative response was virtually nonexistent while in others it was far more intense and encompassed a larger

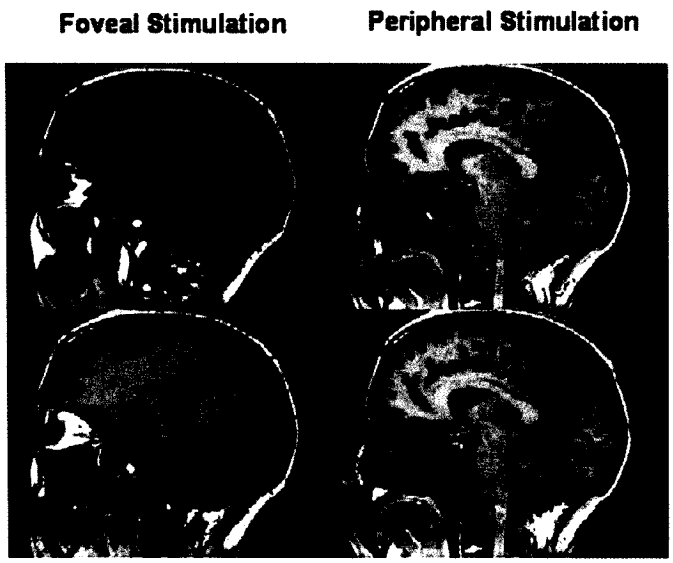

Figure 5.4: Sagittal views of negative (blue) and positive (red) **BOLD** responses averaged over all subjects. Maps on the left are from foveal stimulation. Maps on the right are from the peripheral stimulus condition.

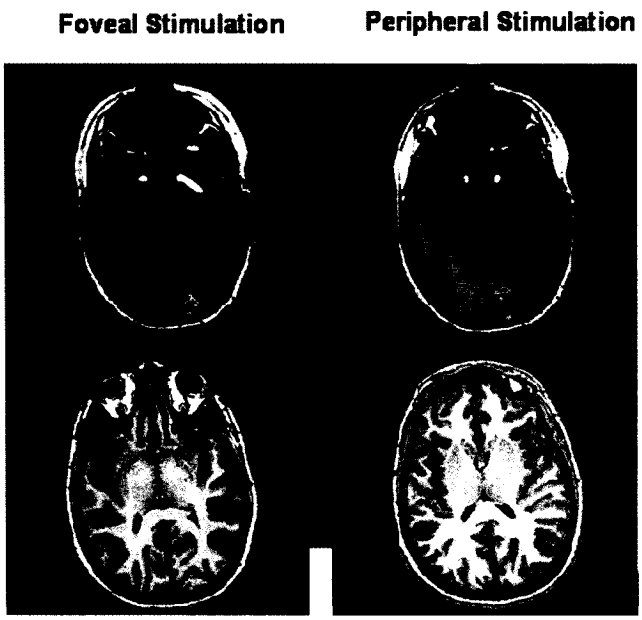

Figure 5.5: Axial views of negative (blue) and positive (red) **BOLD** responses averaged over all subjects. Maps on the left are from foveal stimulation. Maps on the right are from the peripheral stimulus condition.

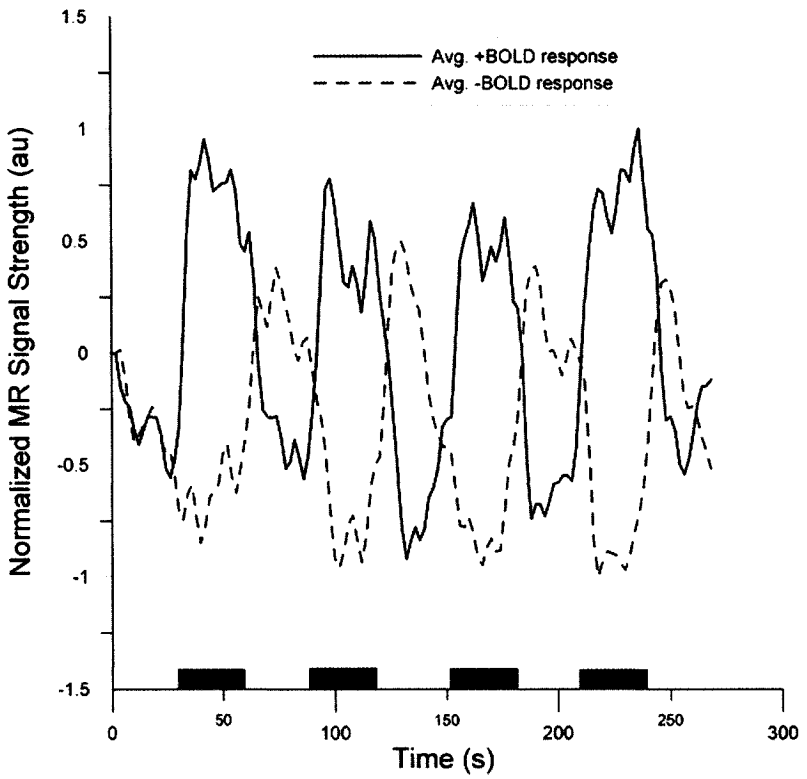

Figure 5.6: Mean FMRI signal extracted from ROIs placed around areas reflecting the positive (solid line) and negative (dashed line) BOLD response during foveal stimulation. Results are similar for peripheral stimulation. Black rectangles indicate periods of visual stimulation.

region than the positive response. The majority of subjects displayed a strong **-BOLD** response within the ipsilateral visual cortex during foveal stimulation. During peripheral stimulation, this large ipsilateral activation was greatly reduced, and vanished altogether in some subjects (figure 5.7). For both foveal and peripheral stimulus conditions, a region of activation was observed on the contralateral side of the brain, anterior to the positive activation though still in the V1. Two locations for this activation were generally observed, the first at the Parietal-occipital/calcarine fissure juncture, and the second directly inferior to this, slightly above the cerebellum. During the peripheral stimulus condition, the contralateral activation was reduced, but not to the same extent as the ipsilateral response. The average difference in the location of the contralateral negative response between the two stimulus conditions was 1.0 $\pm$ 0.6cm mm. Details of the magnitude of the distance for both VEP and FMRI sources are listed in Table 5.3.

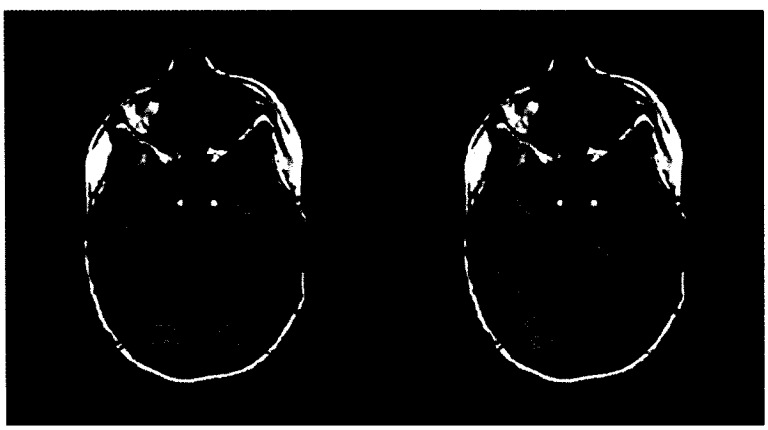

Figure 5.7: **-BOLD** response measured in one subject during foveal (left) and peripheral (right) visual stimulation. The ipsilateral response is dramatically reduced in the peripheral stimulus condition.

5.5 Discussion

The aim of this study was to observe how changes in the VEP are reflected in the FMRI response. Dipole localization of the first two VEP components (N75 & P100) was carried out for foveal and peripheral stimulus conditions. The location of the peak

	N75	P100	+BOLD	-BOLD
Subject 1	34.8	16.5	26.6	12.4
Subject 2	58.6	31.8	33.1	4.6
Subject 3	41.8	24.8	17.0	16.4
Subject 4	30.8	44.8	20.9	6.0
Subject 5	41.3	34.0	21.7	2.0
Subject 6	47.1	44.1	20.0	18.1
Subject 7	47.3	31.9	30.4	7.5
Subject 8	49.7	4.0	N/A	N/A
Subject 9	67.7	7.2	8.5	4.7
Subject 10	30.4	10.6	13.9	16.0
Average	45.0	25.0	21.3	9.7
S.D	11.9	14.8	7.8	6.0

Table 5.3: Displacement (mm) of VEP and FMRI sources obtained between foveal and peripheral stimulus conditions.

positive and **-BOLD** response was also obtained in similar experimental conditions. The difference between these VEP and FMRI source locations was noted in each stimulus condition.

Overall, the results from the VEP source analysis are consistent with those from the previous chapter. These results indicate that the N75 and P100 generators are located in the area V1 of the primary visual cortex. In the foveal stimulus condition, the N75 dipole was posterior to the P100 dipole in eight of the ten subjects. This was also seen in all subjects in the peripheral stimulus condition. By changing from foveal to peripheral stimulus conditions, the N75 and P100 moved according to the retinotopic mapping of the visual cortex, which is consistent with previous VEP source localization studies [135, 119]. However, the N75 dipole was much more sensitive to stimulus location compared to the P100 ($p \leq 0.001$). This reduced sensitivity of the P100 as compared to N75 has also been reported in previous studies [136]. A similar study by Brecelj et al. [137] reported that the P100 moved approximately 1cm anteriorly during peripheral stimulation as compared to foveal stimulation. Alfors et al. [138] reported no P100 movement in either stimulus condition. These studies did not report the location of the N75 source. In our study, the N75 was displaced more than the P100 in nine of the ten subjects. On average, the N75 source moved approximately twice the distance the P100 moved between foveal and peripheral stimulation

conditions.

The FMRI results from this study also show a similar finding. In seven subjects, the **+BOLD** response was displaced further than the **-BOLD** response. The location of the peak **+BOLD** response was consistent with retinotopic mapping FMRI studies [130]. During foveal stimulation, a peak positive and negative response could be found contralaterally. A larger, more disperse negative response was also found ipsilaterally. These results are consistent with Smith et al. [64]. During peripheral stimulation, the peak positive response moved in accordance with retinotopic mapping. The contralateral negative response was not significantly displaced, while the ipsilateral negative response was dramatically reduced, and in some subjects vanished all together. This has also been reported by Shmuel et al. [62]. The notion that the **-BOLD** response is simply a shifted **+BOLD** response would imply that the **+BOLD** is delayed by 1min in some areas of the brain, which is unlikely. Overall, the peak **+BOLD** response moved approximately two times as much as the peak negative response did for the foveal and peripheral stimulus conditions. It should be noted that since the ipsilateral activation was not seen for both stimulus conditions in all subjects, this study was limited to observing the effects of stimulus location solely on the contralateral positive and **-BOLD** response. Further work is needed to study the sensitivity of the ipsilateral **-BOLD** response.

5.6 Conclusions

The source locations of the first two VEP components (N75 & P100) were estimated during foveal and peripheral stimulation. The location of the peak positive and negative FMRI response was also investigated under these experimental conditions. The results indicate that the position of the N75 and **+BOLD** sources were more sensitive to stimulus location than the position of the P100 and **-BOLD** sources, respectively. By going from foveal to peripheral stimulus conditions, the position of the N75 and the **+BOLD** source moved approximately two times as much as the P100 and **-BOLD** source. This finding indicates that the source locations of the N75 and **+BOLD** response are more sensitive to stimulus location than the source locations of the P100 and **-BOLD** response. These results therefore suggest that the source of the N75 may be better linked to the source of the **+BOLD** response, while

the source of the P100 may be better linked to the source of the **-BOLD** response.

Chapter 6

Integration of ERP and FMRI for analysis of glaucoma

6.1 Physiological causes and effects of glaucoma

Inside the eyeball there are two fluid-filled sections separated by the lens. The larger, back section contains a clear, gel-like material called the vitreous humor. The smaller, front compartment contains a clear, watery material called the aqueous humor. The aqueous humor fills the space between the cornea and the iris. The aqueous humor is continually produced by the ciliary body, the part of the eye that lies just behind the iris. It is the pressure of this fluid that maintains the convex shape of the cornea. The aqueous humour allows nutrients to circulate through the inner layer of the cornea, and then drains into the blood stream via the canal of Schlemm.

An excess flow of aqueous humor caused by too much fluid entering the eye, or by the trabecular meshwork ('drain') getting clogged up can result in an increased intraocular pressure (IOP). Raised IOP is a significant risk factor for developing glaucoma. A normal IOP ranges between 11 and 21 mm Hg. However, there is no set threshold for IOP that can reliably detect the onset of glaucoma. While one person may develop glaucoma at a relatively low pressure, another person may have a high IOP for years and yet never develop glaucoma. The various types of glaucoma are categorized into groups based on progressive physiological changes to the eye(s). The most common types of glaucoma are open and closed angle glaucoma. Unlike closed angle glaucoma, which is often caused by too small a space between the cornea and the iris, patients with open angle glaucoma have a gradual blockage of aqueous outflow despite a seemingly open space (chamber angle) in the front of the eye. If left untreated, the subsequent increase in pressure can result in: (1) deformation and death of the ganglion cells, (2) cupping of the optic disc and (3) compression of the optic nerve [139]. Almost half of the ganglion cells may be lost before any abnormality shows up on visual field testing [140]. Death to the ganglion cell leads to **permanent** damage of the optic disc and resultant permanent visual field loss. Since

it is the axons of the ganglion cells that make up the optic nerve, their death causes interruptions in the electrical impulses from eye to visual cortex. This can result in damage to both the LGN and the visual cortex [141].

6.2 EEG and FMRI in glaucoma patients

Although a raised IOP is the most commonly used marker for monitoring the onset of glaucoma, it is far from being reliable. This makes it difficult for the ophthalmologist to make the diagnosis of glaucoma and recommend appropriate treatment. It is therefore important that methodologies are developed in order to detect the onset of glaucoma before the onset of significant vision loss. One such methodology is to observe how visual processing in the visual cortex is affected in glaucomatous eyes. The investigation of the VEP latency may be useful in detecting changes in optic nerve brought on by glaucoma. Studies using VEPs in glaucoma patients have shown that delays in the VEP can be apparent even before visual defects are reported [140]. The point at which the VEP latency becomes abnormal is difficult to define since there is such a high variability of the VEP signal from person to person [20].

The majority of studies measuring VEPs in glaucoma populations have focused their attention on the latency of the P100 [142, 143, 140] relative to healthy people. These latency delays are also influenced by the different stages in the evolution of glaucoma [144]. The effects of glaucoma on the P100 amplitude on the other hand seems to be unresolved, with one report finding a significant reduction in P100 amplitude in glaucoma patients [145], while another found no noticeable change in P100 amplitude [142].

The reason why the P100 is readily used in glaucoma studies is clear: the P100 component is more often easily identifiable than the N75 [20]. However, the results from the few studies that have solely investigated the N75 in populations with visual field defects suggest that the inclusion of the N75 may provide additional information in the evaluation of visual field defects [146, 147].

To date, few studies have looked at the effects of glaucoma on the FMRI signal. A study by Miki et al. [148] tested three glaucoma patients with extensive visual field defects in one eye and normal vision in the other. It was shown that the damaged eye resulted in lower FMRI activation as compared to the healthy eye.

In this chapter, we attempt to extend the findings by Miki et al. by incorporating VEP measurements. Interocular VEP and FMRI measurements are made on four glaucoma patients and two healthy age-matched controls. Comparisons between the healthy and damaged eye within patients may remove the variability obtained through common group comparison studies. The aim is to (1) ascertain that both VEP and FMRI are sensitive enough to detect visual field defects like glaucoma and (2) determine whether findings regarding the relationship between VEP and FMRI sources presented earlier in the thesis are similar to people with glaucoma. Based on the the findings presented thus far, and those put forth by Miki et al., it is hypothesized that the N75 component will be a better marker than the P100 in identifying glaucomatous eyes.

6.3 Methods

6.3.1 Subjects, stimulus, measurements & analysis

Subjects were recruited by Dr. Marcelo Nicolela, Department of Ophthalmology & Visual Sciences, Dalhousie University. Four subjects (mean age 66.3 years) with unilateral glaucoma were included in the study. Only patients whose vision was severely affected were included in the study. Prior to VEP/FMRI measurements, the patients vision was tested using the Humphrey 24-2 perimetry field analyzer. This test consists of showing white flashed in various regions of the patients visual field. The patient is instructed to press a button each time he/she sees a flash. A computer records the spot of each flash and if the patient pressed the button when the light flashed in that spot. The Humphrey 24-2 test point pattern includes 54 test points covering the central field out to 24 degrees with a grid of points 6 degrees apart. The white stimuli can be varied in intensity over a range of 51 decibels. The decibel (dB) value refers to retinal sensitivity, rather than stimulus intensity, with 0 dB corresponding to the maximum brightness of stimulus that the perimeter can produce, and 51 dB the minimum brightness the perimeter can produce. The dimmest stimulus that can be seen foveally by a young, well-trained observer is at most about 38 to 40 dB. Between 10 and 20 dB is the typical range of abnormal vision. Values below 0 dB imply that the patient is blind in the tested area of the visual field. These values can

be presented in numeric and gray-scale form (figure 6.1).

One of the better parameters to quantify visual field loss is the mean deviation (MD). This number represents an average loss in sensitivity of the visual field compared to that of age-matched controls. Since other diseases (such as cataracts) can affect the MD, only patients without significant cataracts were selected (usually, MD values less than 15 dB is considered as significant visual field damage). Three of the subjects were diagnosed with capsular glaucoma (CG), which is similar to open angle glaucoma, the other with chronic closed angle glaucoma (CAG). The perimetry maps from each patient is displayed graphically. Details of their diagnosis are shown in Table 6.1. Two age matched controls with no history of visual impairment were also included in the study (mean age 62.5 years). Both subjects were examined and tested for visual defects one year prior to this study. Perimetry maps from these subjects are not available.

Patient	**Diagnosis**	**IOP** (R/L)	**MD (dB)** (R/L)	**Visual field defects** (R/L)
Patient-I	CAG-right eye	42/17	-18.3/+1.13	Superior & inferior arcuate scotomas / Normal
Patient-II	CG-left eye	21/47	+0.15/-14.1	Normal / Inferior paracentral scotoma & superior nasal step
Patient-III	CG-left eye	26/43	+2.51/-5.9	Normal / Inferior arcuate scotoma & superior nasal depression
Patient-IV	CG-left	21/37	+0.31/-19.5	Normal / Superior and inferior arcuate scotomas

Table 6.1: Information regarding the patients visual field decencies in each eye. Interocular pressure (IOP) values are in millimeters of Mercury (mm Hg).

In order to make inter-occular comparisons, monocular stimulation was used instead of binocular. The stimulus consisted of 5x5 checks that spanned approximately 10°x10° of the left visual field only (resulting in peak activation in the right hemisphere). Each eye was tested independently, with an opaque eye patch placed on the other. Measurements were made on separate days. EEG measurements were made and analyzed in the same way as described in section 4.3.2. In each VEP sweep

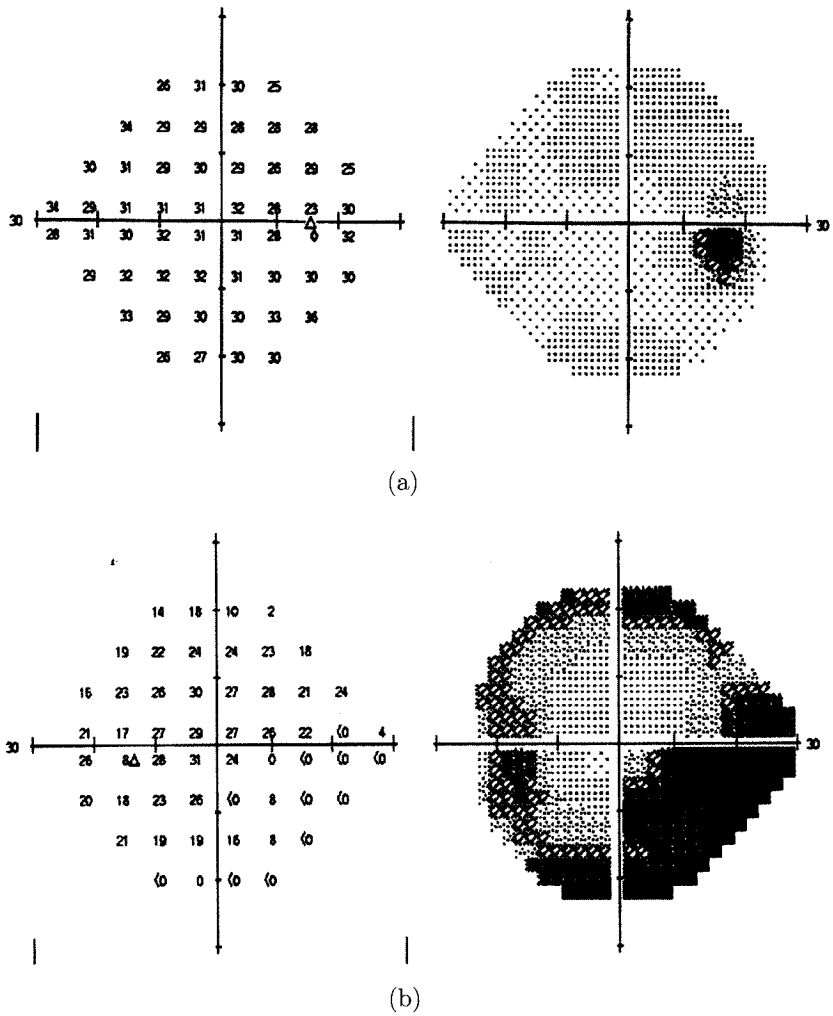

Figure 6.1: Perimetry maps that are represented numerically (left) and by grackle (right) taken from the healthy (a) and damaged (b) eye of one patient in this study. Dark areas in the grackle figure represent areas of the visual field that did not respond to the stimulus at that location (indicated as a <0 in the numerical map). The dark area in the healthy eye (a) is the patients blind spot, which is present in both healthy and damaged eyes.

(approximately 200 in total), the N75 and P100 components were identified by locating the peak negativity and positivity found in the 60-80ms and 90-110ms range, respectively. The N75 & P100 latency and amplitude were recorded in each sweep of the two stimulus conditions. For each subject, a Student's t-test was used to test whether the N75 & P100 latency and amplitude were significantly different in either condition (healthy vs. damaged eye). As an overall analysis, an analysis of variance ($ANOVA$) was then used to compare the group-average latency of the N75 & P100 components in either condition (healthy vs. damaged eye). In both the t-test and $ANOVA$, the level of significance was set to $\alpha = 0.05$. Dipole analysis (as described in section 4.3.3) was also carried out. These results are shown in the discussion.

FMRI measurements were also the same as described in section 4.3.4, with the slight exception that only voxels in the contralateral visual cortex with a correlation coefficient (CC) exceeding a threshold of ± 0.2 ($p \leq 0.001$) were retained. The total number and average CC of the positively correlated voxels (**+BOLD**) and negatively (**-BOLD**) correlated voxels that met the threshold criteria were noted. Finally, the FMRI signal from all the surviving voxels were averaged and the average % signal change was calculated relative to baseline. For each subject, a Student's t-test was once again used to test whether the average CC was statistically different in healthy and damaged eye stimulus conditions. The same was done for the % signal change of the (**+BOLD**) and (**-BOLD**) response in healthy and damaged eye stimulus conditions. As an overall analysis the $ANOVA$ was used to compare the group-average CC in either condition (healthy vs. damaged eye). In both the t-test and $ANOVA$, the level of significance was set to $\alpha = 0.05$.

The VEP and FMRI results are summarized in a brief subject-specific discussion and table provided at the end of each subject section. An overall discussion is given at the end of the chapter.

6.4 Results

6.4.1 Subject-NI

The first normal subject (NI) was a 59 year old female with no history of visual impairment in both eyes.

6.4.2 Results

The measured VEP of N75 is shown in figure 6.2. FMRI maps are shown in figure 6.3. The positive and negative FMRI signals averaged over all voxels surviving the threshold are shown in figure 6.4.

6.4.3 Discussion

Taken together, the VEP and FMRI results suggest that healthy participant NI had similar vision in both eyes. The latency and amplitude of the N75/P100 VEP components for both right and left stimulation are shown in figure 6.5. Statistical analysis (t-test) indicate that there were no significant differences in the latency and amplitude of the N75 and P100 components during left and right eye stimulation. Analysis of the FMRI data revealed an average CC of positively and negatively correlated voxels that was statistically identical in both eyes. Moreover, the average % signal change of the **+BOLD** signal was also similar in both eyes. These results suggest that similiar VEP and FMRI findings for both eyes are to be expected from monocular stimulation of subjects with normal vision. These VEP and FMRI results are summarized in Table 6.2.

	Left eye	**Right eye**
Avg. N75 latency (ms)	70.6	70.4
Avg. N75 amplitude (μV)	-1.8	-1.7
Avg. P100 latency (ms)	102.5	102.8
Avg. P100 amplitude(μV)	6.3	6.9
No. of **+BOLD** voxels	76	148
No. of **-BOLD** voxels	32	6
Avg. **+BOLD** CC	0.29	0.31
Avg. **-BOLD** CC	-0.27	-0.28
Avg. **+BOLD** signal change (%)	0.59	0.63
Avg. **-BOLD** signal change (%)	-1.46*	-0.76

Table 6.2: Summary of VEP and FMRI findings for healthy participant. The $*$ symbol indicates a significant statistical difference ($p \leq 0.001$). No symbol indicates no statistical difference.

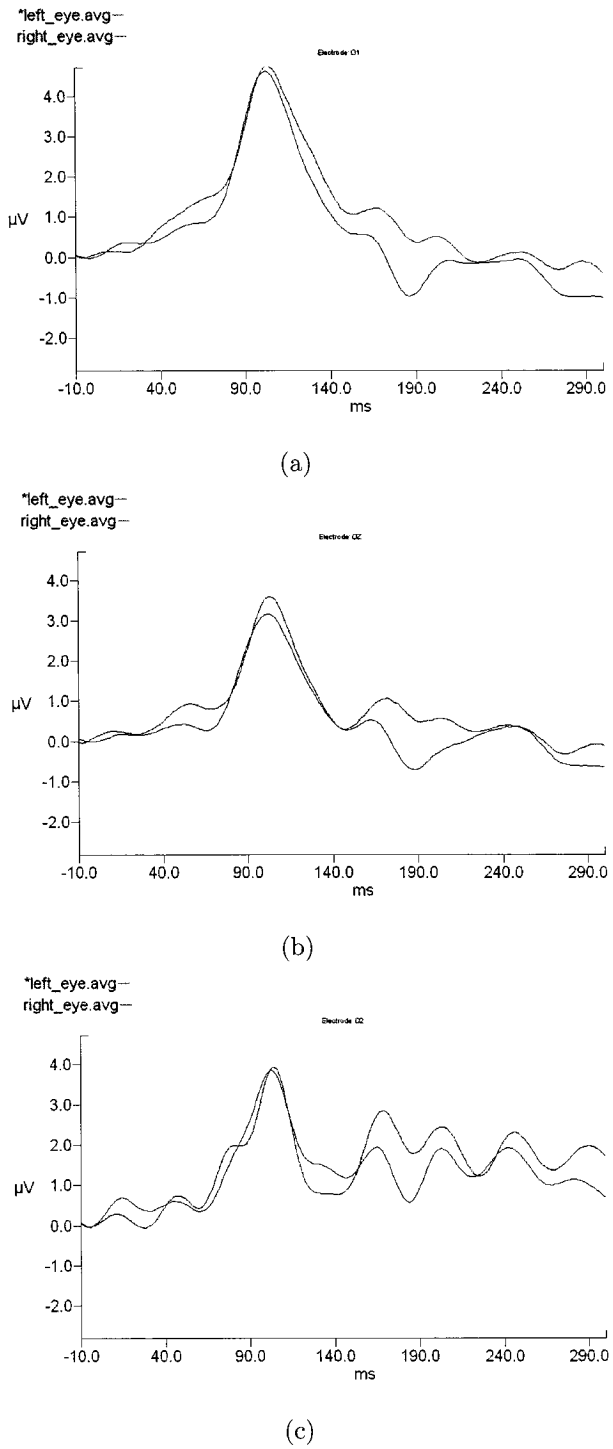

Figure 6.2: VEPs from the healthy subject-N1 as measured at electrode sites (a) O1, (b) Oz and (c) O2. Black traces are from left eye stimulation, red traces from right eye stimulation.

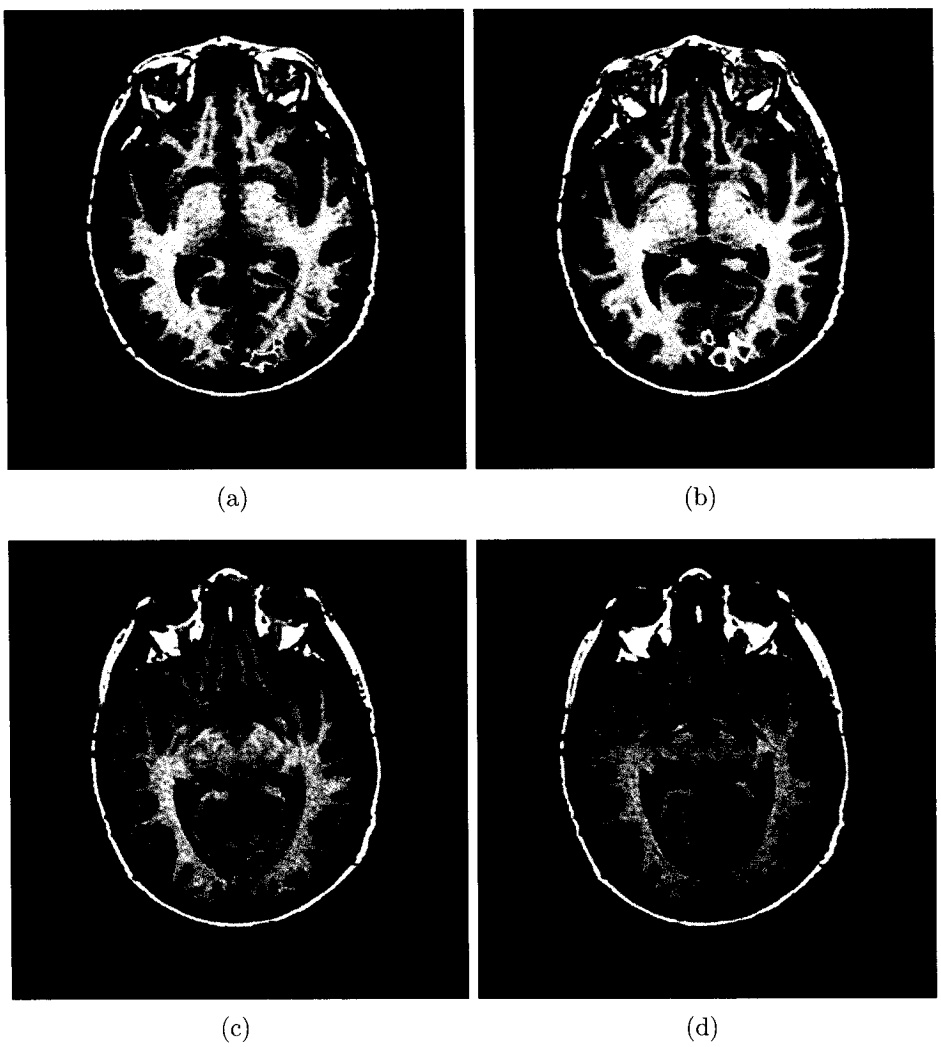

Figure 6.3: FMRI activation maps from subject-NI showing the dominant **+BOLD** response from the (a) left and (b) right eyes, as well as the dominant **-BOLD** response from the (c) left and (d) right eyes. Visual stimulation was presented in the left hemifield only, resulting in peak activation in the right hemisphere. Maps are thresholded to $p \leq 0.001$.

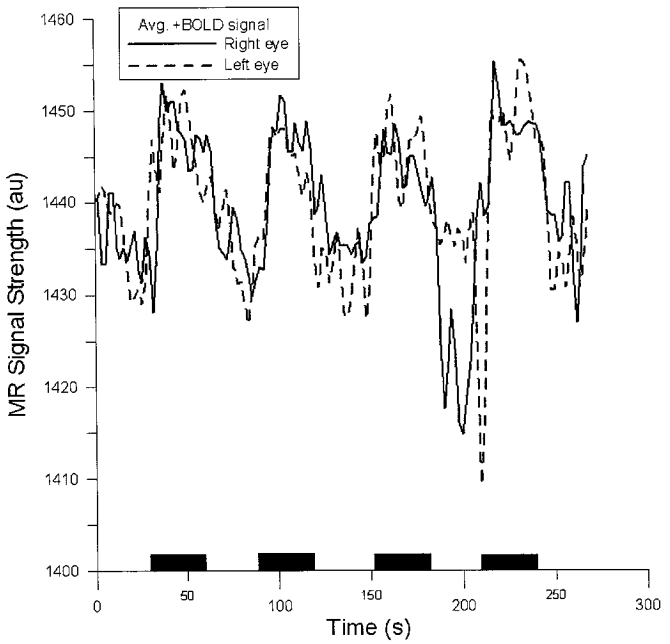

(a)

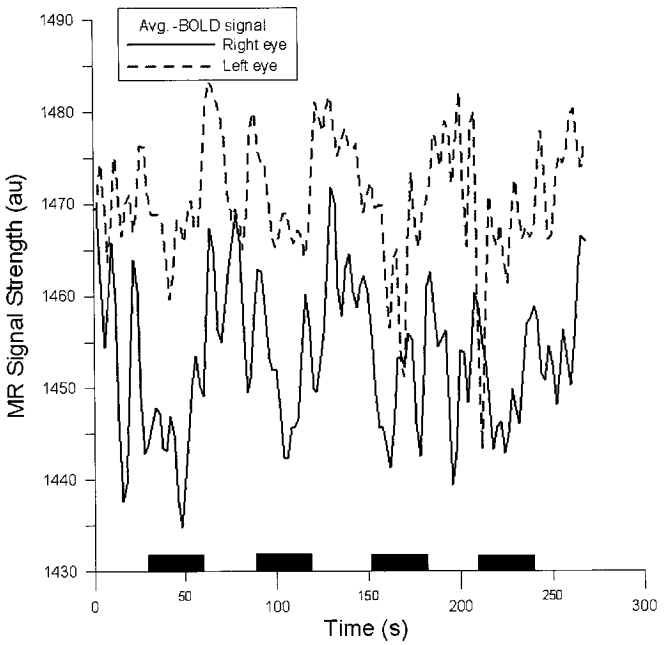

(b)

Figure 6.4: FMRI signal averaged over all significant voxels ($p \leq 0.001$) with (a) positive correlation and (b) negative correlation. Dark lines represent right eye stimulation, lighter dashed lines represent left eye stimulation. Black bars at the bottom indicate periods of visual stimulation.

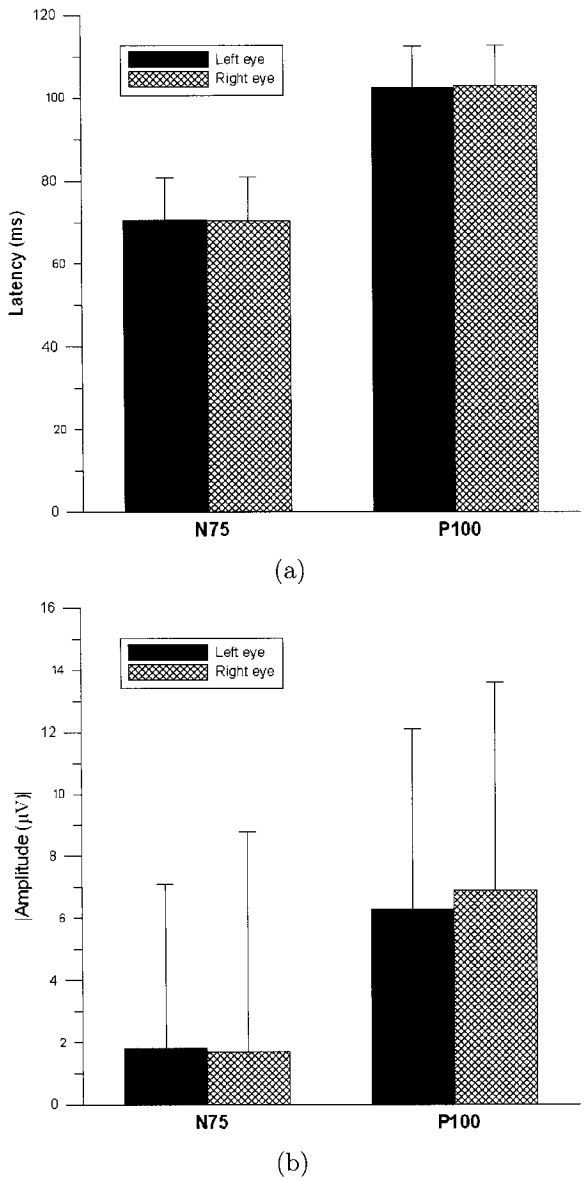

Figure 6.5: (a) The latency of the N75 and P100 components for the healthy participant are shown during right and left eye stimulation. (b) The amplitude of the N75 and P100 components during right and left eye stimulation. The standard deviations are denoted by the black error bars.

6.4.4 Subject-NII

The second healthy subject (NII) was a 65 year old female with normal vision in both eyes.

6.4.5 Results

The measured VEP of subject NII is shown in figure 6.6. FMRI maps are shown in figure 6.7. Due to the low number of voxels that survived the threshold, the mean FMRI signal is not shown for this subject.

6.4.6 Discussion

The FMRI results from the second healthy subject again show that that the average *CC* of +BOLD and **-BOLD** voxels are statistically identical in both eyes. However, it should be noted that there were very few **+BOLD** voxels that survived the modest threshold. This was expected, since the this subject showed no statistical evidence of an N75 component. This subject did on the other hand show a relatively robust P100 component and a -BOLD response. The P100 did not show any statistical difference in latency or amplitude in either eye (figure 6.8). These VEP and FMRI results are summarized in Table 6.3.

	Left eye	**Right eye**
Avg. N75 latency (ms)	N/A	N/A
Avg. N75 amplitude (μV)	N/A	N/A
Avg. P100 latency (ms)	94.4	93.7
Avg. P100 amplitude(μV)	5.9	6.3
No. of **+BOLD** voxels	5	3
No. of **-BOLD** voxels	14	14
Avg. **+BOLD** *CC*	0.25	0.27
Avg. **-BOLD** *CC*	-0.29	-0.28
Avg. **+BOLD** signal change (%)	N/A	N/A
Avg. **-BOLD** signal change (%)	N/A	N/A

Table 6.3: Summary of VEP and FMRI findings for the second healthy participant.

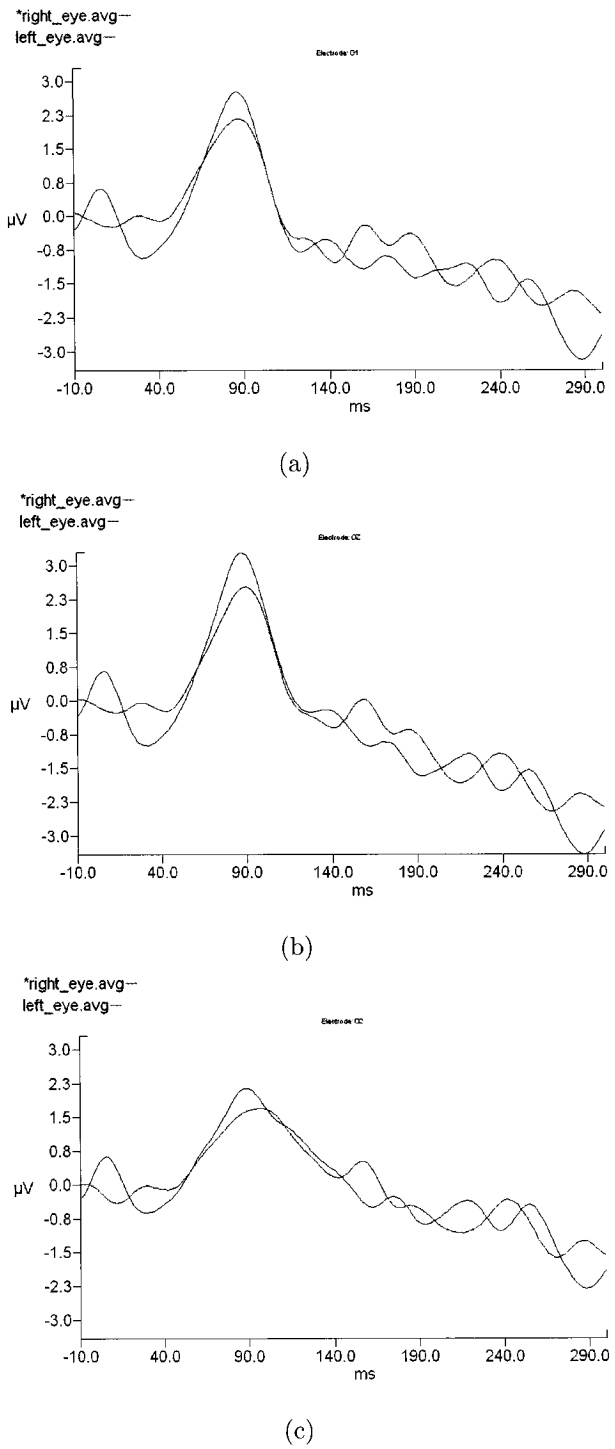

Figure 6.6: VEPs from the second healthy subject-NII as measured at electrode sites (a) O1, (b) Oz and (c) O2. Black traces are from right eye stimulation, red traces from left eye stimulation.

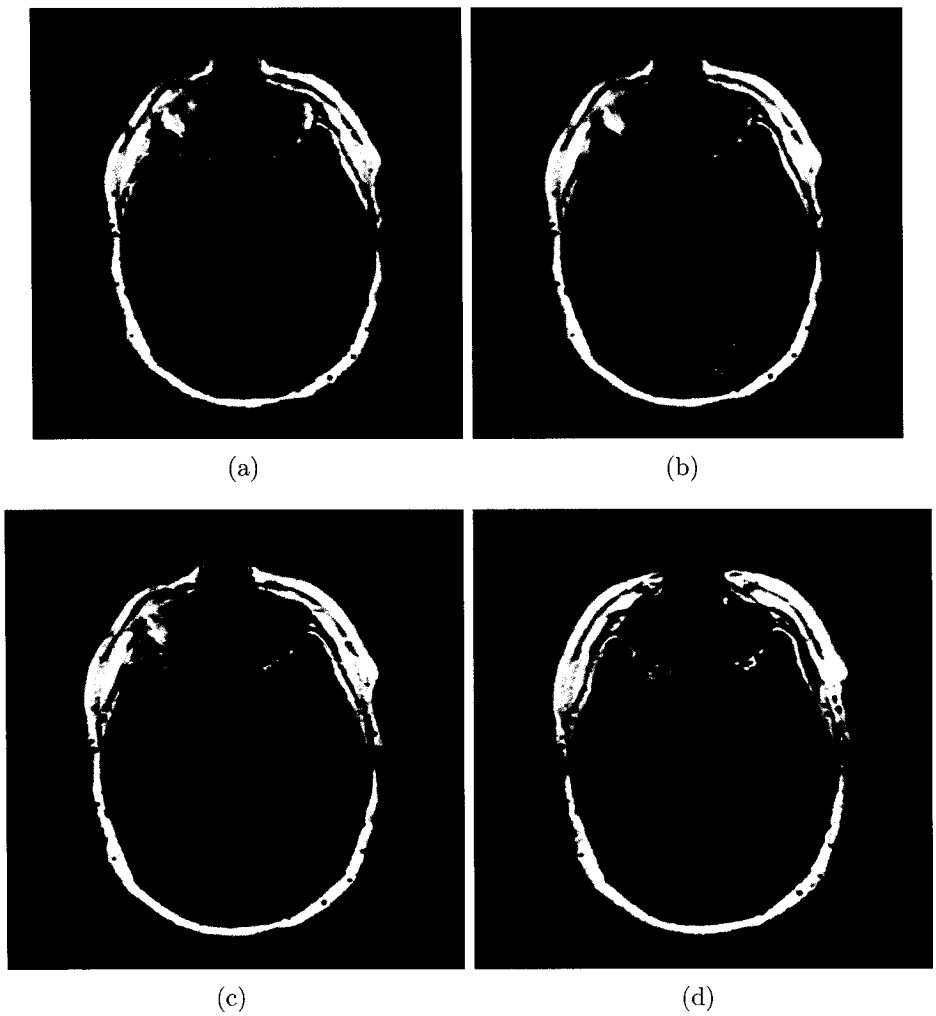

Figure 6.7: FMRI activation maps from healthy subject-NII showing the dominant **+BOLD** response from the (a) left and (b) right eyes, as well as the dominant **-BOLD** response from the (c) left and (d) right eyes. Visual stimulation was presented in the left hemifield only, resulting in peak activation in the right hemisphere. Maps are thresholded to $p \leq 0.001$.

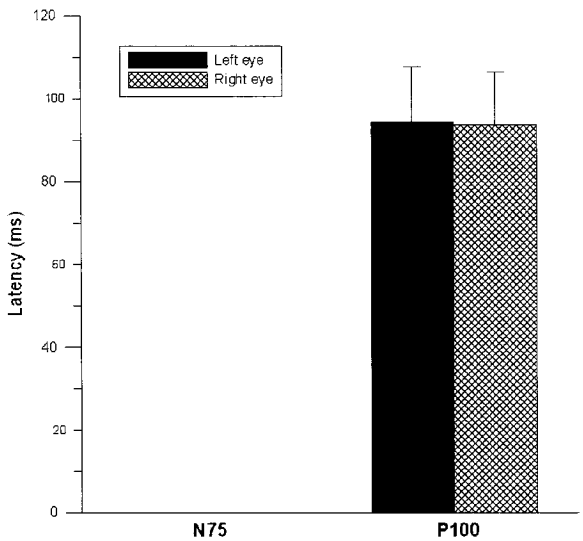

(a)

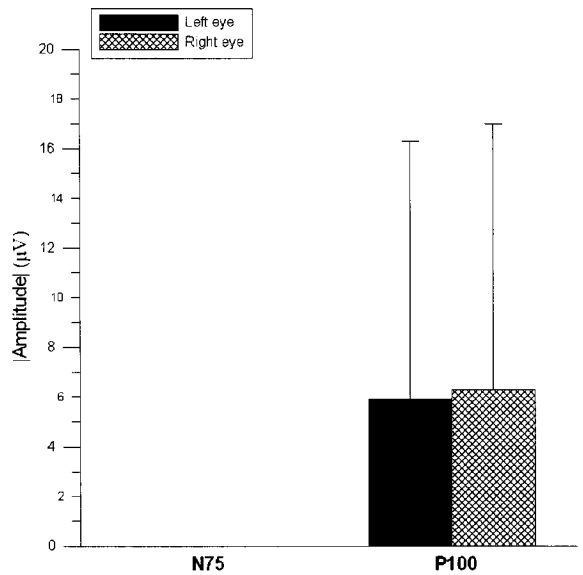

(b)

Figure 6.8: (a) The latency of P100 component for the second healthy participant are shown during right and left eye stimulation. (b) The amplitude of the P100 components during right and left eye stimulation. The N75 was not seen in this subject. The error bars represent the standard deviation.

6.4.7 Subject-PI

Patient-I was a 68 year old male. His left eye had a normal visual field, while the right eye showed considerable glaucomatous visual defects (figure 6.9).

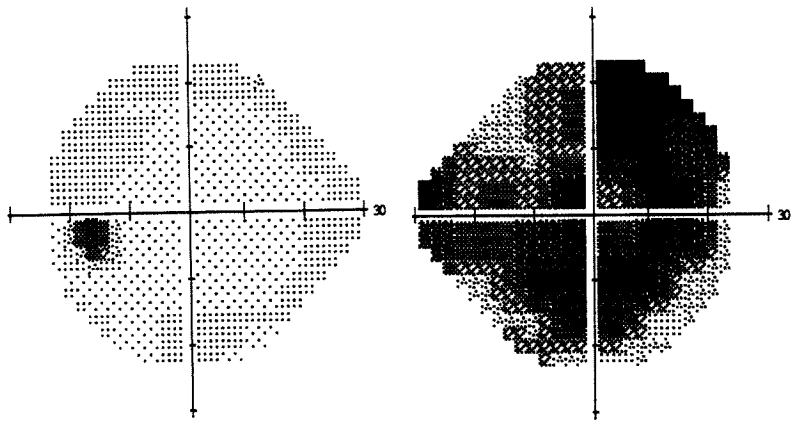

(a) Left eye (b) Right eye

Figure 6.9: Left and right eye perimetry maps obtained for Patient-I (Humphrey 24-2).

6.4.8 Results

The measured VEP of Patient-I is shown in figure 6.10. FMRI maps are shown in figure 6.11. The positive and negative FMRI signals averaged over all voxels surviving the threshold are shown in 6.12

6.4.9 Discussion

The VEP results obtained from Patient-I indicate that there was a significant difference in the healthy and damaged eye measurements. The VEP results from Patient-I show that the N75 was significantly delayed in the right eye compared to the left. No such significant delay was found for the P100. These results are shown in figure 6.13. The FMRI findings also indicate a measurable difference between eyes. When the left eye was stimulated, there were a total of 128 significantly positively correlated voxels compared 63 when the right eye was stimulated. The average CC of voxels activated during left eye stimulation was also significantly greater than that observed in the

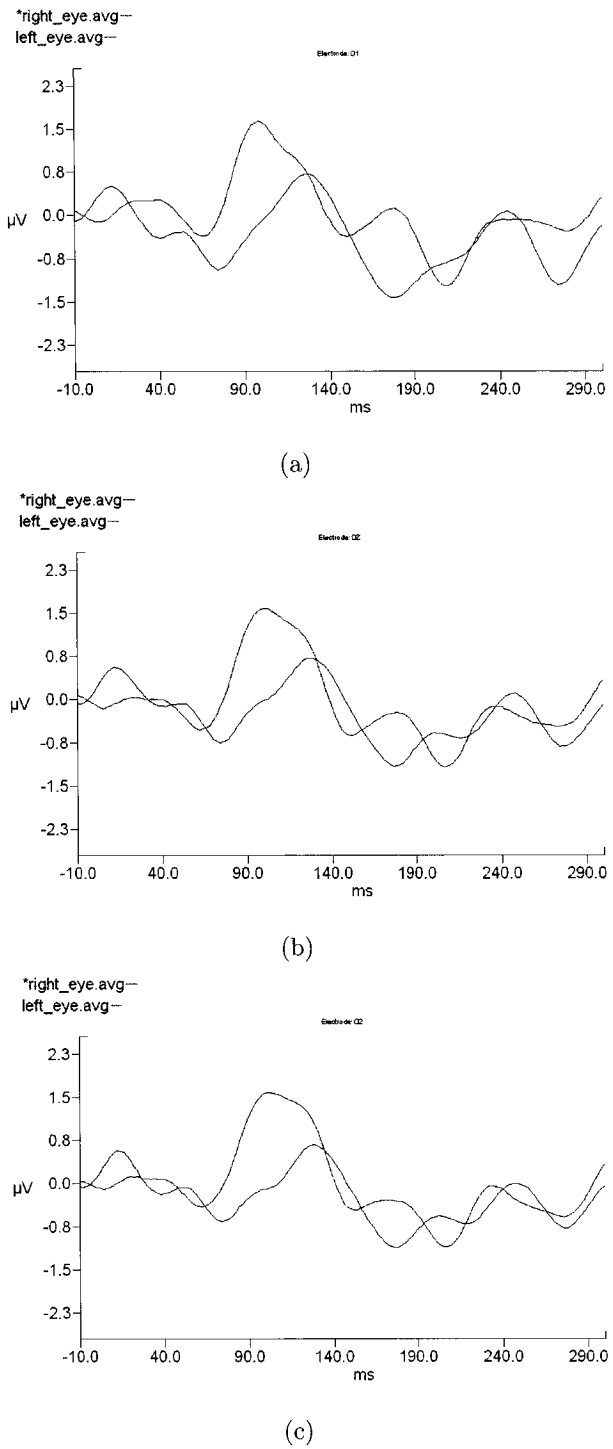

Figure 6.10: VEPs from Patient-I as measured at electrode sites (a) O1, (b) Oz and (c) O2. Black traces are from right eye stimulation, red traces from left eye stimulation.

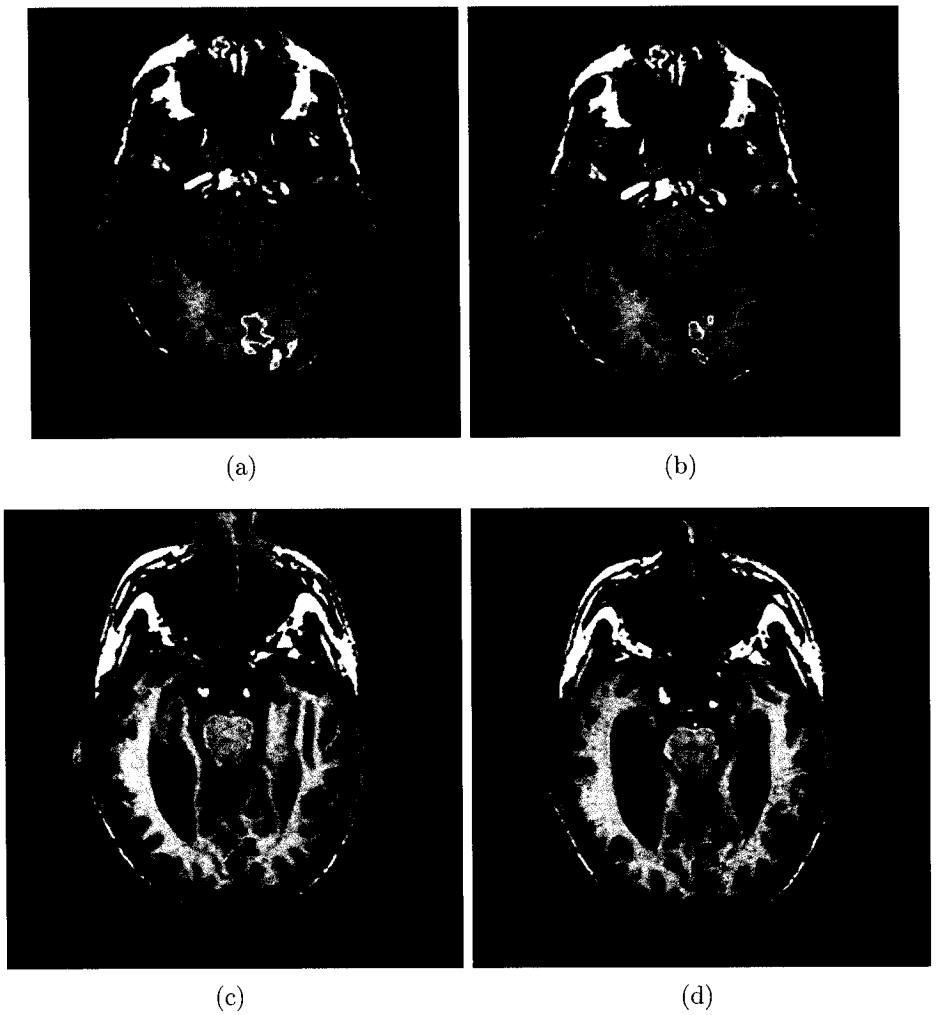

Figure 6.11: FMRI activation maps from Patient-I showing the dominant **+BOLD** response from the (a) left and (b) right eyes, as well as the dominant **-BOLD** response from the (c) left and (d) right eyes. Visual stimulation was presented in the left hemifield only, resulting in peak activation in the right hemisphere. Maps are thresholded to $p \leq 0.001$.

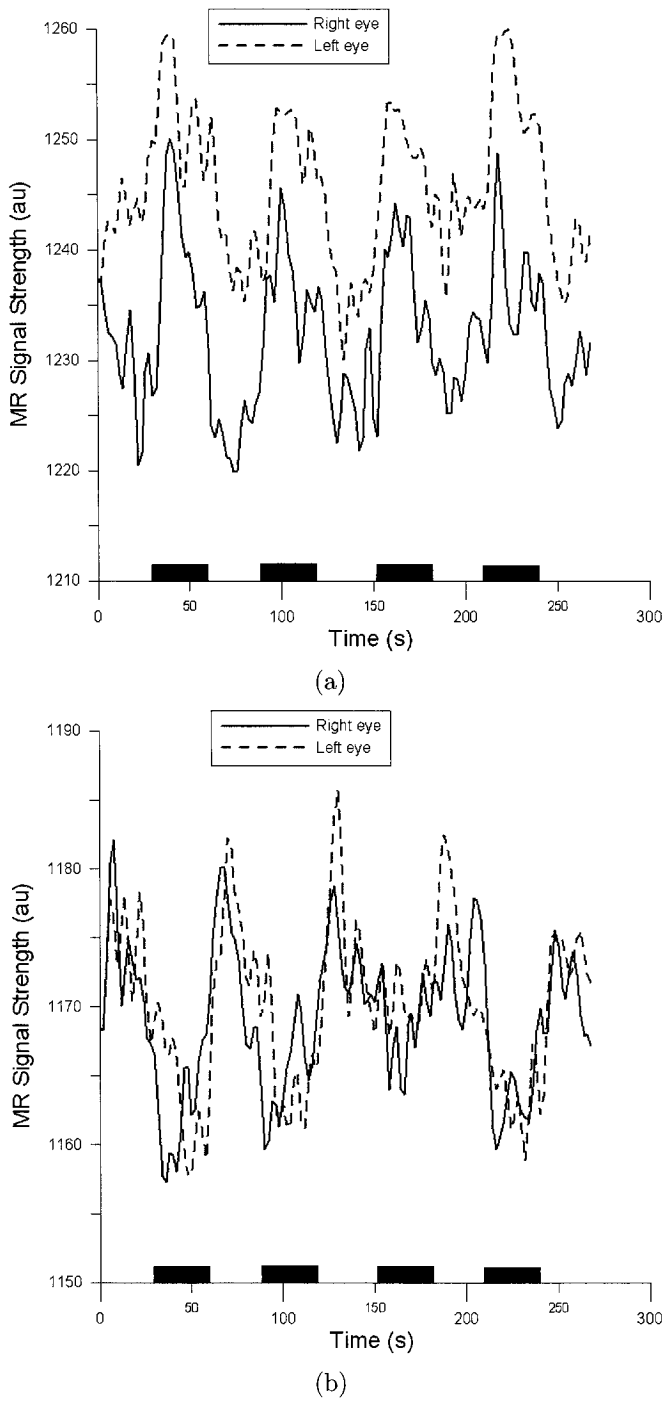

Figure 6.12: FMRI signal from Patient-I averaged over all significant voxels ($p \leq 0.001$) with (a) positive correlation and (b) negative correlation. Dark lines represent right eye stimulation, lighter dashed lines represent left eye stimulation. Black bars at the bottom indicate periods of visual stimulation.

right eye. The % signal change of the **+BOLD** signal was also significantly greater in the left eye compared to the right. A summary of these findings is given in Table 6.4.

	Left eye	**Right eye**
Avg. N75 latency (ms)	70.8*	73.9
Avg. N75 amplitude (μV)	-3.2*	-8.5
Avg. P100 latency (ms)	102.8	104.5
Avg. P100 amplitude(μV)	70	70
No. of **+BOLD** voxels	128	63
No. of **-BOLD** voxels	46	66
Avg. **+BOLD** CC	0.34*	0.29
Avg. **-BOLD** CC	-0.32	-0.31
Avg. **+BOLD** signal change (%)	1.62*	0.59
Avg. **-BOLD** signal change (%)	-0.64	-0.61

Table 6.4: Summary of VEP and FMRI findings for Patient-I. The * indicates a significant statistical difference ($p \leq 0.001$). No symbol indicates no statistical difference.

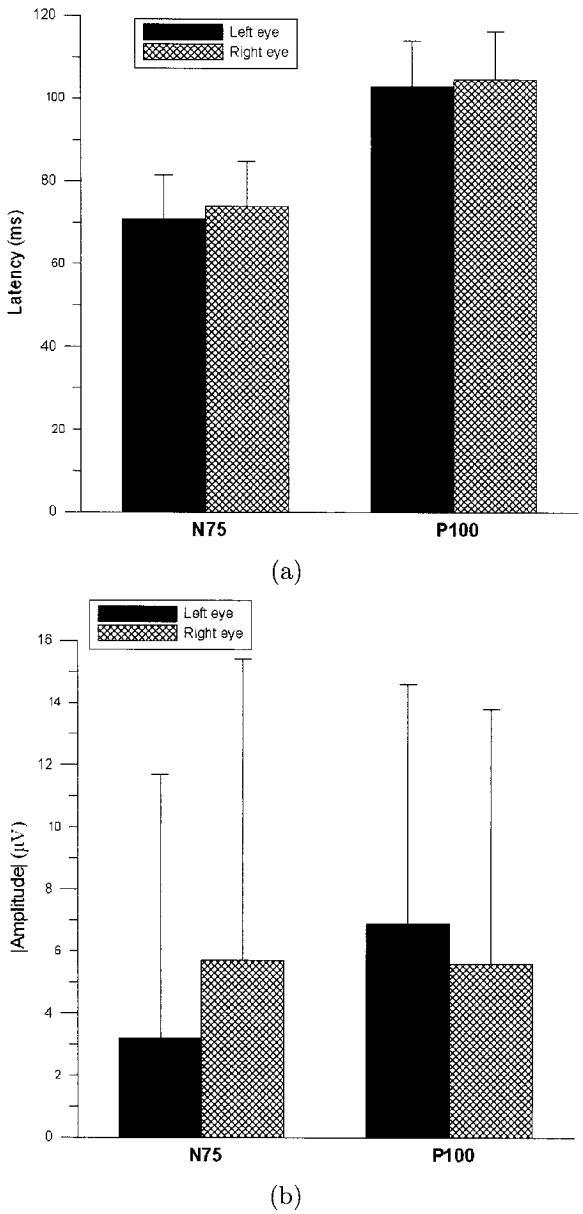

Figure 6.13: (a) The latency of the N75 and P100 components of Patient-I are shown during right and left eye stimulation. (b) The amplitude of the N75 and P100 components during right and left eye stimulation. The error bars represent the standard deviation.

6.4.10 Subject-PII

Patient-II was a 66 year old male. His vision was relatively normal in the right eye, while the left showed significant visual field loss.

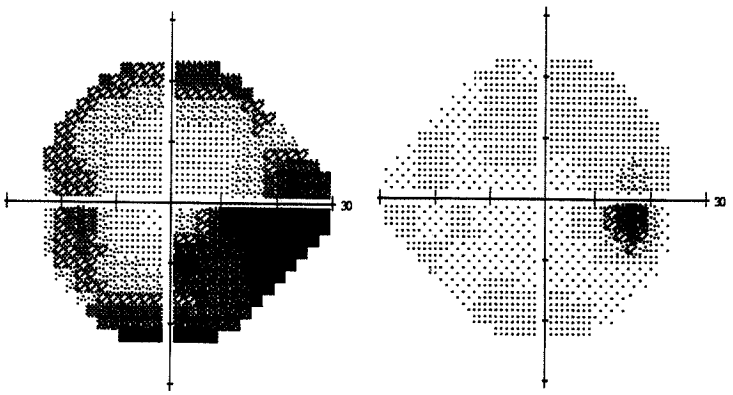

(a) Left eye (b) Right eye

Figure 6.14: Left and right eye perimetry maps obtained from Patient-II (Humphrey 24-2).

6.4.11 Results

The measured VEP of Patient-II is shown in figure 6.15. In this patient, the mean amplitude of the VEP signal in 60-80ms time range was statistically identical to that of the mean baseline. Therefore, there is no statistical evidence of the N75 component. FMRI maps are shown in figure 6.16. The positive and negative FMRI signals averaged over all voxels surviving the threshold are shown in 6.17

6.4.12 Discussion

The VEP measurements from this patient were of particular interest as there was no statistical evidence of an N75 component, though a relatively strong P100 component was present. Based on findings described earlier in the thesis, this would suggest a smaller **+BOLD** response compared to the **-BOLD** response. This was in fact observed, with the negative response containing more active voxels that were more highly correlated than the positive. Moreover, this negative response was greater in the healthy right eye compared to the damaged left eye. The P100 was significantly

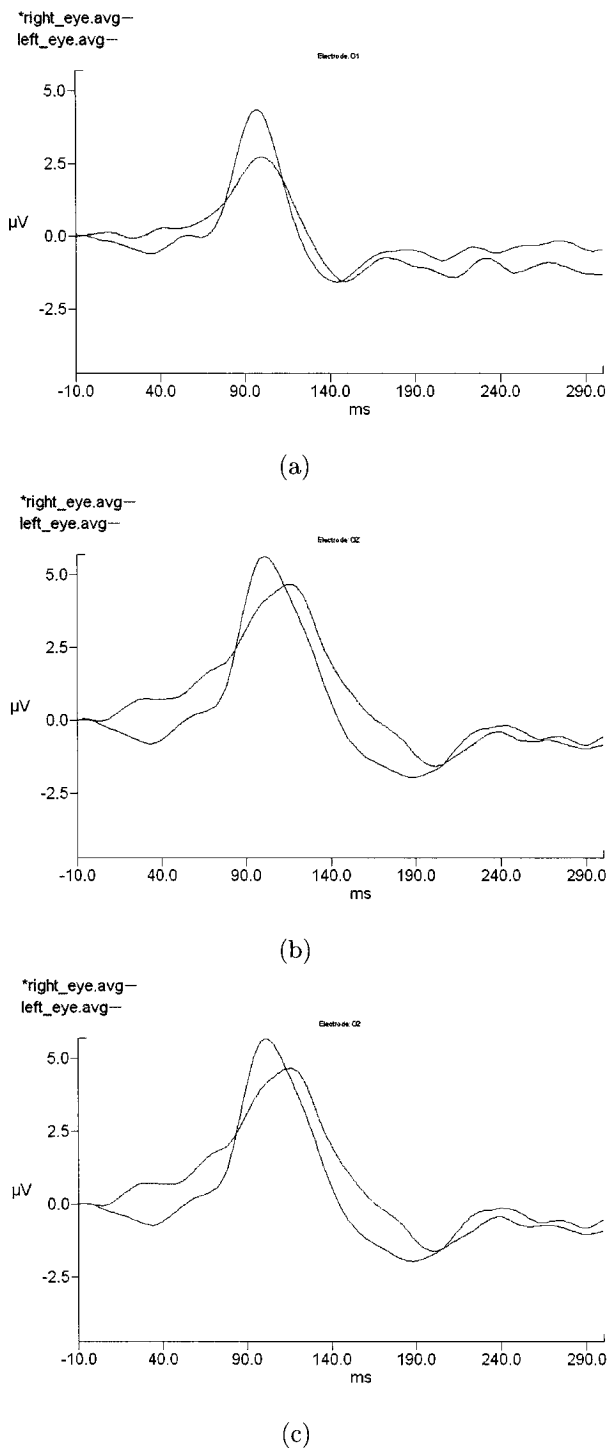

Figure 6.15: VEPs from Patient-II as measured at electrode sites (a) O1, (b) Oz and (c) O2. Black traces are from right eye stimulation, red traces from left eye stimulation.

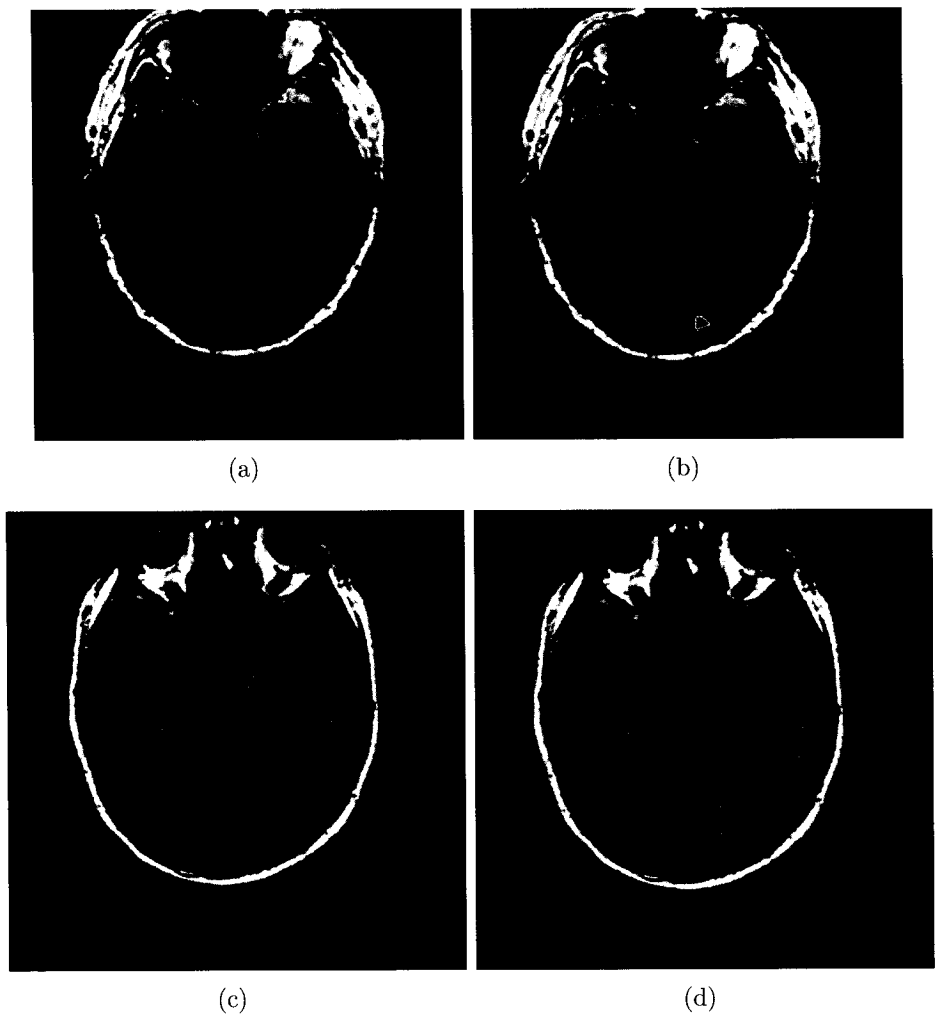

Figure 6.16: FMRI activation maps from Patient-II showing the dominant **+BOLD** response from the (a) left and (b) right eyes, as well as the dominant **-BOLD** response from the (c) left and (d) right eyes. Visual stimulation was presented in the left hemifield only, resulting in peak activation in the right hemisphere. Maps are thresholded to $p \leq 0.001$.

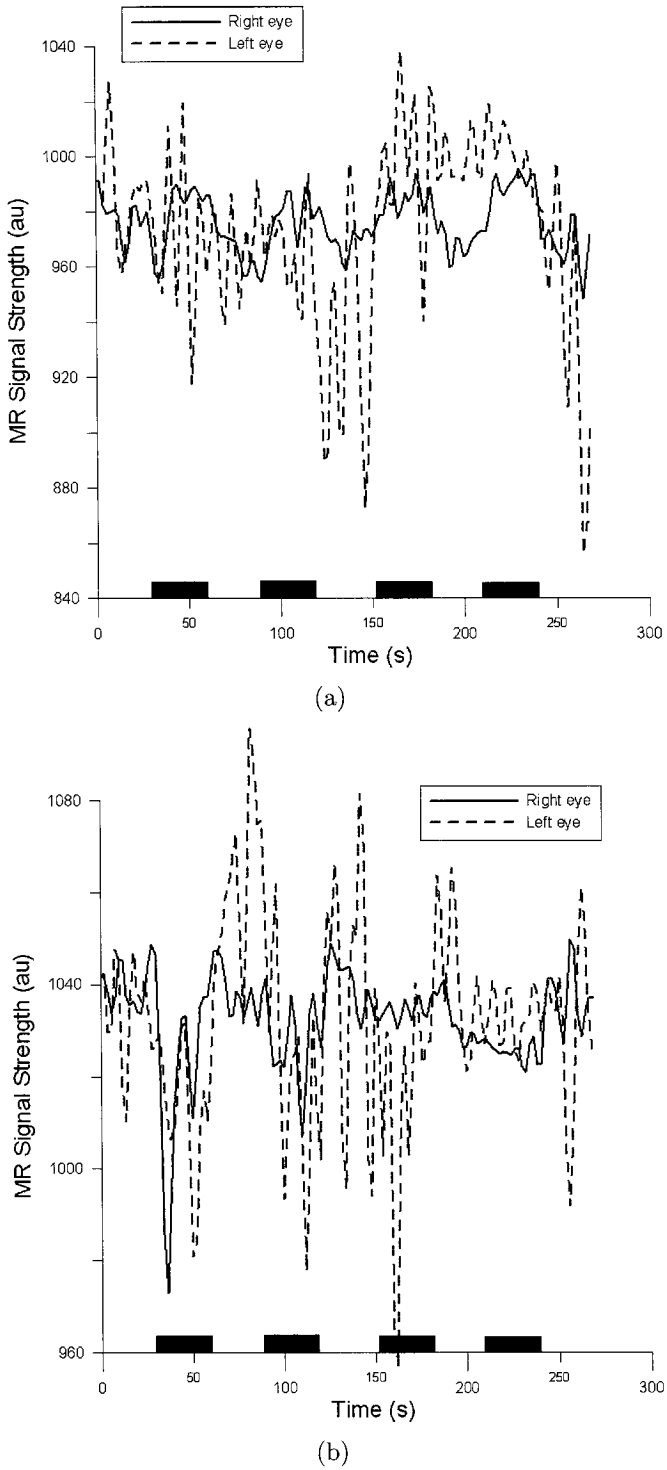

Figure 6.17: FMRI signal from Patient-II averaged over all significant voxels ($p \leq 0.001$) with (a) positive correlation and (b) negative correlation. Dark lines represent right eye stimulation, lighter dashed lines represent left eye stimulation. Black bars at the bottom indicate periods of visual stimulation.

delayed in the left eye compared to the right (figure 6.18). No significant difference in P100 amplitude was found. A summary of these these detailed findings are summarized in Table 6.5.

	Left eye	**Right eye**
Avg. N75 latency (ms)	N/A	N/A
Avg. N75 amplitude (μV)	N/A	N/A
Avg. P100 latency (ms)	104.8	102.4*
Avg. P100 amplitude(μV)	8.2	8.9
No. of **+BOLD** voxels	2	40
No. of **-BOLD** voxels	22	112
Avg. **+BOLD** CC	0.23	0.27*
Avg. **-BOLD** CC	-0.24	-0.29
Avg. **+BOLD** signal change (%)	0.34	0.44
Avg. **-BOLD** signal change (%)	-1.64	-1.32

Table 6.5: Summary of VEP and FMRI findings for Patient-II. The * indicates a significant statistical difference ($p \leq 0.005$). No symbol indicates no statistical difference.

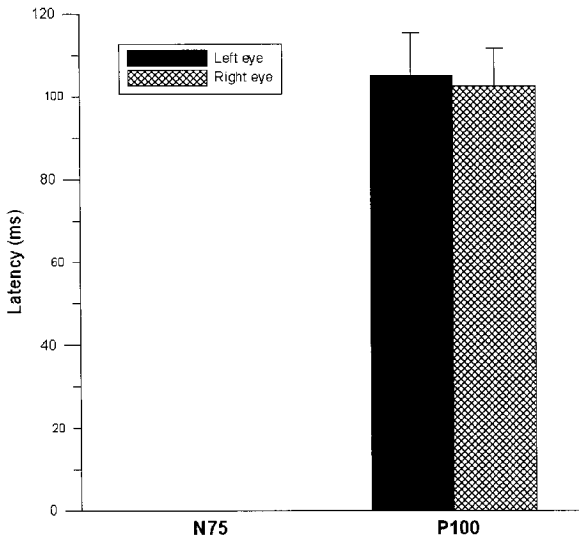

(a)

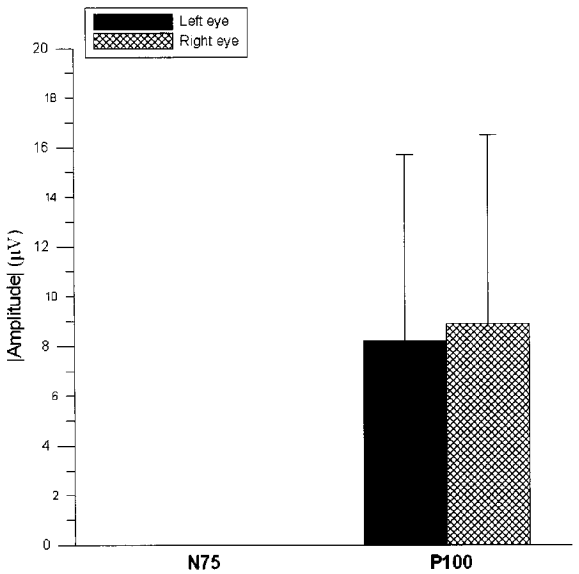

(b)

Figure 6.18: (a) The latency of the P100 component of Patient-II is shown during right and left eye stimulation. (b) The amplitude of the P100 component during right and left eye stimulation. The N75 was not observed in this patient. The error bars represent the standard deviation.

6.4.13 Subject-PIII

Patient-III was a 69 year old male. His right eye had relatively little visual field loss, while the left showed significant visual field defects in the macular-nasal and inferior paramacular temporal area (see figure 6.19).

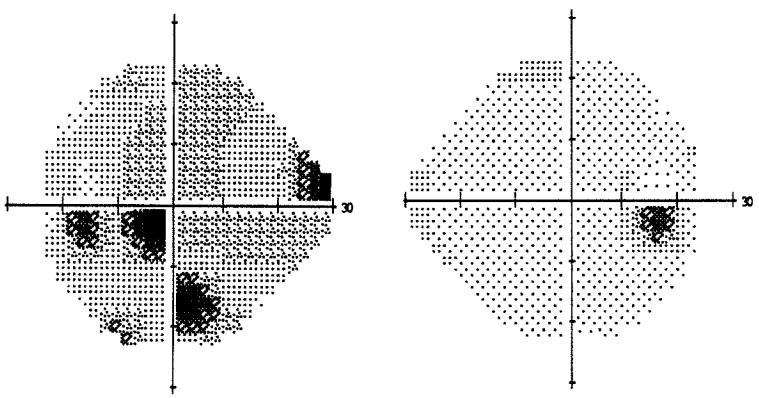

(a) Left eye (b) Right eye

Figure 6.19: Patient-III right and left eye perimetry maps (Humphrey 24-2).

6.4.14 Results

The measured VEP of patient is shown in figure 6.20. FMRI maps are shown in figure 6.21. The positive and negative FMRI signals averaged over all voxels surviving the threshold are shown in 6.22

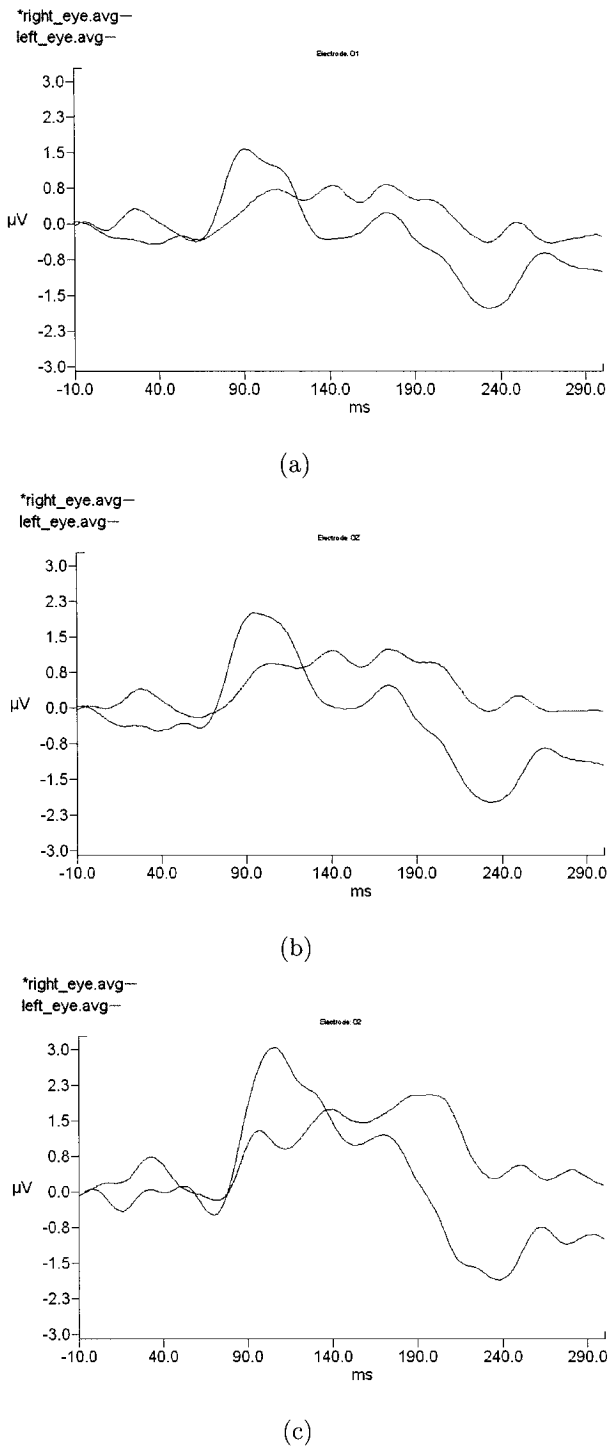

Figure 6.20: VEPs from Patient-III as measured at electrode sites (a) O1, (b) Oz and (c) O2. Black traces are from right eye stimulation, red traces from left eye stimulation.

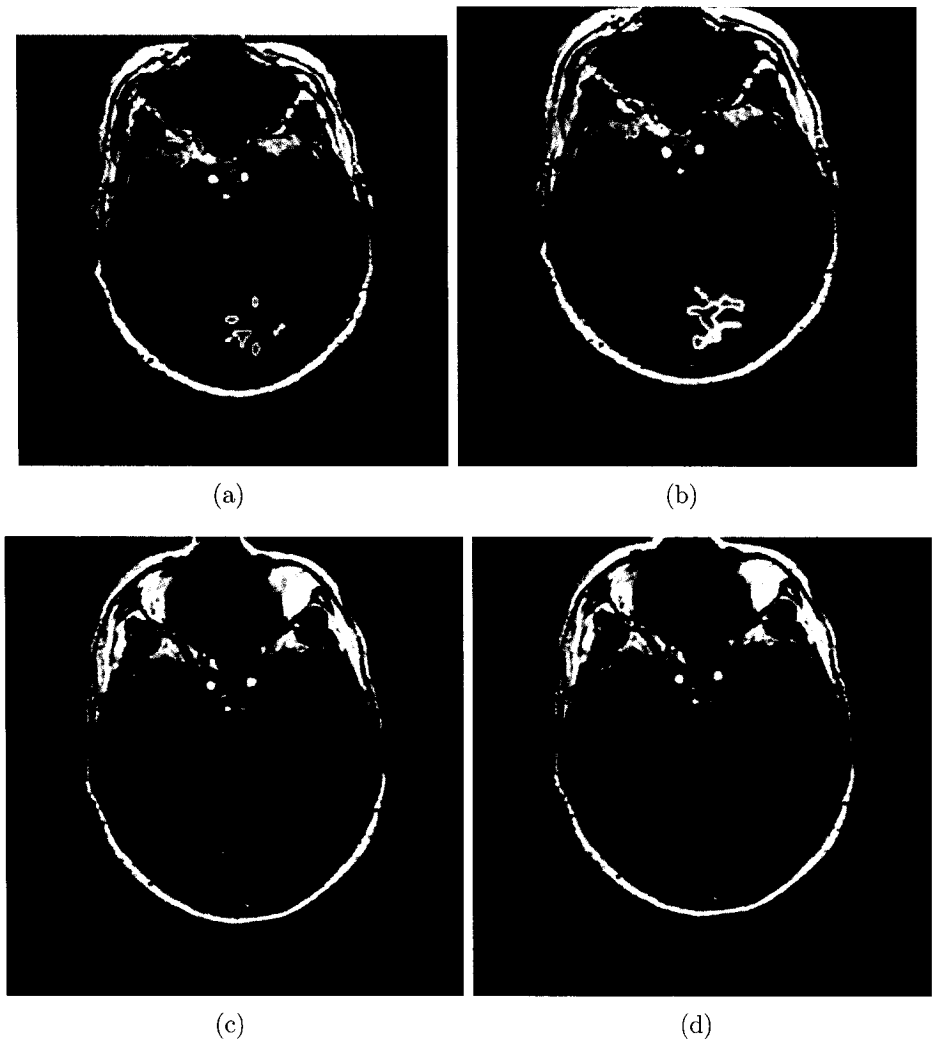

Figure 6.21: FMRI activation maps from Patient-III showing the dominant **+BOLD** response from the (a) left and (b) right eyes, as well as the dominant **-BOLD** response from the (c) left and (d) right eyes. Visual stimulation was presented in the left hemifield only, resulting in peak activation in the right hemisphere. Maps are thresholded to $p \leq 0.001$.

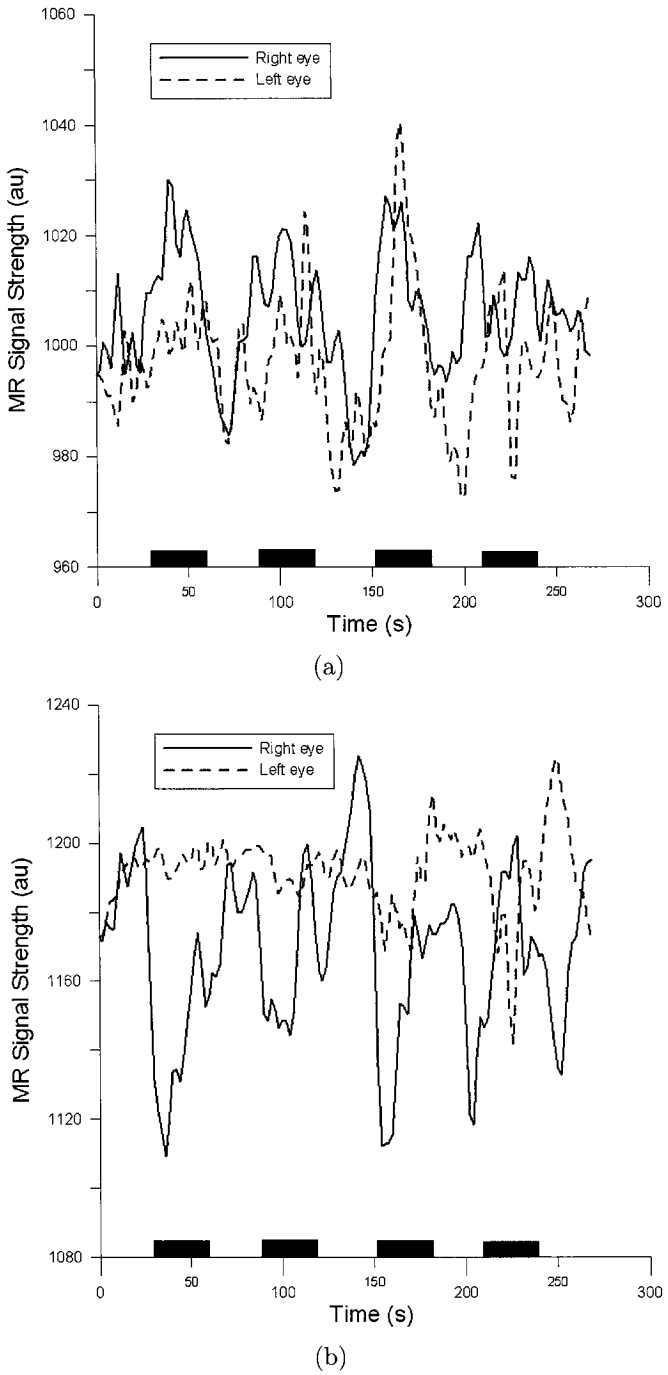

Figure 6.22: FMRI signal from Patient-III averaged over all significant voxels ($p \leq 0.001$) with (a) positive correlation and (b) negative correlation. Dark lines represent right eye stimulation, lighter dashed lines represent left eye stimulation. Black bars at the bottom indicate periods of visual stimulation.

6.4.15 Discussion

The VEP and FMRI results showed reduced measured activity in the damaged eye compared to the healthy eye. The N75 was significantly delayed in the left eye while the P100 latency was unaffected (figure 6.23). The **+BOLD** response was clearly dominant in the right eye, showing more highly correlated voxels with a significantly higher % signal change relative to the left. A summary of these results are shown in Table 6.6.

	Left eye	**Right eye**
Avg. N75 latency (ms)	73.1*	69.4
Avg. N75 amplitude (μV)	-3.5	-2.8
Avg. P100 latency (ms)	104.0	102.3
Avg. P100 amplitude(μV)	4.4	5.3
No. of **+BOLD** voxels	34	79
No. of **-BOLD** voxels	21	37
Avg. **+BOLD** *CC*	0.27*	0.29
Avg. **-BOLD** *CC*	-0.25	-0.27
Avg. **+BOLD** signal change (%)	0.94*	1.10
Avg. **-BOLD** signal change (%)	-0.70*	-2.65

Table 6.6: Summary of VEP and FMRI findings for Patient-III. The * indicates a significant statistical difference ($p \leq 0.05$). No symbol indicates no statistical difference.

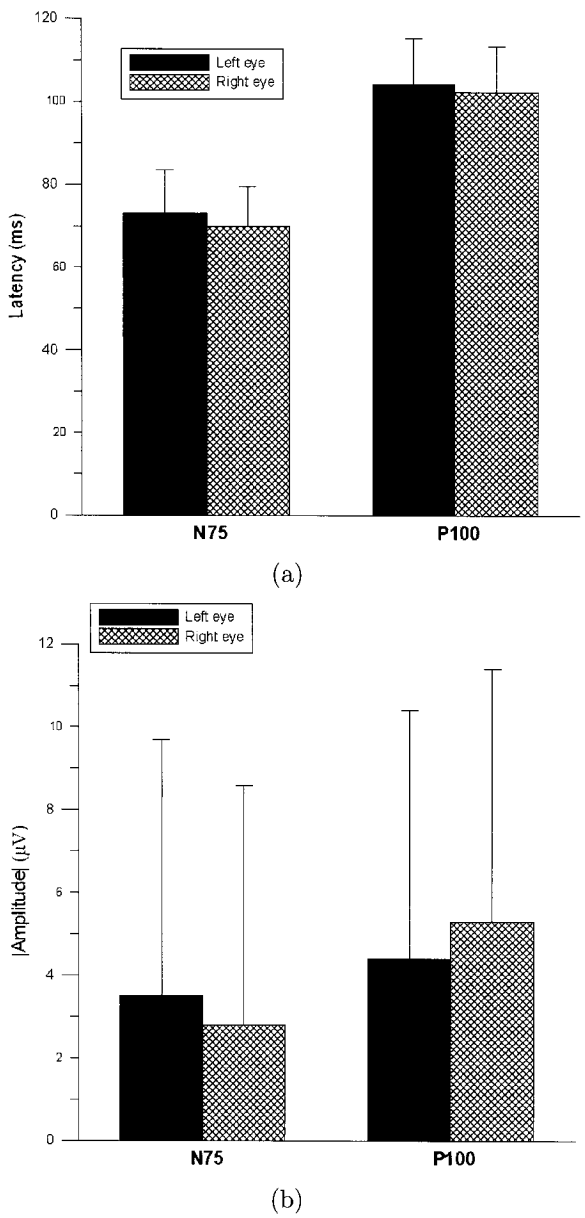

Figure 6.23: (a) The latency of the N75 and P100 components of Patient-III are shown during right and left eye stimulation. (b) The amplitude of the N75 and P100 components during right and left eye stimulation.

6.4.16 Subject-PIV

Patient-IV was a 62 year old female. Her right eye showed little visual field loss while the left showed significant visual field degradation in the paramacular area, while the central macula contained less damage (see figure 6.24).

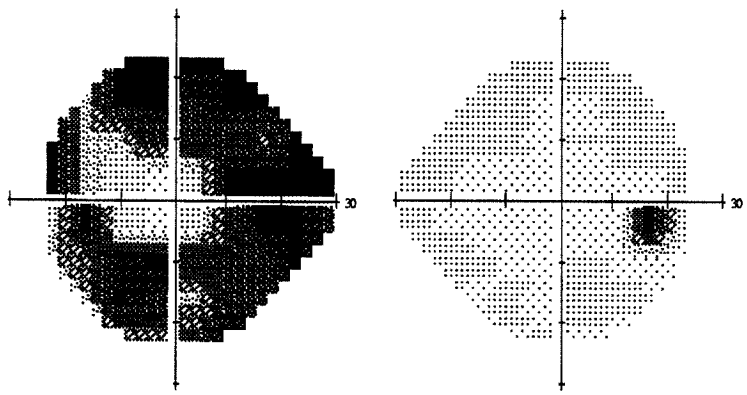

(a) Left eye (b) Right eye

Figure 6.24: Patient-IV left and right perimetry maps (Humphrey 24-2).

6.4.17 Results

The measured VEP of patient is shown in figure 6.25. FMRI maps are shown in figure 6.26. The positive and negative FMRI signals averaged over all voxels surviving the threshold are shown in figure 6.27

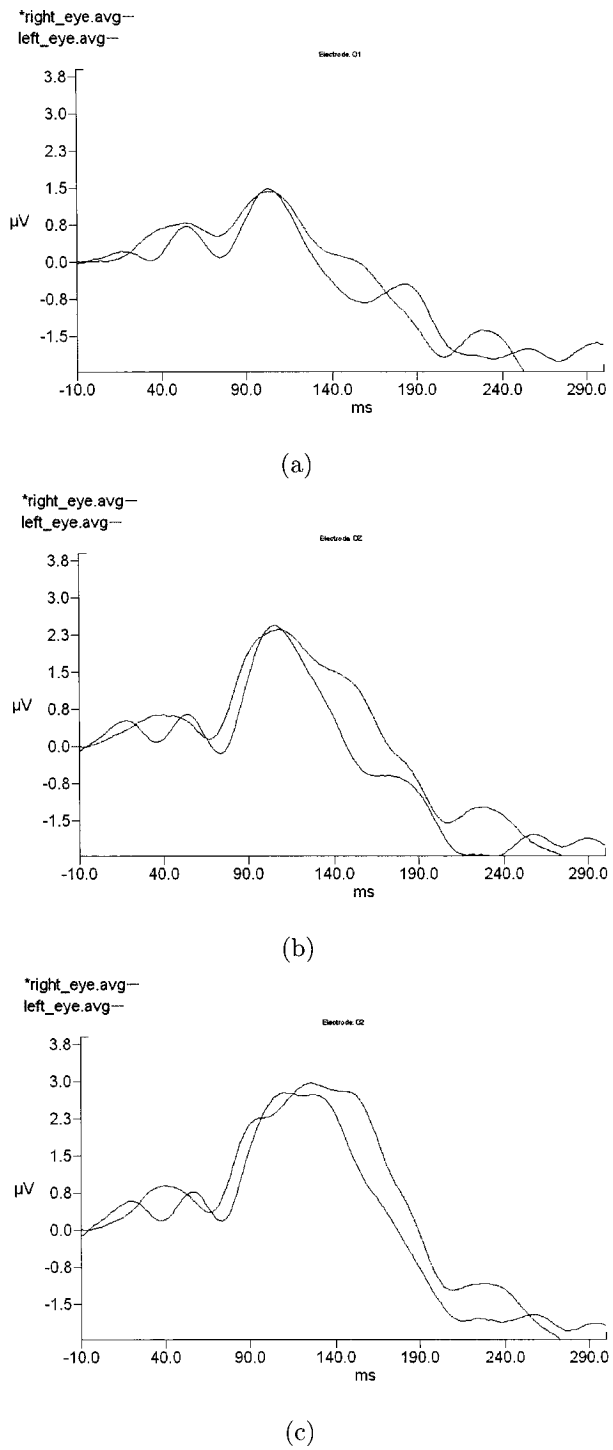

Figure 6.25: VEPs from Patient-IV as measured at electrode sites (a) O1, (b) Oz and (c) O2. Black traces are from right eye stimulation, red traces from left eye stimulation.

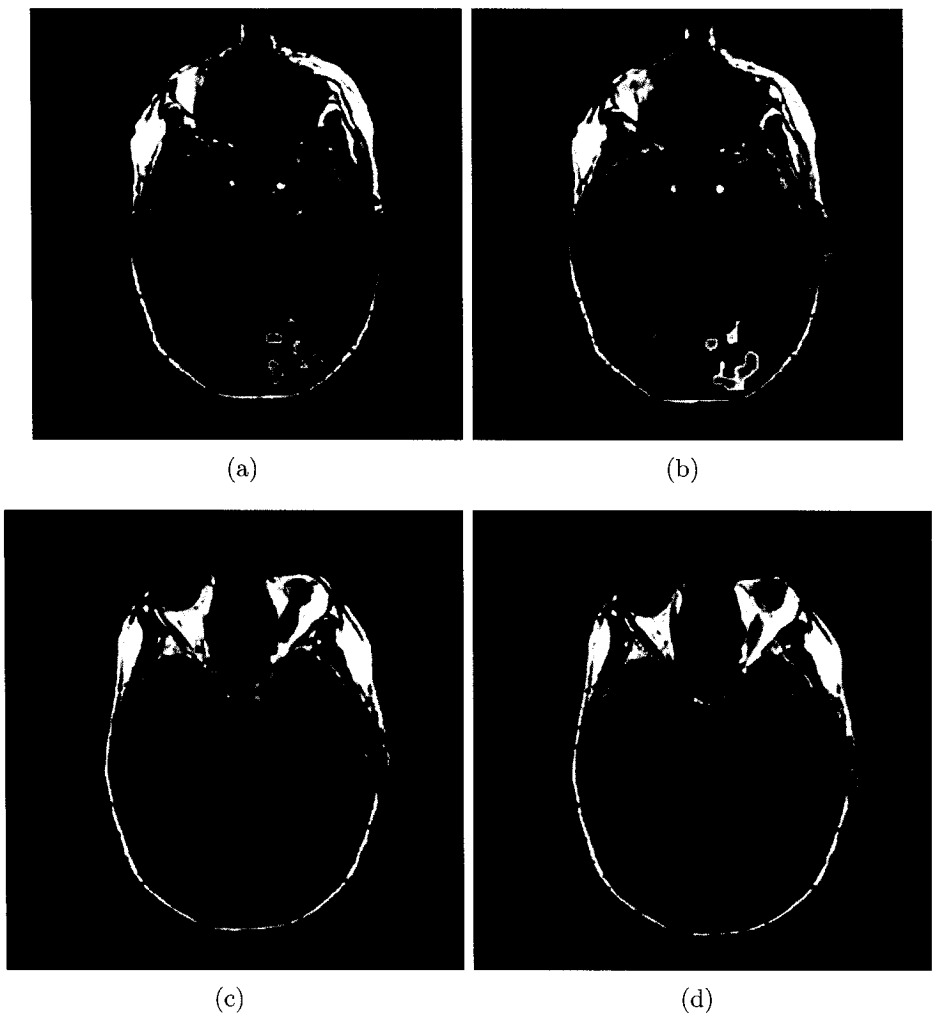

Figure 6.26: FMRI activation maps from Patient-IV showing the dominant **+BOLD** response from the (a) left and (b) right eyes, as well as the dominant **-BOLD** response from the (c) left and (d) right eyes. Visual stimulation was presented in the left hemifield only, resulting in peak activation in the right hemisphere. Maps are thresholded to $p \leq 0.001$.

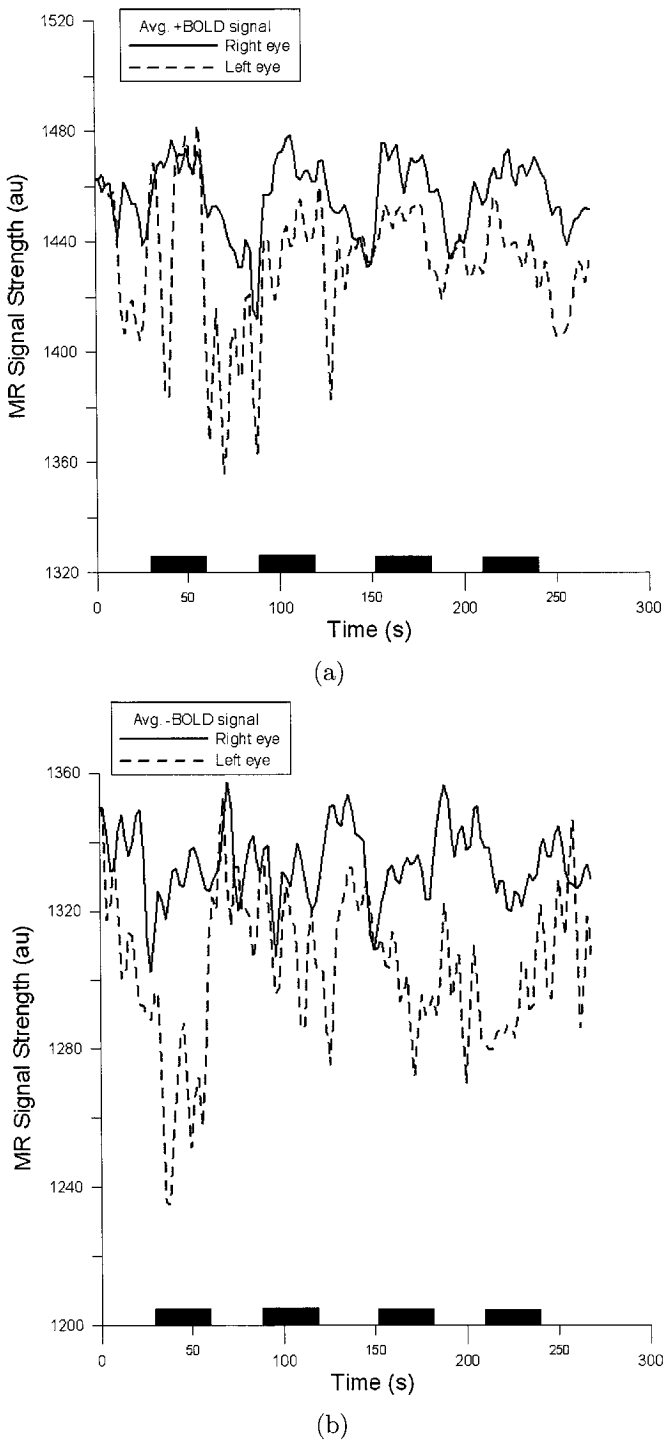

Figure 6.27: FMRI signal from Patient-IV averaged over all significant voxels ($p \leq 0.001$) with (a) positive correlation and (b) negative correlation. Dark lines represent right eye stimulation, lighter dashed lines represent left eye stimulation. Black bars at the bottom indicate periods of visual stimulation.

6.4.18 Discussion

The VEP and FMRI results diverge on this particular patient. The measured VEP showed no significant changes in latency of the N75/P100 in either eye. Their amplitudes were also statistically identical, suggesting that both eyes responded in the same fashion (figure 6.28). The FMRI results on the other hand were consistent with the previous patients findings. The **+BOLD** response was clearly stronger and highly correlated in the healthy eye compared to the damaged eye. These results are shown in Table 6.7.

	Left eye	**Right eye**
Avg. N75 latency (ms)	71.7	72.1
Avg. N75 amplitude (μV)	-2.4	-2.6
Avg. P100 latency (ms)	102.7	104.4
Avg. P100 amplitude(μV)	6.3	5.9
No. of **+BOLD** voxels	86	117
No. of **-BOLD** voxels	4	13
Avg. **+BOLD** *CC*	0.26*	0.31
Avg. **-BOLD** *CC*	-0.25	-0.27
Avg. **+BOLD** signal change (%)	0.60*	0.81
Avg. **-BOLD** signal change (%)	-1.74*	-0.73

Table 6.7: Summary of VEP and FMRI findings for Patient-IV. The * indicates a significant statistical difference ($p \leq 0.001$). No symbol indicates no statistical difference.

6.5 VEP dipole analysis

The mean dipole localization from the healthy subject's VEP is shown in figure 6.29. Localization of the N75 was not performed on one of the normal subjects since they did not show an N75 in the measured VEP. The localization of the N75 component in the remaining normal subject yielded solutions that explained less the 50% of the measured data (compared to an average >90% obtained in the previous experiments). The P100 performed slightly better, with a mean explained variance of 75% in both healthy subjects. Dipole localization of the N75 in all glaucoma patients once again yeilded solutions that exlpained less than 50% of the measured data. Localization of the P100 yeilded solutions with an average explained variance of 78% in three of the

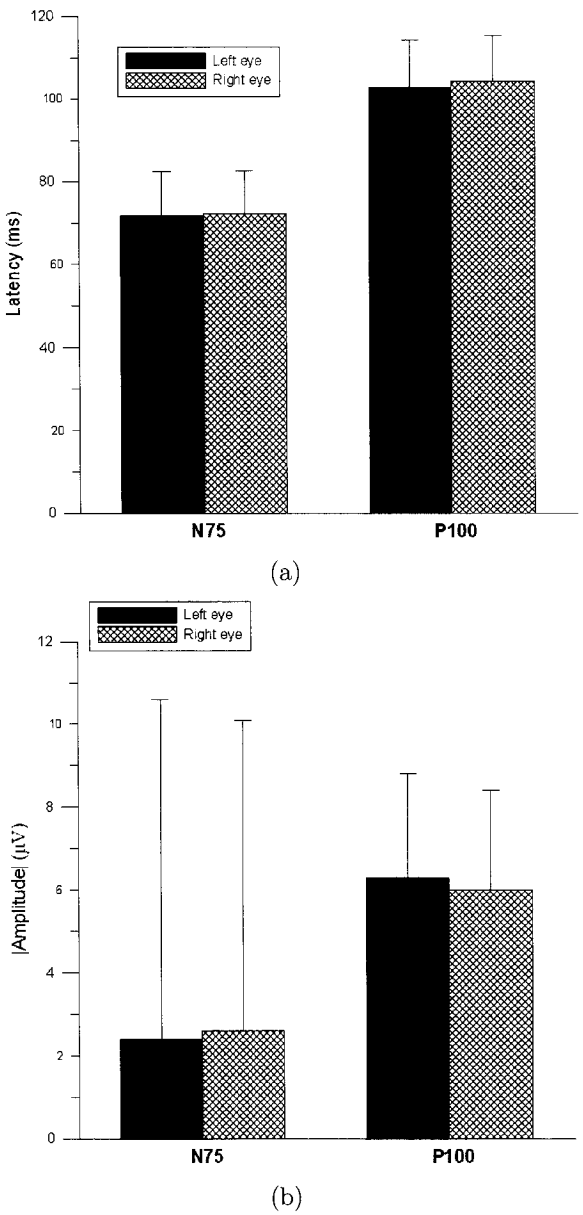

Figure 6.28: (a) The latency of the N75 and P100 components of Patient-IV are shown during right and left eye stimulation. (b) The amplitude of the N75 and P100 components during right and left eye stimulation. The dark error bars represent the standard deviation.

patients (localization of the P100 in the remainng patient also yeilded a solution with an explained variance of 32%). These results are shown in figure 6.30.

6.6 Discussion and summary

6.6.1 VEP & FMRI Group analysis

The results from the *ANOVA* test of the two healthy subjects demonstrate the symmetry between left and right eye that is to be expected in monocular VEP and FMRI experiments. In both subjects, the latency and amplitude of the N75 & P100 components were statistically identical in both eyes ($p \leq 0.05$). This is consistent with previous findings [140]. The FMRI results corroborate the VEP findings. There was no significant difference in the average *CC* and % signal change in the **+BOLD** response during stimulation of either eye. These results are summarized in table 6.8

	N75 (ms)	**P100 (ms)**	**+BOLD** (*CC*)	**-BOLD**(*CC*)
Left eye	70.6±10.6	98.4±12.4	0.29±0.07	-0.27±0.05
Right eye	70.4±10.08	98.2±12.3	0.30±0.08	-0.28±0.04

Table 6.8: Group average values of N75 & P100 latency and **+BOLD** & **BOLD** correlation-coefficient (*CC*) in healthy subjects. The results from the *ANOVA* test showed no significant difference in VEP latency and FMRI *CC* between eyes.

It should be noted that subject-I showed a higher number of activated voxels in the right eye compared to the left. Toosy et al. [149] showed that lateralization of FMRI activation is to be expected from monocular stimulation in healthy subjects. The study by Toosy et al. limited the analysis to the *volume* of FMRI activation, and not the distribution of mean *CC* and % signal change as we did. It is therefore suggested while the volume of activation may differ in monocular stimulation experiments, the mean *CC* and % signal change are similar in both hemispheres of subjects with normal vision.

The results from the glaucoma patients demonstrate what differences are to be expected in monocular VEP and FMRI recordings. The group average VEP over the healthy and damaged eyes of all patients is shown in figure 6.31. The group mean latency of the N75 component when the healthy eye was stimulated was 70.0 ± 9.9ms and 72.1 ± 10.8ms when the damaged eye was stimulated. The group mean latency

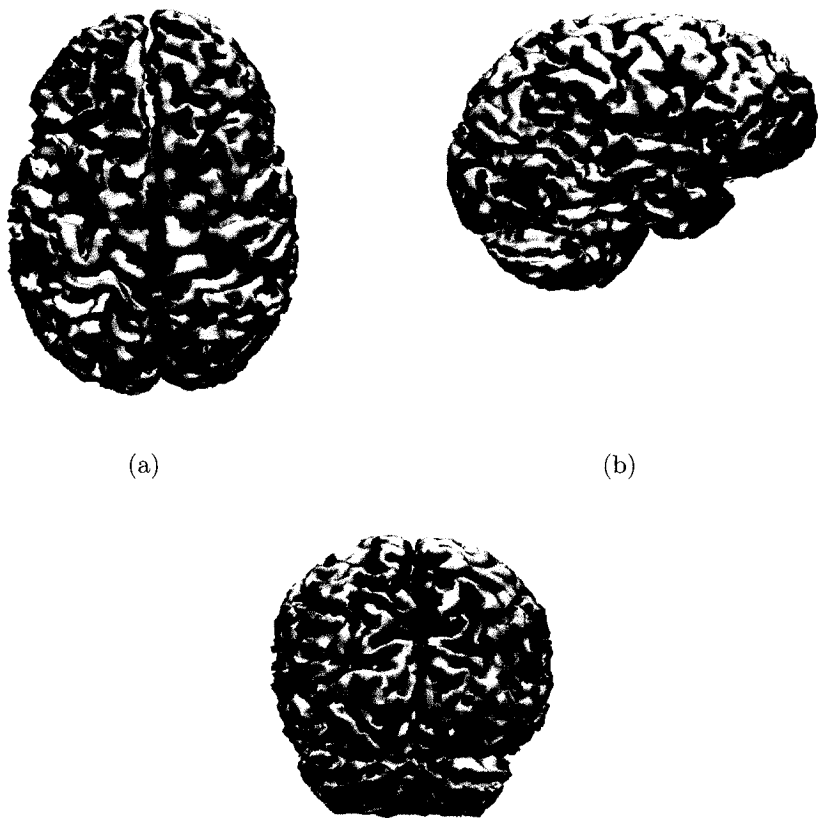

(a) (b)

(c)

Figure 6.29: Dipole localization of the P100 component in healthy participants from monocular stimulation in the left (red cube) and right (green cube) eye. Localization of the N75 component is not shown due to its very low explained variance (see text for details). Axial (a), sagittal (b) and coronal (c) views from a reconstructed cortical surface are shown.

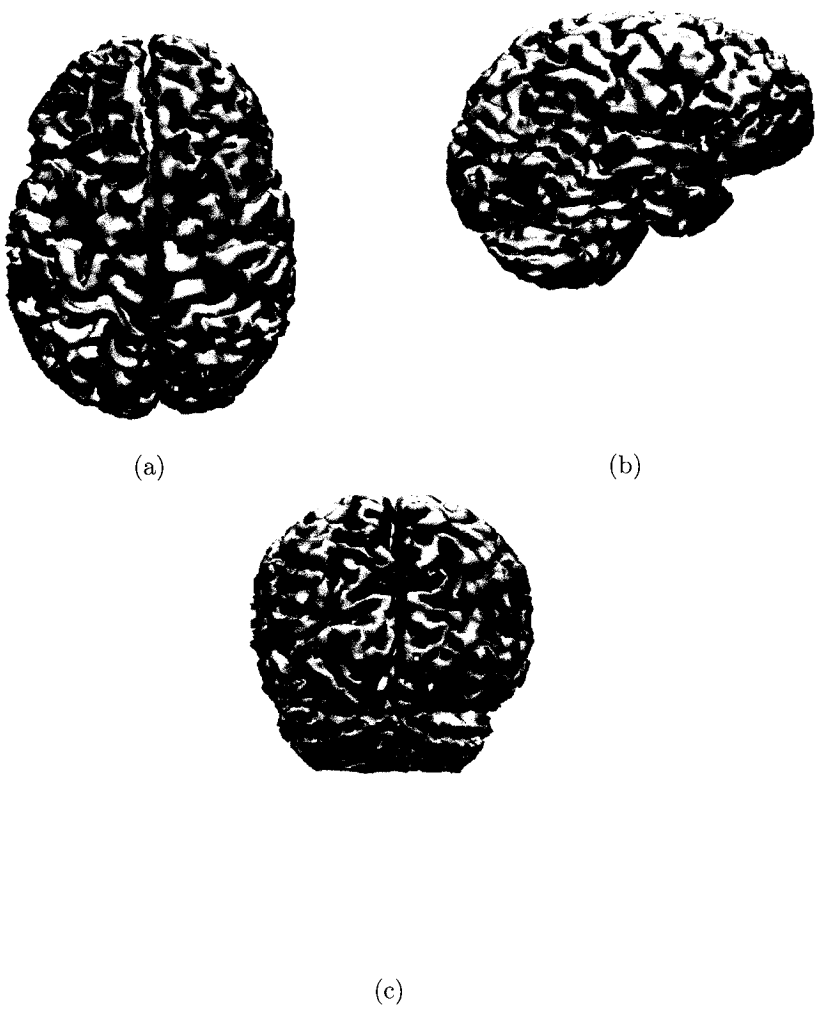

Figure 6.30: Dipole localization of the P100 component in healthy participants from monocular stimulation in the healthy (purple cube) and damaged (yellow cube) eye. Localization of the N75 component is not shown due to its very low explained variance (see text for details). Axial (a), sagittal (b) and coronal (c) views from a reconstructed cortical surface are shown.

of the P100 component when the healthy eye was stimulated was 102.0 ± 10.4ms and 104.1 ± 11.1ms when the damaged eye was stimulated. The results from the $ANOVA$ test show that the N75 component in the damaged eye condition was significantly delayed relative to the healthy eye condition ($p \leq 0.001$). The latency of the P100 on the other hand was statistically identical in both healthy and damaged eyes.

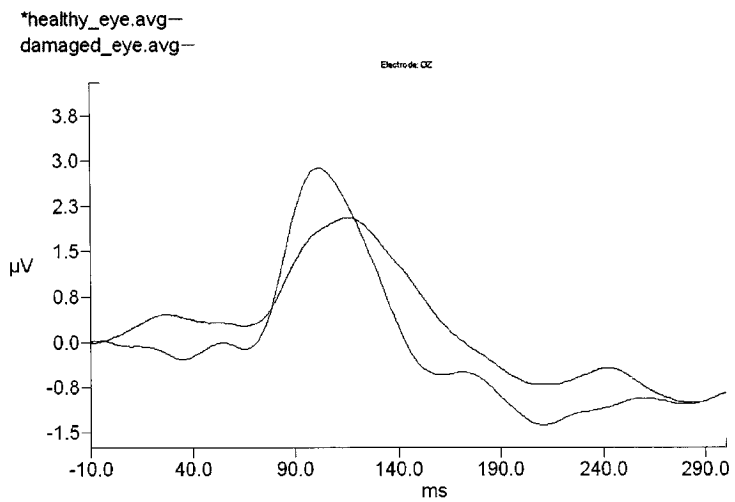

Figure 6.31: Group average of VEP as measured at electrode site Oz. The black trace represents the average over the healthy eyes and the delayed red trace represents the average over the damaged eyes of the patients.

For the FMRI, the group average **+BOLD** CC was 0.33 ± 0.09 when the healthy eye was stimulated and 0.28 ± 0.06 when the damaged eye was stimulated. The group average **-BOLD** CC was -0.29 ± 0.08 when the healthy eye was stimulated and -0.28 ± 0.08 when the damaged eye was simulated. The results from the $ANOVA$ test show that the **+BOLD** CC in the healthy eye condition was significantly greater than the **+BOLD** CC in the damaged eye condition ($p \leq 10^{-6}$). The **-BOLD** CC on the other hand was statistically identical in both healthy and damaged eyes. The group average **+BOLD** signal in healthy and damaged eye conditions is shown in figure 6.32. Taken together, the VEP and FMRI results show that the N75 VEP component and the **+BOLD** FMRI response are better markers (relative to the P100 VEP component and the **-BOLD** FMRI response) for correctly identifying glaucomatous eyes. These results are summarized in table 6.9

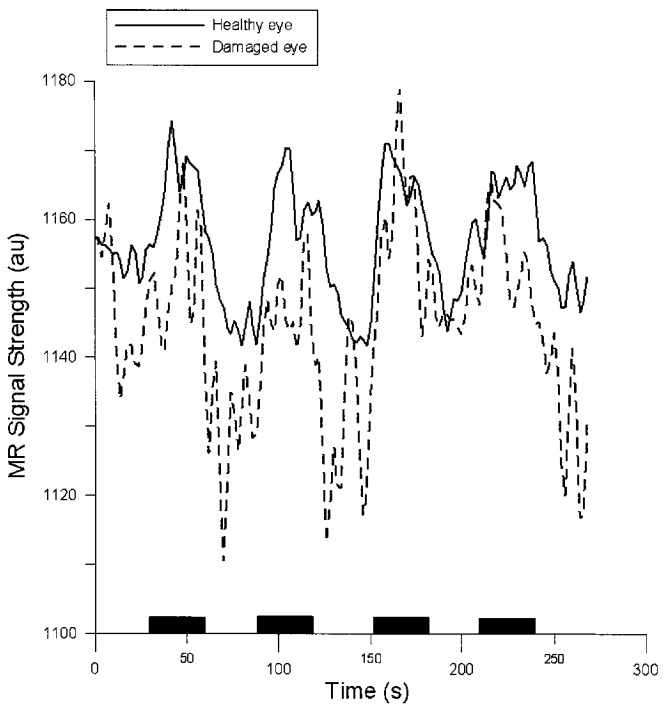

Figure 6.32: Group average of **+BOLD** signal in healthy and damaged eye stimulus conditions. The % signal change was significantly greater in the healthy eye condition compared to the damaged eye condition (see text for details).

	N75 (ms)	**P100 (ms)**	**+BOLD** (CC)	**-BOLD**(CC)
Healthy eyes	70.0 ± 9.9	102.0 ± 10.4	0.33 ± 0.09	-0.29 ± 0.08
Damaged eyes	$72.1 \pm 10.8^*$	104.1 ± 11.1	$0.28 \pm 0.06^*$	-0.28 ± 0.08

Table 6.9: Group average values of N75 & P100 latency and **+BOLD** & **BOLD** correlation-coefficient (CC) in four glaucoma patients. The $ANOVA$ test revealed a significant difference ($p \leq 0.01$) in the N75 latency and **+BOLD** CC between healthy and damaged eyes (denoted by *).

6.6.2 Dipole localization

Overall, the dipole localization results of the N75 in the normal and glaucoma patients were not conclusive. The P100 dipole solutions were localized near the posterior portion of the visual cortex in both healthy and glaucoma populations. Due to the small population size, statistical testing of the P100 dipole position in the two conditions (left vs. right in healthy population)and (healthy eye vs. damaged eye in glaucoma population)was not carried out. To date, there is no supporting literature corroborating these results, and thus no significant conclusion can be drawn from the *location* of the dipole solutions.

6.6.3 Subject-specific analysis

In two patients, it was the N75 component that was significantly delayed, not the P100. In one of the remaining two patients, it was the P100 component that was delayed in the damaged eye, though it should be noted that this patient's N75 was absent. The remaining patient showed no significant changes in N75 or P100 latency between healthy and damaged eye. It has been shown in earlier studies that in some instances VEP delays may not be observed in damaged eyes caused by glaucoma [150, 151]. As seen in this patient's perimetry map, the majority of field defects were in the peripheral field, outside of the checkerboard stimulus field. It may therefore be possible that the stimulus was not large enough to encompass the entire damaged area of the visual field. However, this scenario is unlikely since the same stimulus was used during FMRI recordings and the results clearly showed a measurable difference between healthy and damaged eyes. In the majority of patients , the amplitudes of the N75 and P100 components were statistically identical in both eyes, and thus could not be used as reliable markers for the identification of visual field defects.

In all patients, the FMRI measurements correctly differentiated the cortical response obtained from the healthy eye relative to the damaged eye. This was characterised by (1) a higher number of statistically significant voxels during stimulation of the healthy eye, (2) a higher mean CC of these voxels and (3) a greater average % signal change over these voxels. The **-BOLD** response on the other hand was more variable. In three of the four subjects, the **-BOLD** response showed more activated voxels when the healthy eye was stimulated, though the mean CC of these voxels was statistically identical to that of the voxels in the damaged eye.

Of particular interest was the VEP and FMRI results obtained in healthy Subject-NII and glaucoma Patient-II. In both of these cases, an absence of the N75 component was observed with a relatively robust P100 component. This has been observed in healthy subjects [25] as well as in patients with late-stage glaucoma [152]. This finding provides more evidence that the N75 and P100 are physiologically distinct- the existence of the P100 may not directly depend on the existence of the N75. Moreover, the FMRI findings from these participants showed a more dominant and statistically significant **-BOLD** response than the **+BOLD** response. This finding is consistent with previous findings in this work indicating that the N75 is better correlated with the **+BOLD** response, while the P100 is better correlated with the **-BOLD** response.

6.7 Summary and Conclusion

In both age-matched healthy subjects, the measured VEP and FMRI showed no significant difference between eyes. In the majority of patients, both VEP and FMRI responses clearly demonstrated a difference between healthy and damaged eyes. This difference was mainly characterized by (1) a delay of the N75 VEP component during stimulation of the damaged eye, (2) a decrease in the **+BOLD** % signal change and (3) a decrease in the number and average correlation coefficient of **+BOLD** voxels during stimulation of the damaged eye. A significant delay of the P100 and decrease of the **-BOLD** response was only observed in participants whose N75 was absent. Taken together, the VEP and FMRI results show that the N75 VEP component and the **+BOLD** FMRI response are better markers (relative to the P100 VEP component and the **-BOLD** FMRI response) for correctly identifying glaucomatous eyes. The

findings from this study are consistent with those of the previous chapters-the N75 appears to be better coupled to the **+BOLD** response, and the P100 appears to be better coupled to the **-BOLD** response. Due to the relatively small sample size, more measurements on uni-lateral glaucoma patients are needed in order to corroborate this suggestion.

Chapter 7

Future work

A limitation of this study is the omission of the third VEP component (N150). To our knowledge, the location of this component has not been investigated very well using VEP and studies using invasive measurements have yielded conflicting results [30, 153]. This lack of information would have made it difficult to validate the inverse solution, and was therefore omitted from the thesis. However, seeing as how this component is often seen in the VEP, it is important to study its relationship with FMRI. The first step would be to estimate the number of sources responsible for eliciting the N150. This could be achieved by comparing a single dipole solution of the N150 component with a distributed inverse solution model. From there, its location could be compared to the location of the N75/P100 and to the location of the peak **+BOLD** & **-BOLD** response. Since the N150 is a negative going component, it is hypothesized that it will be better correlated to a **+BOLD** response. It would also be advantageous to investigate how the N150 is modulated and if it is affected in glaucoma populations. Preliminary results show that the N150 is present in glaucoma populations though delayed relative to healthy people.

In experiment II, it was found that in over half of the subjects measured, the **-BOLD** response in the ipsilateral hemisphere seemed to vanish when the stimulus was in the subjects peripheral visual field. The contralateral response on the other hand remained relatively unchanged in both position and magnitude. If the suggestions put forth in this thesis are true, then it would follow that a strong ipsilateral negative FMRI response should be accompanied by a P100 source nearby. However, in experiment I it was shown that the P100 dipole always converged to a location in the contralateral visual cortex. It is therefore possible that there may be a second, though weaker, ipsilateral P100 source [154]. This was briefly investigated early on, though in most cases, a two dipole inverse solution simply resulted in overlapping sources in the contralateral hemisphere. Therefore, it may be necessary to perform a

one dipole inverse solution (which leads to a source in the contralateral hemisphere), and then perform a second dipole search while keeping the first dipole fixed. This is essentially the same as fitting a dipole to the residual potentials left unaccounted for by the first dipole.

The **-BOLD** FMRI response is relatively new to the neuroimaging community. This work, as well as others cited in the conclusion show that it does not behave in the same manner as the **+BOLD** response. It is therefore important to determine in what capacity the **-BOLD** response can be influenced. It has been suggested that attention plays a crucial role in eliciting the **-BOLD** response [155], which is encouraging since the P100 has also been shown to be modulated by attention [133]. This is consistent with the suggestions put forth in this thesis-that the P100 VEP component is better linked to the **-BOLD** response.

Lastly, it would be advantageous to pursue studying the effects of visual impairment on the VEP and FMRI response. As this was the first time that VEP and FMRI measurements were conducted on glaucoma patients, the primary goal was to investigate whether or not these modalities were sensitive enough to detect the effects of late-stage, unilateral glaucoma. This is a very specific form of glaucoma, and thus limited the number of patients (four in total) that could participate in the study. Out of this patient population, VEP measurements showed a significant effect in three of the patients, while FMRI showed a significant effect in all four. It would be advantageous to increase the patient population to determine if one modality is more sensitive to late-stage, unilateral glaucoma than the other.

Chapter 8

Summary and Conclusion

Since its development in the early 1990's, FMRI has become a widely used tool in the neuroimaging community. Recently, there has been a push toward implementing a combined EEG/FMRI protocol, in the hopes that more information may be made available by combining these two modalities. This has resulted in a surge of studies making use of sequential and/or simultaneous EEG/FMRI measurements. Studies using invasive recording techniques have demonstrated that the hemodynamic activity routinely seen in FMRI studies is due to synaptic neuronal activity and not spiking activity [83]. EEG measurements are also thought to be particularly sensitive to synaptic neuronal activity. This suggests that EEG and FMRI are sensitive to the same cortical events, though the exact relationship between their sources is still not fully understood. To further this understanding, the aim of this thesis is to study the level at which EEG and FMRI measurements complement one another.

In the first experiment of this thesis, we compared the location of VEP and FMRI sources in response to a basic visual stimulus. In the majority of subjects, it was found that the location of the N75 VEP component was closest to the peak **+BOLD** response. The location of the next VEP component, the P100, was closer to the peak **-BOLD** response. This indicates that the N75 may be better correlated to the **+BOLD** response, while the P100 is better correlated with the **-BOLD** response. However, this result alone does not resolve this particular aspect of the EEG/FMRI relationship. To further cloud the issue, there are known sources of error in a VEP inverse solution which could be as large as a few centimeters. We therefore designed a second experiment that would rely less on the exact *location* of the VEP/FMRI sources, and more on their change in location when the stimulus position is changed.

In this second experiment, we studied how the measured VEP and FMRI from healthy subjects responded to a change in stimulus position from central to peripheral visual field. In the majority of subjects, the location of the N75 moved according to

retinotopic mapping, while the location of the P100 remained relatively unchanged. The FMRI results show a similar effect with the **+BOLD** response moving in a retinotopic manner, while the **-BOLD** response remained in a fairly fixed location. On average, the location of the N75 and **+BOLD** moved 2.8 ± 0.8 times as much as the P100 and **-BOLD** did. The findings from this experiment corroborate the findings of the previous experiment that there is a possible linkage between the N75/**+BOLD** response and P100/**-BOLD** response.

In the third experiment, we sought to implement VEPs and FMRI in a clinical setting. The goal was to investigate whether or not VEPs and/or FMRI were able to accurately detect the effects of visual field defects in the brain caused by late-stage glaucoma. Overall, it was shown in uni-lateral glaucoma patients that both the VEP and FMRI can reliably detect the effects of visual impairment, though by different means. In the case of the VEP, it was the delay of the N75 component that was the most robust marker in identifying glaucomatous eyes. The FMRI results showed that it was the **+BOLD** response that was the robust marker for identifying glaucomatous eyes. These findings indicate that the N75 component of the VEP and the **+BOLD** response of FMRI are the more reliable form of measurements that can detect the effects of glaucoma in the visual cortex.

In the two cases (one healthy subject, one glaucoma patient) where the measured VEP showed no signs of an N75 component, the P100 was quite robust. The FMRI findings in these two cases were consistent with our hypothesis as it was shown that the **+BOLD** response was for the most part absent, while the **-BOLD** response appeared more dominant. In the patient who showed no signs of an N75, it was the P100 that was able to detect a measurable VEP delay in the damaged eye relative to the healthy one. In that same patient, it was the **-BOLD** response that accurately reflected the effects of the damaged eye relative to healthy one. The **+BOLD** response did not show a measurable difference. This suggests that the P100 and the **-BOLD** response are only capable of detecting the effects of visual impairment when the N75 and **+BOLD** response are absent. The overall findings from this experiment not only demonstrate that the VEP and FMRI modalities are sensitive to the effects of glaucoma in the visual cortex, but they also reinforce the suggestion that there exists a link between only certain constituents of the VEP and FMRI, namely between the

N75/+**BOLD** and the P100/-**BOLD**.

The pathway from eye to brain has been extensively studied in the past. Visual information first flows into layer 4 of the primary visual cortex, and then to layers 2/3. Intracortical recordings in monkeys have demonstrated that the N75 component reflects *excitatory* postsynaptic potentials of stellate cells in the primary visual cortex layer 4C [35]. The same authors postulate that the ensuing P100 component reflects *inhibitory* postsynaptic potentials of pyramidal neurons in layers 2 and 3 [35]. There are a growing number of studies that have suggested that the **+BOLD** response is driven by excitatory postsynaptic potentials [59, 60, 61]. The **-BOLD** response is thought to be mainly driven by neuronal inhibition [65, 66]. The overall results from this work are in agreement with this observation. It is therefore suggested that the FMRI signal may be initially triggered by the same sources that drive the EEG signal recorded at the scalp. However, this does not necessarily imply that the N75 and P100 (and the **+BOLD** and **-BOLD** response for that matter) are directly dependent on one another. The very fact that one of these two sources can exist without the other provides strong evidence that the two have distinct physiological structures, which is in agreement with previous studies [34, 60].

In conclusion, the results from this thesis indicate that there exists a strong relationship between the N75 VEP component and the **+BOLD** FMRI response and a strong relationship between the P100 VEP component and the **-BOLD** FMRI response. This relationship between neural and hemodynamic activity in the brain shows that both EEG and FMRI are capable of reflecting underlying neuronal activation, even though they are measuring different physiological events. This hypothesis has been explored here for the visual system, but should also be examined for different sensory systems in order to further evaluate the relationship between EEG and FMRI.

Appendix A

Validation of FMRI source localization-Case Study

A.1 Introduction

A 25-year-old male patient underwent several FMRI scans on the recommendation of Dr. David Clarke, Division of Neurosurgery, QEII Health Sciences Centre. MR imaging diagnosed a mass lesion in the vicinity of the motor cortex in the left hemisphere (figure A.1). FMRI measurements were made in order to investigate areas of functionality surrounding the abnormality. Locations of these particular centers based on FMRI findings were then verified via electrical stimulation of the cortex during neurosurgery.

A.2 Methods

FMRI measurements were made three days prior to surgery. In all cases, experiments were conducted using the block paradigm approach described in section 4.3.1. FMRI acquisition and off-line analysis were the same as described earlier in section 4.3.4. The FMRI images were imported into a surgical neuronavigational system (Medtronics™). This portable system includes a wireless stylus whose position in 3D space can be viewed directly on a built-in screen. Usually, the patients anatomical MRI is displayed on the screen and the stylus is used to help guide the neurosurgeon during surgery. In this study, the imported FMRI images were overlaid onto the high-resolution anatomical images, and the two could be simultaneously viewed on screen during surgery. With the help of the stylus, it was possible to accurately locate the areas of significant FMRI activation *in*the brain during surgery. In order to test the validity of the FMRI findings, several cortical sites were electrically stimulated and the patients response was observed. The distance between the areas deemed active via intraoperative stimulation and those found via FMRI was then calculated.

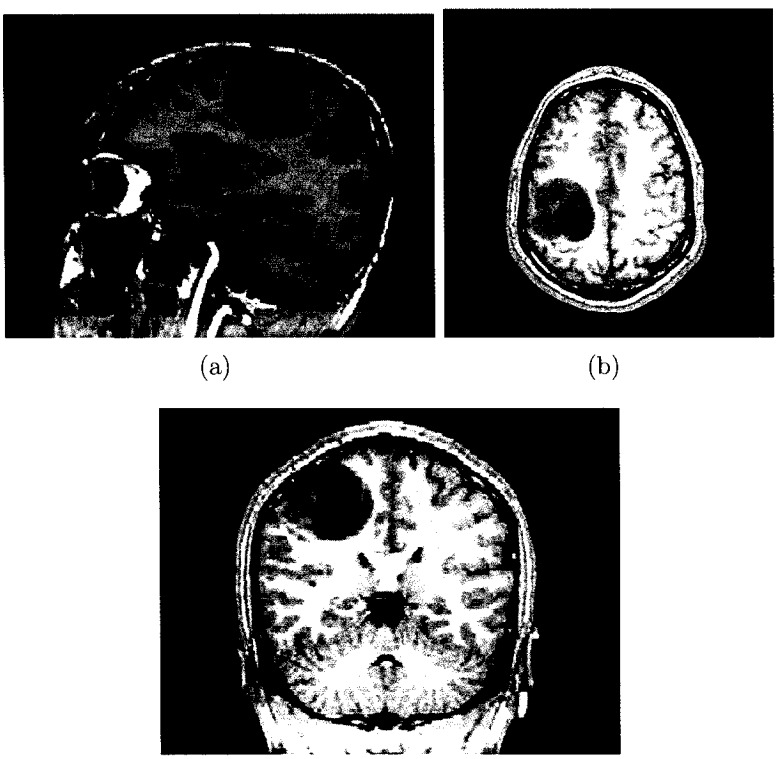

Figure A.1: Sagittal (a), axial (b) and coronal (c) MRI slices of a patient diagnosed with a tumor in and around the motor cortex.

A.2.1 Experimental tasks

As shown in the patients anatomical MRI (figure A.1), the most inferior portion of the tumor was near Brodmann's area 44 & 45 (language center). The most superior portion of the tumor was near Brodmann's area 1-6 (sensory & motor center). In order to investigate whether the tumor affected the functionality of these regions, FMRI using language, motor and sensory tasks were employed. These tasks are described below.

A.2.2 Speech & Language

As shown in the patient's anatomical MRI (figure A.1), the anterior portion of the tumor bordered on Brodmann's' area 44 & 45. This is otherwise referred to as *Broca's* area (figure A.2). This area was first identified by Broca in 1862 [156] when one of his patients could understand speech but was unable to speak. The approximate location of Broca's area is in the inferior frontal gyrus of the frontal lobe of the cortex. Damage to Broca's area (Broca's aphasia) can result in various speech limitations such as preventing a person from producing speech, words not being properly formed and speech that is slow and slurred. Prior to surgery, FMRI scans using two language tasks were employed to chart functional language areas in the vicinity of the tumor. In the first task, the patient was shown random letters that were displayed on the screen for 30 seconds. During this time, the subject was instructed to think of words that started with that letter. The second was a sentence verification task where the patient was asked to mentally detect sentence anomalies.

A.2.3 Motor & Sensory

The bulk of the tumor was in and around the area of the primary somatosensory cortex (Brodmann's areas 1-6) which consists of motor and sensory control. The motor cortex is defined by the precentral gyrus, which is almost similar to Brodmann's areas 4 (figure A.2). The presensory and secondary sensory (sensory association) areas are located behind the postcentral gyrus (Brodmann area 1). The motor cortex was found by instructing the patient to make sequential finger tapping movements in either hand while the other remained stationary. The location of the sensory area

was found by lightly poking the palms of the patients left and right hands.

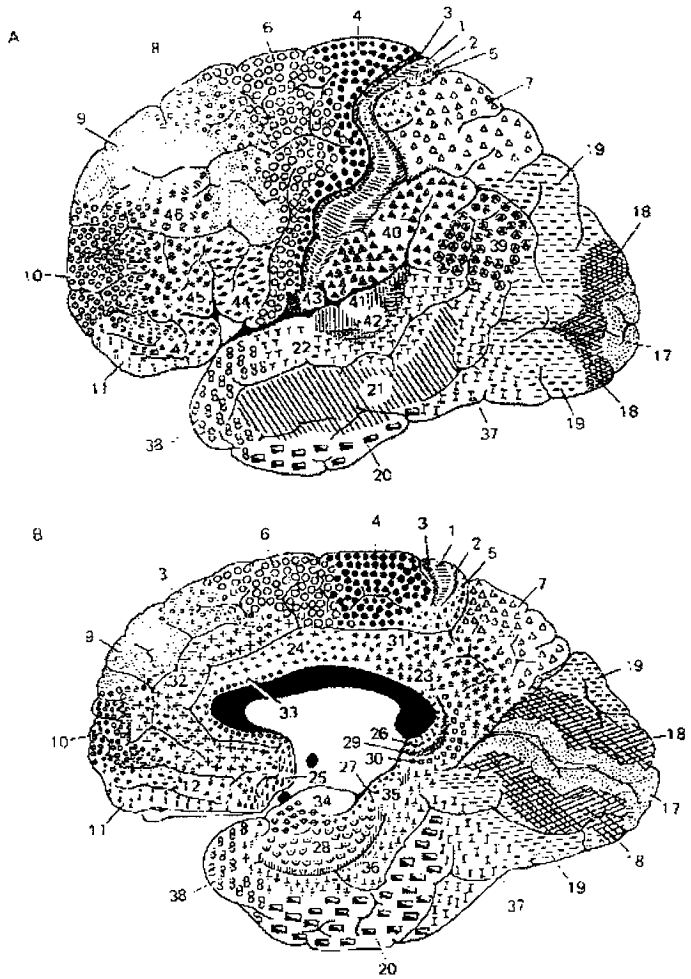

Figure A.2: Both Broca's area (area 44 & 45) and the primary somatosensory cortex (area 1, 2 & 3) were stimulated in a patient with a tumor near these regions. Taken from [90].

A.3 FMRI Results

A.3.1 Speech

All FMRI datasets were fully analyzed for viewing within 4-5 minutes after each experiment while the patient remained in the MRI scanner. FMRI activation sites in response to the language tasks are shown in figure A.3. The activation was divided

into two separate, yet equally active regions. The FMRI response from the first language task peaked in an area close to to the anterior periphery of the tumor. The second language task resulted in an activation near the anterior portion of the frontal lobe, quite removed from the tumor.

Figure A.3: Axial slice showing the most significant FMRI activity ($p \leq 10^{-4}$) in response to two language tasks (see text for description of language tasks). Both areas of functional activity are in good agreement with the location of Broca's area

A.3.2 Motor & Sensory

FMRI results to motor and sensory stimulation are shown in figure A.4. In the motor task involving the right hand, the strongest response was found slightly posterior and lateral to the tumor. A similar, yet weaker FMRI response was found in the sensory task. The locations of both the peak motor and sensory responses are slightly posterior than would be expected in a healthy subject. This indicates that cortical re-arrangement may have been a factor. During left hand stimulation, the location of the peak FMRI responses from motor and sensory tasks were highly symmetric to the peak FMRI response obtained during right hand stimulation. No significant activation from either task was found inside the tumor.

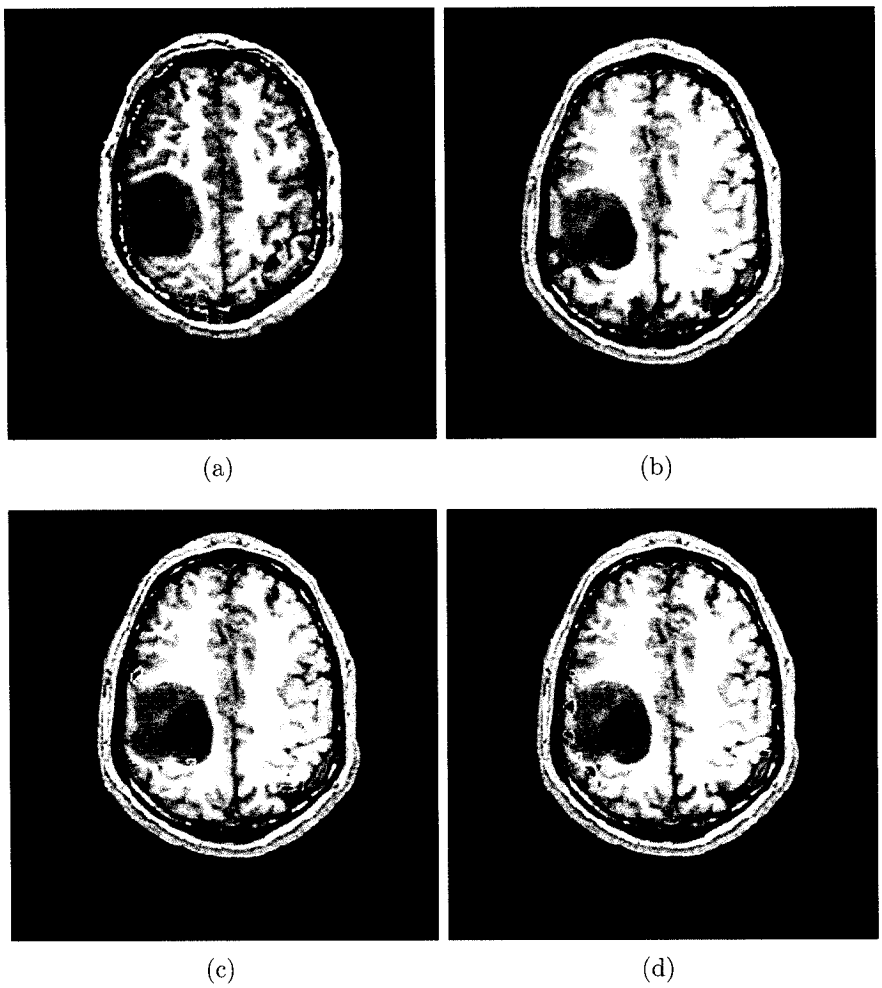

Figure A.4: FMRI activation maps showing the dominant **+BOLD** response during (a) left and (b) right finger tapping tasks, and (c) left and (d) right sensory tasks (see text for details). Maps are thresholded to $p \leq 10^{-4}$.

A.4 Neurosurgery results

Initial intraoperative mapping of cortical functionality was done on the cortical surface, prior to tumor resection. An example of the cortical surface being stimulated is shown in figure A.5.

Figure A.5: The cortical surface being electrically stimulated.

With the area surrounding the tumor exposed, the patient was asked to tap his fingers while the cortex was stimulated. When the patient was not able to move his fingers, the corresponding cortical area was labelled with an 'M' (motor). An 'S' (sensory) was used to label the area corresponding to when the patient reported feeling 'pins and needles' in this right hand. An 'L' (language) was used to identify the area which, upon stimulation, caused the patient's speech to become slightly interrupted and slurred. Once the tumor had been resected, the language area was again identified by stimulating an area (marked by an 'I') that caused the patients speech to become even more slowed, slurred and interrupted. The motor, sensory and language areas that responded to electrical stimulation prior to resection are shown

in figure A.6. A more accurate location of the language area was found after resection

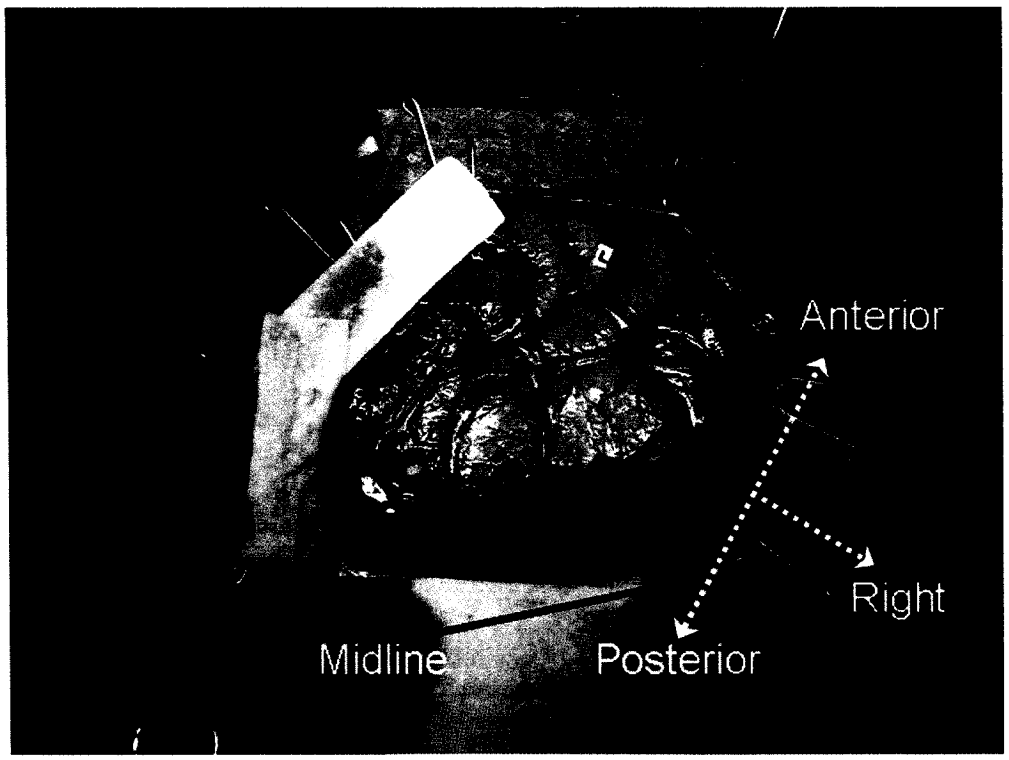

Figure A.6: Cortical areas representing motor (m), sensory (s) and language (l) centers that responded to electrical stimulation. The black arrow points to the approximate location of the midline (dashed white arrow). Anterior, posterior and right direction are also shown.

is shown in figure A.7. A more detailed look of how well the FMRI motor, sensory and language areas correlated with the intraoperative stimulation is shown in figures A.8, A.9 and A.10, respectively.

A.5 Discussion

The language, motor and sensory areas found via FMRI are similar to the FMRI findings obtained by Hirsch et al. involving a patient with a tumor similar to the one in this study [157]. However, owing to the differences in the orientations of the acquired slices, Hirsch et al. were unable to make a precise comparison between FMRI and intraoperative findings. Instead, the surgeon judged the correspondence between

Figure A.7: The 'I' corresponds to the deeper language area.

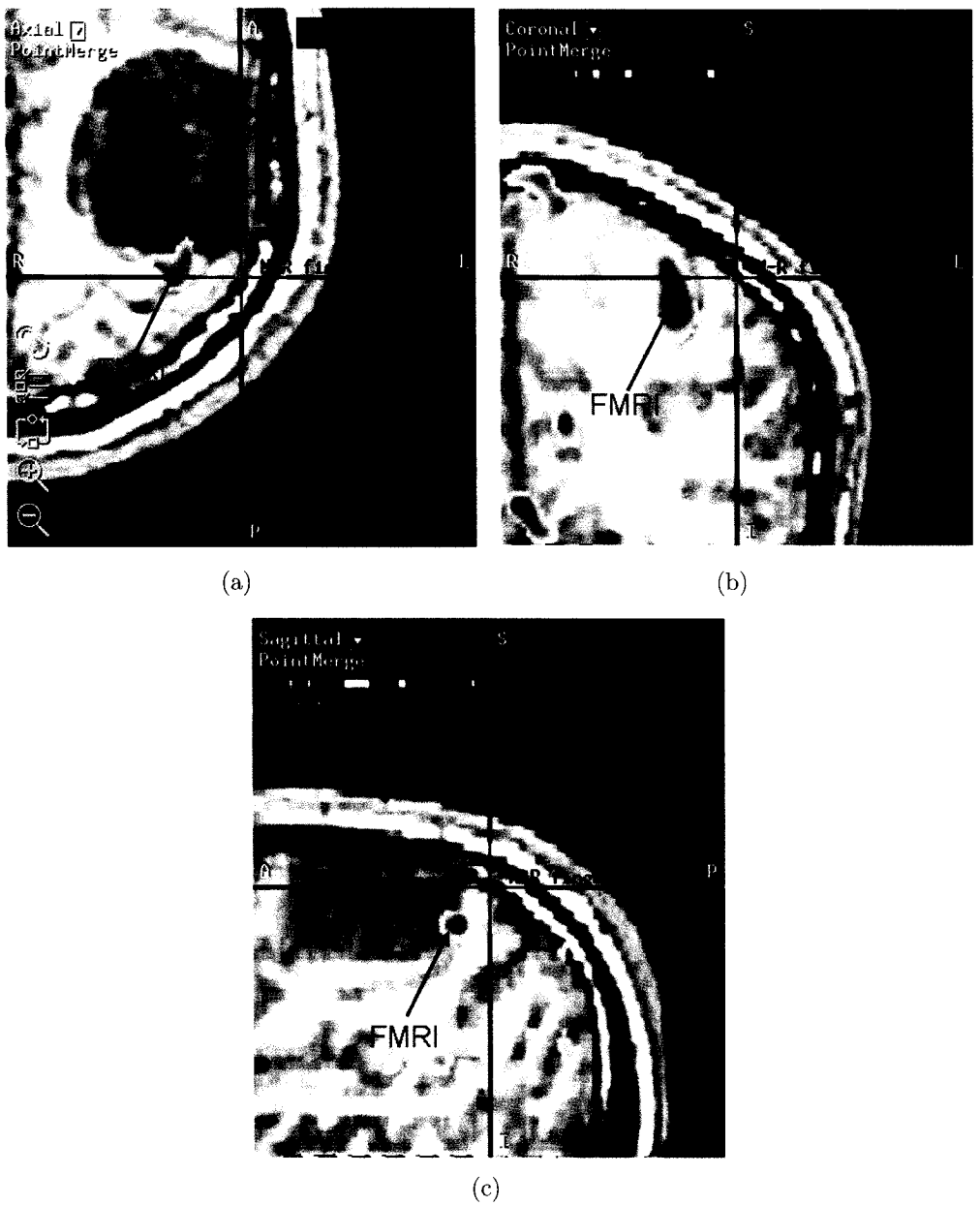

Figure A.8: Axial (a), coronal, (b) and sagittal (c) FMRI images after they have been imported into the neuronavigational system. The red crosshair points to the site where, upon electrical stimulation (5.5 mA) the patient experienced arrested finger tapping. In (a) and (b), the dark spot to the left of the crosshair (in (c), the dark spot is below the crosshair) represents the peak FMRI response obtained during the motor task. The distance between the FMRI and crosshair was less than 1cm.

(a) (b)

(c)

Figure A.9: Axial (a), coronal, (b) and sagittal (c) FMRI images after they have been imported into the neuronavigational system. The red crosshair points to the site where, upon electrical stimulation (5.5 mA) the patient experienced a tingling sensation in the right hand. In (a), the dark spot to the left of the crosshair represents the peak FMRI response obtained during the sensory task. The distance between the FMRI and crosshair was less than 1cm.

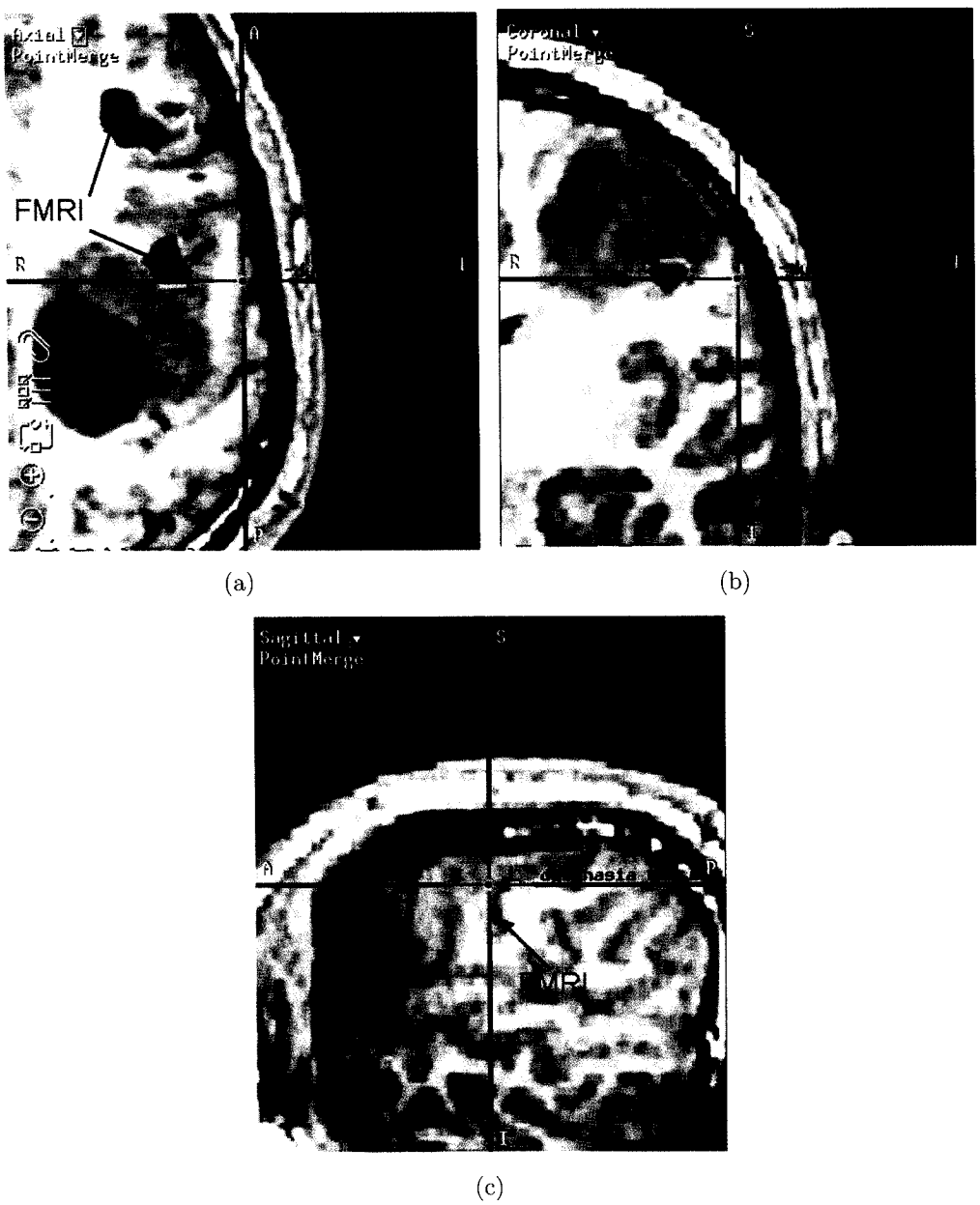

(a) (b)

(c)

Figure A.10: Axial (a), coronal, (b) and sagittal (c) FMRI images after they have been imported into the neuronavigational system. The red crosshair points to the site where, upon electrical stimulation (6.5 mA) the patient experienced a significant loss in speech ability (dysphasia). This area was obtained after resection of the tumor was complete. In (a) and (b), the dark spot to the left of the crosshair represents the peak FMRI response obtained during the second language task. The distance between the FMRI and crosshair was less than 1cm.

FMRI and intraoperative stimulation based on photographs taken during surgery. In our study, the FMRI images were directly imported into the neuronavigational system used during neurosurgery. We were therefore able to directly identify these FMRI and intraoperative locations on the patients structural MRI and better evaluate the correspondence between the two measures.

Overall, the location of the peak FMRI response correlated quite well with cortical areas responding to electrical stimulation. There seemed to be no difference between the level of accuracy between the more superficial motor and sensory areas and the deeper language center. The FMRI COA for motor, sensory and language tasks were less than 1 cm away from their respective areas found via electrical stimulation. Seeing as this was the first time FMRI was used as pre-operative mapping at this institution, this level of accuracy is quite remarkable. In fact, it should be noted that the patient suffered no significant speech impairment following surgery, concluding that no surgical damage was done to the important speech areas of the brain. This verification of FMRI localization significantly increases the reliability of the FMRI findings presented earlier in the thesis. To assist in further research in this area, we suggest that the following points are implemented:

- It would be advantageous to more accurately calculate the distance between the FMRI COA and electrically stimulated site. This could be achieved by noting the coordinates of the FMRI COA after the images have been loaded into the neuronavigational system. During neurosurgery, the x, y, & z coordinates of the cortical region that is stimulated can also be noted, and the distance can be calculated.

- There may exist a limiting SNR at which an optimal FMRI location accuracy is achieved. It is possible that this level of accuracy can be attained in a shorter time than taken in this investigation. It would therefore be advantageous to observe changes in FMRI COA as a function of the SNR.

- Once limiting SNR from the previous point is found, it may be advantageous to use a smaller voxel size, particularly in the inferior-superior direction.

- The neuronavigational system used during neurosurgery should be capable of accepting colour images. This way, the FMRI activation spots would appear

brighter and easier to distinguish from the underlying black and white anatomical structures.

A.6 Conclusion

Since neurosurgery relies on a precise delineation of the structural and functional aspects of the brain, the role for FMRI in neurosurgical planning is potentially very significant. The results presented here illustrate the potential advantage of FMRI for surgical treatment of brain tumors. Moreover, the accuracy achieved with a relatively short analysis time (4-5 minutes per FMRI experiment) shows the advantage of using the FMRI protocol developed in this thesis for urgent clinical cases. These findings also demonstrate the importance of FMRI as a pre-operative tool when the presence of a tumor alters the expected location of a function, or when the location of the tumor is in an area with an uncertain function such as various language, motor or sensory-related processes.

A.7 Acknowledgement

Special thanks goes to Ron Hill for his assistance and support in this study.

Bibliography

[1] R. M. Gulrajani. *Bioelectricity and Biomagnetism.* Wiley, 1998.

[2] F. H. Lopes de Silva and A. Van Rotterdam. Biophysical aspects of eeg and meg generation. In E Neidermeyer and F. H. Lopes da Silva, editors, *Electroencephalography: Basic Principles, clinical applications and related fields*, pages 15–28. Urban & Schwarzenberg, Baltimore, 1987.

[3] W. W. Orrison, J. D. Lewine, J. A. Sanders, and M. F. Hartshorne. *Functional Brain Imaging.* Moseby, St. Louis, 1995.

[4] R. J. Speckmann and C. E. Elger. *Introduction to the neurophysiological basis of the EEG and DC potentials. In: Niedermeyer E and Lopes da Silva F (eds), Electroencephalography. Basic Principles, Clinical Applications and Related Fields.* Urban and Schwarzenberg, 1987.

[5] T. Allison, G. McCarthy, C. C. Wood, and S. J. Jones. Potentials evoked in human and monkey cerebral cortex by stimulation of the median nerve. A review of scalp and intracranial recordings. *Brain*, 114 (Pt 6):2465–2503, Dec 1991.

[6] J. C. Eccles. Interpretation of action potentials in the cerebral cortex. *Electroencephalography: Clinical Neurophysiology*, 3:449 – 464, 1951.

[7] F. H. Lopes da Silva. Neural mechanisms underlying brain waves:from neural membranes to networks. *Electroencephalography: Clinical Neurophysiology*, 79:81 – 93, 1991.

[8] A. J. Rockel, R. W. Hiorns, and T. P. Powel. The basic nonouniformity in structure of the neocortex. *Brain*, 103:22 – 41, 1980.

[9] P. H. Schimpf, C. Ramon, and J. Haueisen. Dipole models for the EEG and MEG. *IEEE Trans Biomed Eng*, 49(5):409–418, May 2002.

[10] J. C. de Munck, B. W. van Dijk, and H. Spekreijse. Mathematical dipoles are adequate to describe realistic generators of human brain activity. *IEEE Trans Biomed Eng*, 35(11):960–966, Nov 1988.

[11] R. Plonsey and R. C. Barr. *Bioelectricity.* Kluwer Academic/Plenumm Press, 1988.

[12] C. M. Michel, M. M. Murray, G. Lantz, S. Gonzalez, L. Spinelli, and R. Grave de Peralta. EEG source imaging. *Clin Neurophysiol*, 115(10):2195–2222, Oct 2004.

[13] S. Thees, F. Blankenburg, B. Taskin, G. Curio, and A. Villringer. Dipole source localization and fMRI of simultaneously recorded data applied to somatosensory categorization. *Neuroimage*, 18(3):707–719, Mar 2003.

[14] J. S. Ebersole. EEG source modeling. The last word. *J Clin Neurophysiol*, 16(3):297–302, May 1999. Editorial.

[15] R. D. Pascual-Marqui, C. M. Michel, and D. Lehmann. Low resolution electromagnetic tomography: a new method for localizing electrical activity in the brain. *Int J Psychophysiol*, 18(1):49–65, Oct 1994. Clinical Trial.

[16] R. J. Ilmoniemi. Models of source currents in the brain. *Brain Topogr*, 5(4):331–336, Summer 1993.

[17] M. S. Hamalainen and R. J. Ilmoniemi. Interpreting magnetic fields of the brain: minimum norm estimates. *Med Biol Eng Comput*, 32(1):35–42, Jan 1994.

[18] R. G. de Peralta Menendez, M. M. Murray, and S. L. G. Andino. Improving the performance of linear inverse solutions by inverting the resolution matrix. *IEEE Trans Biomed Eng*, 51(9):1680–1683, Sep 2004. Evaluation Studies.

[19] C. A. Malcolm, D. L. McCulloch, and A. J. Shepherd. Pattern-reversal visual evoked potentials in infants: gender differences during early visual maturation. *Dev Med Child Neurol*, 44(5):345–351, May 2002. Clinical Trial.

[20] V. L. Towle, A. Moskowitz, S. Sokol, and B. Schwartz. The visual evoked potential in glaucoma and ocular hypertension: effects of check size, field size, and stimulation rate. *Invest Ophthalmol Vis Sci*, 24(2):175–183, Feb 1983.

[21] M. Nakamura, R. Kakigi, T. Okusa, M. Hoshiyama, and K. Watanabe. Effects of check size on pattern reversal visual evoked magnetic field and potential. *Brain Res*, 872(1-2):77–86, Jul 2000. Clinical Trial.

[22] J. R. Brannan, H. A. Solan, A. P. Ficarra, and E. Ong. Effect of luminance on visual evoked potential amplitudes in normal and disabled readers. *Optom Vis Sci*, 75(4):279–283, Apr 1998.

[23] V. Zemon, W. Eisner, J. Gordon, J. Grose-Fifer, F. Tenedios, and H. Shoup. Contrast-dependent responses in the human visual system: childhood through adulthood. *Int J Neurosci*, 80(1-4):181–201, 1995.

[24] F. Di Russo, A. Martinez, M. I. Sereno, S. Pitzalis, and S. A. Hillyard. Cortical sources of the early components of the visual evoked potential. *Hum Brain Mapp*, 15(2):95–111, 2002.

[25] H. Shigeto, S. Tobimatsu, T. Yamamoto, T. Kobayashi, and M. Kato. Visual evoked cortical magnetic responses to checkerboard pattern reversal stimulation: a study on the neural generators of N75, P100 and N145. *J Neurol Sci*, 156(2):186–194, Apr 1998.

[26] H. Tabuchi, T. Yokoyama, M. Shimogawara, K. Shiraki, E. Nagasaka, and T. Miki. Study of the visual evoked magnetic field with the m-sequence technique. *Invest Ophthalmol Vis Sci*, 43(6):2045–54, 2002.

[27] M. Onofrj, T. Fulgente, A. Thomas, L. Curatola, M. Peresson, L. Lopez, T. Locatelli, V. Martinelli, and G. Comi. Visual evoked potentials generator model derived from different spatial frequency stimuli of visual field regions and magnetic resonance imaging coordinates of v1, v2, v3 areas in man. *Int J Neurosci*, 83(3-4):213–39, 1995.

[28] C. E. Schroeder, M. Steinschneider, D. C. Javitt, C. E. Tenke, S. J. Givre, A. D. Mehta, G. V. Simpson, J. C. Arezzo, and Jr. Vaughan, H. G. Localization of erp generators and identification of underlying neural processes. *Electroencephalogr Clin Neurophysiol Suppl*, 44:55–75, 1995.

[29] F. Di Russo, S. Pitzalis, G. Spitoni, T. Aprile, F. Patria, D. Spinelli, and S. A. Hillyard. Identification of the neural sources of the pattern-reversal vep. *Neuroimage*, 24(3):874–86, 2005.

[30] S. Noachtar, T. Hashimoto, and H. Luders. Pattern visual evoked potentials recorded from human occipital cortex with chronic subdural electrodes. *Electroencephalogr Clin Neurophysiol*, 88(6):435–46, 1993.

[31] G. Bonmassar, D. P. Schwartz, A. K. Liu, K. K. Kwong, A. M. Dale, and J. W. Belliveau. Spatiotemporal brain imaging of visual-evoked activity using interleaved EEG and fMRI recordings. *Neuroimage*, 13(6 Pt 1):1035–1043, Jun 2001.

[32] P. H. Laarne, M. L. Tenhunen-Eskelinen, J. K. Hyttinen, and H. J. Eskola. Effect of EEG electrode density on dipole localization accuracy using two realistically shaped skull resistivity models. *Brain Topogr*, 12(4):249–254, Summer 2000.

[33] Outi R. M. Ryynanen, Jari A. K. Hyttinen, Paivi H. Laarne, and Jaakko A. Malmivuo. Effect of electrode density and measurement noise on the spatial resolution of cortical potential distribution. *IEEE Trans Biomed Eng*, 51(9):1547–1554, Sep 2004. Evaluation Studies.

[34] G. G. Celesia, R. D. Polcyn, J. E. Holden, R. J. Nickles, J. S. Gatley, and R. A. Koeppe. Visual evoked potentials and positron emission tomographic mapping of regional cerebral blood flow and cerebral metabolism: can the neuronal potential generators be visualized? *Electroencephalogr Clin Neurophysiol*, 54(3):243–56, 1982.

[35] C. E. Schroeder, C. E. Tenke, S. J. Givre, J. C. Arezzo, and H. G. Vaughan. Striate cortical contribution to the surface-recorded pattern-reversal VEP in the alert monkey. *Vision Res*, 31(7-8):1143–1157, 1991.

[36] D. Regan. *Human brain electrophysiology : evoked potentials and evoked magnetic fields in science and medicine.* Elsevier, 1989.

[37] A. Carrington and A. D. McLachlan. *Introduction to Magnetic Resonance.* Chapman and Hall, London, 1967.

[38] R. K. Harris. *Nuclear magnetic resonance spectroscopy.* Pitman Books Ltd, 1983.

[39] G. H. Glover and A. T. Lee. Motion artifacts in fMRI: comparison of 2DFT with PR and spiral scan methods. *Magn Reson Med*, 33(5):624–635, May 1995.

[40] L. Pauling and C. D. Coryell. The Magnetic properties and structure of hemoglobin, oxyhemoglobin and carbonmonoxyhemoglobin. *Proc Natl Acad Sci U S A*, 22(4):210–216, Apr 1936.

[41] L. Pauling. Magnetic properties and structure of oxyhemoglobin. *Proc Natl Acad Sci U S A*, 74(7):2612–2613, Jul 1977.

[42] S. Ogawa, T. M. Lee, A. R. Kay, and D. W. Tank. Brain magnetic resonance imaging with contrast dependent on blood oxygenation. *Proc Natl Acad Sci U S A*, 87(24):9868 – 9872, Dec 1990.

[43] P. A. Bandettini, E. C. Wong, R. S. Hinks, R. S. Tikofsky, and J. S. Hyde. Time course EPI of human brain function during task activation. *Magn Reson Med*, 25(2):390–397, Jun 1992.

[44] K. K. Kwong, J. W. Belliveau, D. A. Chesler, I. E. Goldberg, R. M. Weisskoff, B. P. Poncelet, D. N. Kennedy, B. E. Hoppel, M. S. Cohen, and R. Turner. Dynamic magnetic resonance imaging of human brain activity during primary sensory stimulation. *Proc Natl Acad Sci U S A*, 89(12):5675–5679, Jun 1992.

[45] L. Sokoloff. Relation between physiological function and energy metabolism in the central nervous system. *J Neurochem*, 29(1):13–26, Jul 1977.

[46] P. J. Yarowsky and D. H. Ingvar. Neuronal activity and energy metabolism. *Fed. Proc.*, 40(2):2353–2362, Sep 1981. Evaluation Studies.

[47] M. Erecinska, D. Nelson, and B. Chance. Depolarization-induced changes in cellular energy production. *Proc. Nat. Acad. Sci.*, 88(2):7600–7604, Sep 1991. Evaluation Studies.

[48] R. G. Shulman and D. L. Rothman. Interpreting functional imaging studies in terms of neurtrasnmitter cycling. *Proc. Nat. Acad. Sci.*, 95(2):11993–11998, Sep 1998. Evaluation Studies.

[49] R. J. Seitz and P. E. Roland. Vibratory stimulation increases and decreases in regional blood flow and oxidative metabolism: a positron emission tomography (PET) study. *Acta. Neurologica Scandinavica*, 20(2):740–748, Sep 1992. Evaluation Studies.

[50] H. Fujita, H. Kuwabara, D. C. Reutens, and A. Gjedde. Oxygen consumption of cerebral cortex fails to increase during continued vibrotactile stimulation. *Journal of cerebral flow and metabolism*, 19(2):266–281, Sep 1999. Evaluation Studies.

[51] P. T. Fox and M. E. Raichle. Focal physiological uncoupling of cerebral blood flow and oxidative metabolism during somatosensory stimulation in human subjects. *Proc Natl Acad Sci U S A*, 83(4):1140–1144, Feb 1986.

[52] P. T. Fox, M. E. Raichle, M. A. Mintun, and C. Dence. Nonoxidative glucose consumption during focal physiologic neural activity. *Science*, 241(4864):462–464, Jul 1988.

[53] S. Ogawa, R. S. Menon, S. G. Kim, and K. Ugurbil. On the characteristics of functional magnetic resonance imaging of the brain. *Annu Rev Biophys Biomol Struct*, 27:447–474, 1998.

[54] J. L. Boxerman, P. A. Bandettini, K. K. Kwong, J. R. Baker, T. L. Davis, B. R. Rosen, and R. M. Weisskoff. The intravascular contribution to fMRI signal change: Monte Carlo modeling and diffusion-weighted studies in vivo. *Magn Reson Med*, 34(1):4–10, Jul 1995.

[55] R. B. Buxton and L. R. Frank. A model for the coupling between cerebral blood flow and oxygen metabolism during neural stimulation. *J Cereb Blood Flow Metab*, 17(1):64–72, Jan 1997.

[56] J. Frahm, G. Kruger, K. D. Merboldt, and A. Kleinschmidt. Dynamic uncoupling and recoupling of perfusion and oxidative metabolism during focal brain activation in man. *Magn Reson Med*, 35(2):143–148, Feb 1996.

[57] R. B. Buxton, E. C. Wong, and L. R. Frank. Dynamics of blood flow and oxygenation changes during brain activation: the balloon model. *Magn Reson Med*, 39(6):855–864, Jun 1998.

[58] N. K. Logothetis, H. Guggenberger, S. Peled, and J. Pauls. Functional imaging of the monkey brain. *Nat Neurosci*, 2(6):555–562, Jun 1999.

[59] M. Lauritzen. Reading vascular changes in brain imaging: is dendritic calcium the key? *Nat Rev Neurosci*, 6(1):77–85, Jan 2005.

[60] D. Waldvogel, P. van Gelderen, W. Muellbacher, U. Ziemann, I. Immisch, and M. Hallett. The relative metabolic demand of inhibition and excitation. *Nature*, 406(6799):995–998, Aug 2000. Clinical Trial.

[61] R. Wenzel, P. Wobst, H. H. Heekeren, K. K. Kwong, S. A. Brandt, M. Kohl, H. Obrig, U. Dirnagl, and A. Villringer. Saccadic suppression induces focal hypooxygenation in the occipital cortex. *J Cereb Blood Flow Metab*, 20(7):1103–10, 2000.

[62] A. Shmuel, E. Yacoub, J. Pfeuffer, P. F. Van de Moortele, G. Adriany, X. Hu, and K. Ugurbil. Sustained negative bold, blood flow and oxygen consumption response and its coupling to the positive response in the human brain. *Neuron*, 36(6):1195–210, 2002.

[63] A. T. Smith, K. D. Singh, and M. W. Greenlee. Attentional suppression of activity in the human visual cortex. *Neuroreport*, 11(2):271–7, 2000.

[64] A. T. Smith, A. L. Williams, and K. D. Singh. Negative bold in the visual cortex: evidence against blood stealing. *Hum Brain Mapp*, 21(4):213–20, 2004.

[65] A. Shmuel, M. Augath, E. Rounis, N. K. Logothetis, and S. Smirknakis. Negative bold repsonse ipsilateral to the visual stimulus: origin is not blood stealing. *Neuroimage*, 19(Suppl)(309), 2003b.

[66] B. Stefanovic, J. M. Warnking, and G. B. Pike. Hemodynamic and metabolic responses to neuronal inhibition. *Neuroimage*, 22(2):771–8, 2004.

[67] A. T. Lee, G. H. Glover, and C. H. Meyer. Discrimination of large venous vessels in time-course spiral blood-oxygen-level-dependent magnetic-resonance functional neuroimaging. *Magn Reson Med*, 33(6):745–754, Jun 1995.

[68] J. Frahm, K. D. Merboldt, W. Hanicke, A. Kleinschmidt, and H. Boecker. Brain or vein–oxygenation or flow? On signal physiology in functional MRI of human brain activation. *NMR Biomed*, 7(1-2):45–53, Mar 1994.

[69] S. Lai, A. L. Hopkins, E. M. Haacke, D. Li, B. A. Wasserman, P. Buckley, L. Friedman, H. Meltzer, P. Hedera, and R. Friedland. Identification of vascular structures as a major source of signal contrast in high resolution 2D and 3D functional activation imaging of the motor cortex at 1.5T: preliminary results. *Magn Reson Med*, 30(3):387–392, Sep 1993.

[70] R. S. Menon, S. Ogawa, D. W. Tank, and K. Ugurbil. Tesla gradient recalled echo characteristics of photic stimulation-induced signal changes in the human primary visual cortex. *Magn Reson Med*, 30(3):380–386, Sep 1993.

[71] E. Yacoub, J. Shmuel, A.and Pfeuffer, P. F. Van De Moortele, G. Adriany, P. Andersen, J. T. Vaughan, H. Merkle, K. Ugurbil, and X. Hu. Imaging brain function in humans at 7 Tesla. *Magn Reson Med*, 45(4):588–594, Apr 2001.

[72] E. R. Kandel, J. H. Schwartz, and T. M. Jessel. *Principles of Neural Science (4th Ed.)*. McGraw-Hill, 1991.

[73] D. S. Kim, I. Ronen, C. Olman, S. G. Kim, K. Ugurbil, and L. J. Toth. Spatial relationship between neuronal activity and BOLD functional MRI. *Neuroimage*, 21(3):876–885, Mar 2004.

[74] N. K. Logothetis. The underpinnings of the BOLD functional magnetic resonance imaging signal. *J Neurosci*, 23(10):3963–3971, May 2003.

[75] N. K. Logothetis and J. Pfeuffer. On the nature of the BOLD fMRI contrast mechanism. *Magn Reson Imaging*, 22(10):1517–1531, Dec 2004.

[76] C. A. Marsan. Electrical activity of the brain: slow waves and neuronal activity. *Isr Med J*, 20:104–117, Jan 1965.

[77] G. H. Fromm and H. W. Bond. Slow changes in the electrocortigram and the activity of cortical neurons. *Electroencephalogr Clin Neurophysiol*, 17:520–523, Nov 1964.

[78] G. H. Fromm and H. W. Bond. The relationship between neuron activity and cortical steady potentials. *Electroencephalogr Clin Neurophysiol*, 22(2):159–166, Feb 1967.

[79] A. Kamondi, L. Acsady, X. J. Wang, and G. Buzsaki. Theta oscillations in somata and dendrites of hippocampal pyramidal cells in vivo: activity-dependent phase-precession of action potentials. *Hippocampus*, 8(3):244–261, 1998.

[80] K. Thomsen, N. Offenhauser, and M. Lauritzen. Principal neuron spiking: neither necessary nor sufficient for cerebral blood flow in rat cerebellum. *J Physiol*, 560(Pt 1):181–189, Oct 2004.

[81] L. Gold and M. Lauritzen. Neuronal deactivation explains decreased cerebellar blood flow in response to focal cerebral ischemia or suppressed neocortical function. *Proc Natl Acad Sci U S A*, 99(11):7699–7704, May 2002.

[82] N. A. Nielsen and M. Lauritzen. Coupling and uncoupling of activity-dependent increases of neuronal activity and blood flow in rat somatosensory cortex. *J Physiol*, 533(Pt 3):773–785, Jun 2001.

[83] N. K. Logothetis, J. Pauls, M. Augath, T. Trinath, and A. Oeltermann. Neurophysiological investigation of the basis of the fMRI signal. *Nature*, 412(6843):150–157, Jul 2001.

[84] O. J. Arthurs and S. J. Boniface. What aspect of the FMRI BOLD signal best reflects the underlying electrophysiology in human somatosensory cortex? *Clinical Neurophysiology*, 114:1203–1209, Mar 2003.

[85] S. P. Ahlfors, G. V. Simpson, A. M. Dale, J. W. Belliveau, A. K. Liu, A. Korvenoja, J. Virtanen, M. Huotilainen, R. B. Tootell, H. J. Aronen, and R. J. Ilmoniemi. Spatiotemporal activity of a cortical network for processing visual

motion revealed by MEG and fMRI. *J Neurophysiol*, 82(5):2545–2555, Nov 1999.

[86] B. Opitz, A. Mecklinger, D. Y. Von Cramon., and F. Kruggel. Combining electrophysiological and hemodynamic measures of the auditory oddball. *Psychophysiology*, 36(1):142–147, Jan 1999. Clinical Trial.

[87] S. Vanni, J. Warnking, M. Dojat, C. Delon-Martin, J. Bullier, and C. Segebarth. Sequence of pattern onset responses in the human visual areas: an fmri constrained vep source analysis. *Neuroimage*, 21(3):801–17, 2004.

[88] D. Vitacco, D. Brandeis, R. Pascual-Marqui, and E. Martin. Correspondence of event-related potential tomography and functional magnetic resonance imaging during language processing. *Hum Brain Mapp*, 17(1):4–12, Sep 2002. Clinical Trial.

[89] R. Pascual-Marqui, C. M. Michel, and D. Lehmann. Low resolution electromagnetic tomography: a new method for localizing electrical activity in the brain. *Int J Psychophysiol*, 18:49–65, 1994.

[90] K. Broadmann. *Vergleichende Lokalisationslehre der Grohirnrinde in ihren Prinzipien dargestellt auf Grund des Zellenbaues.* Leipzig: Barth JA., 1909.

[91] J. S. Lund and C. Q. Wu. Local circuit neurons of macaque monkey striate cortex: IV. Neurons of laminae 1-3A. *J Comp Neurol*, 384(1):109–126, Jul 1997.

[92] D. J. Felleman and D. C. Van Essen. Distributed hierarchical processing in the primate cerebral cortex. *Cereb Cortex*, 1(1):1–47, Jan 1991.

[93] J. C. Horton and W. F. Hoyt. The representation of the visual field in human striate cortex. A revision of the classic Holmes map. *Arch Ophthalmol*, 109(6):816–824, Jun 1991.

[94] R. F. Dougherty, V. M. Koch, A. A. Brewer, B. Fischer, J. Modersitzki, and B. A. Wandell. Visual field representations and locations of visual areas V1/2/3 in human visual cortex. *J Vis*, 3(10):586–598, 2003.

[95] J. C. Culham, S. A. Brandt, P. Cavanagh, N. G. Kanwisher, A. M. Dale, and R. B. Tootell. Cortical fMRI activation produced by attentive tracking of moving targets. *J Neurophysiol*, 80(5):2657–2670, Nov 1998.

[96] J. Moran and R. Desimone. Selective attention gates visual processing in the extrastriate cortex. *Science*, 229(4715):782–784, Aug 1985.

[97] D. Chawla, G. Rees, and K. J. Friston. The physiological basis of attentional modulation in extrastriate visual areas. *Nat Neurosci*, 2(7):671–676, Jul 1999.

[98] J. L. Gallant, R. E. Shoup, and J. A. Mazer. A human extrastriate area functionally homologous to macaque V4. *Neuron*, 27(2):227–235, Aug 2000. Case Reports.

[99] D. Cohen, B. N. Cuffin, K. Yunokuchi, R. Maniewski, C. Purcell, G. R. Cosgrove, J. Ives, J. G. Kennedy, and D. L. Schomer. MEG versus EEG localization test using implanted sources in the human brain. *Ann Neurol*, 28(6):811–817, Dec 1990.

[100] B. N. Cuffin, D. Cohen, K. Yunokuchi, R. Maniewski, C. Purcell, G. R. Cosgrove, J. Ives, J. Kennedy, and D. Schomer. Tests of EEG localization accuracy using implanted sources in the human brain. *Ann Neurol*, 29(2):132–138, Feb 1991.

[101] A. S. Ferguson and G. Stroink. Factors affecting the accuracy of the boundary element method in the forward problem–I: Calculating surface potentials. *IEEE Trans Biomed Eng*, 44(11):1139–1155, Nov 1997.

[102] E. Menninghaus, B. Lutkenhoner, and S. L. Gonzalez. Localization of a dipolar source in a skull phantom: realistic versus spherical model. *IEEE Trans Biomed Eng*, 41(10):986–989, Oct 1994.

[103] B. J. Roth, M. Balish, A. Gorbach, and S. Sato. How well does a three-sphere model predict positions of dipoles in a realistically shaped head? *Electroencephalogr Clin Neurophysiol*, 87(4):175–184, Oct 1993.

[104] M. Fuchs, R. Drenckhahn, H. A. Wischmann, and M. Wagner. An improved boundary element method for realistic volume-conductor modeling. *IEEE Trans Biomed Eng*, 45(8):980–997, Aug 1998.

[105] M. Fuchs, M. Wagner, and J. Kastner. Boundary element method volume conductor models for eeg source reconstruction. *Clin Neurophysiol*, 112(8):1400–7, 2001.

[106] V. Menon, J. M. Ford, K. O. Lim, G. H. Glover, and A. Pfefferbaum. Combined event-related fMRI and EEG evidence for temporal-parietal cortex activation during target detection. *Neuroreport*, 8(14):3029–3037, Sep 1997. Clinical Trial.

[107] C. Mulert, L. Jager, R. Schmitt, P. Bussfeld, O. Pogarell, H. J. Moller, G. Juckel, and U. Hegerl. Integration of fmri and simultaneous eeg: towards a comprehensive understanding of localization and time-course of brain activity in target detection. *Neuroimage*, 22(1):83–94, 2004.

[108] B. Opitz, A. Mecklinger, D. Y. Von Cramon, and F. Kruggel. Combining electrophysiological and hemodynamic measures of the auditory oddball. *Psychophysiology*, 36(1):142–7, 1999.

[109] F. Kruggel, C. J. Wiggins, C. S. Herrmann, and D. Y. von Cramon. Recording of the event-related potentials during functional MRI at 3.0 Tesla field strength. *Mag Res Med*, 44:277–282, 2000.

[110] C. Grimm, A. Schreiber, R. Kristeva-Feige, T. Mergner, J. Hennig, and C. H. Lucking. A comparison between electric source localisation and fmri during somatosensory stimulation. *Electroencephalogr Clin Neurophysiol*, 106(1):22–9, 1998.

[111] B. Vanrumste, G. Van Hoey, R. Van de Walle, M. R. D'Have, I. A. Lemahieu, and P. A. Boon. Comparison of performance of spherical and realistic head models in dipole localization from noisy eeg. *Med Eng Phys*, 24(6):403–18, 2002.

[112] K. Whittingstall, G. Stroink, L. Gates, J. F. Connolly, and A. Finley. Effects of dipole position, orientation and noise on the accuracy of eeg source localization. *Biomed Eng Online*, 2(1):14, 2003.

[113] S. Arroyo, R. P. Lesser, W. T. Poon, W. R. Webber, and B. Gordon. Neuronal generators of visual evoked potentials in humans: visual processing in the human cortex. *Epilepsia*, 38(5):600–10, 1997.

[114] S. Kurita-Tashima, S. Tobimatsu, M. Nakayama-Hiromatsu, and M. Kato. Effect of check size on the pattern reversal visual evoked potential. *Electroencephalogr Clin Neurophysiol*, 80(3):161–6, 1991.

[115] K. V. Thilo, A. Kleinschmidt, and M. A. Gresty. Perception of self-motion from peripheral optokinetic stimulation suppresses visual evoked responses to central stimuli. *J Neurophysiol*, 90(2):723–30, 2003.

[116] B. Fortune and D. C. Hood. Conventional pattern-reversal VEPs are not equivalent to summed multifocal VEPs. *Invest Ophthalmol Vis Sci*, 44(3):1364–1375, Mar 2003.

[117] G. H. Klem, H. O. Luders, H. H. Jasper, and C. Elger. The ten-twenty electrode system of the international federation. the international federation of clinical neurophysiology. *Electroencephalogr Clin Neurophysiol Suppl*, 52:3–6, 1999.

[118] J. V. Odom, M. Bach, C. Barber, M. Brigell, M. F. Marmor, A.P. Tormene, and G. E. Holder. Visual evoked potentials standard (2004). *Doc Ophthalmol*, 108(2):115–123, Mar 2004.

[119] S. D. Slotnick, S. A. Klein, T. Carney, E. Sutter, and S. Dastmalchi. Using multi-stimulus vep source localization to obtain a retinotopic map of human primary visual cortex. *Clin Neurophysiol*, 110(10):1793–800, 1999.

[120] J. Steger, K. Imhof, J. Denoth, R. D. Pascual-Marqui, H. C. Steinhausen, and D. Brandeis. Brain mapping of bilateral visual interactions in children. *Psychophysiology*, 38(2):243–53, 2001.

[121] G. H. Glover. Simple analytic spiral K-space algorithm. *Magn Reson Med*, 42(2):412–415, Aug 1999.

[122] D. C. Noll, J. D. Cohen, C. H. Meyer, and W. Schneider. Spiral k-space mr imaging of cortical activation. *J Magn Reson Imaging*, 5(1):49–56, 1995.

[123] R. W. Cox. AFNI: Software for analysis and visualization of functional magnetic resonance neuroimages. *Computers and Biomedical Research*, 29:162–173, 1996.

[124] M. Singh, S. Kim, and T. S. Kim. Correlation between BOLD-fMRI and EEG signal changes in response to visual stimulus frequency in humans. *Magn Reson Med*, 49(1):108–114, Jan 2003.

[125] A. M. Howseman, D. A. Porter, C. Hutton, O. Josephs, and R. Turner. Blood oxygenation level dependent signal time courses during prolonged visual stimulation. *Magn Reson Imaging*, 16(1):1–11, 1998.

[126] G. Kruger, A. Kleinschmidt, and J. Frahm. Stimulus dependence of oxygenation-sensitive mri responses to sustained visual activation. *NMR Biomed*, 11(2):75–9, 1998.

[127] S. Tomita, S. Kajihara, Y. Kondo, Y. Yoshida, K. Shibata, and H. Kado. Influence of head model in biomagnetic source localization. *Brain Topogr*, 8(3):337–40, 1996.

[128] R. Spehlmann, R. A. Gross, S. U. Ho, J. E. Leestma, and K. A. Norcross. Visual evoked potentials and postmortem findings in a case of cortical blindness. *Ann Neurol*, 2(6):531–534, Dec 1977. Case Reports.

[129] G. G. Celesia, D. Bushnell, S. C. Toleikis, and M. G. Brigell. Cortical blindness and residual vision: is the "second" visual system in humans capable of more than rudimentary visual perception? *Neurology*, 41(6):862–869, Jun 1991. Case Reports.

[130] S. A. Engel, D. E. Rumelhart, B. A. Wandell, A. T. Lee, G. H. Glover, E. J. Chichilnisky, and M. N. Shadlen. fmri of human visual cortex. *Nature*, 369(6481):525, 1994.

[131] C. Janz, C. Schmitt, O. Speck, and J. Hennig. Comparison of the hemodynamic response to different visual stimuli in single-event and block stimulation fmri experiments. *J Magn Reson Imaging*, 12(5):708–14, 2000.

[132] G. Huiskamp, M. Vroeijenstijn, R. van Dijk, G. Wieneke, and A. C. van Huffelen. The need for correct realistic geometry in the inverse EEG problem. *IEEE Trans Biomed Eng*, 46(11):1281–1287, Nov 1999.

[133] M. Hoshiyama and R. Kakigi. Effects of attention on pattern-reversal visual evoked potentials: foveal field stimulation versus peripheral field stimulation. *Brain Topogr*, 13(4):293–298, Summer 2001.

[134] J. T. Meredith and G. G. Celesia. Pattern-reversal visual evoked potentials and retinal eccentricity. *Electroencephalogr Clin Neurophysiol*, 53(3):243–53, 1982.

[135] H. Ikeda, H. Nishijo, K. Miyamoto, R. Tamura, S. Endo, and T. Ono. Generators of visual evoked potentials investigated by dipole tracing in the human occipital cortex. *Neuroscience*, 84(3):723–39, 1998.

[136] V. Clark, Fan S., and S. A. Hillyard. Identification of early visual evoked potential generators by retinotopic and topographic analyses. *Hum Brain Mapp*, 2:170–187, 1995.

[137] J. Brecelj, R. Kakigi, S. Koyama, and M. Hoshiyama. Visual evoked magnetic responses to central and peripheral stimulation: simultaneous vep recordings. *Brain Topogr*, 10(3):227–37, 1998.

[138] S. P. Ahlfors, R. J. Ilmoniemi, and M. S. Hamalainen. Estimates of visually evoked cortical currents. *Electroencephalogr Clin Neurophysiol*, 82(3):225–36, 1992.

[139] R. N. Weinreb and P. T. Khaw. Primary open-angle glaucoma. *Lancet*, 363(9422):1711–1720, May 2004.

[140] J. W. Howe and K. W. Mitchell. Visual evoked potential changes in chronic glaucoma and ocular hypertension. *Trans Ophthalmol Soc U K*, 105 (Pt 4):457–462, 1986.

[141] Y. H. Yucel, Q. Zhang, R. N. Weinreb, P. L. Kaufman, and N. Gupta. Effects of retinal ganglion cell loss on magno-, parvo-, koniocellular pathways in the lateral geniculate nucleus and visual cortex in glaucoma. *Prog Retin Eye Res*, 22(4):465–481, Jul 2003.

[142] M. A. Snegir. Modifications of visual evoked potentials in patients with glaucoma. *Neurophysiology*, 34(2):52–57, 2002.

[143] V. Parisi. Neural conduction in the visual pathways in ocular hypertension and glaucoma. *Graefes Arch Clin Exp Ophthalmol*, 235(3):136–142, Mar 1997.

[144] C. Damian, M. Iancau, and D. Costache. [The visual evoked potentials in open angle glaucoma]. *Oftalmologia*, 48(1):62–67, 2004.

[145] V. Parisi and M. G. Bucci. Visual evoked potentials after photostress in patients with primary open-angle glaucoma and ocular hypertension. *Invest Ophthalmol Vis Sci*, 33(2):436–442, Feb 1992.

[146] T. Andersson and A. Siden. An analysis of VEP components in optic neuritis. *Electromyogr Clin Neurophysiol*, 35(2):77–85, Mar 1995.

[147] I. Bodis-Wollner, J. R. Brannan, J. Nicoll, S. Frkovic, and L. H. Mylin. A short latency cortical component of the foveal VEP is revealed by hemifield stimulation. *Electroencephalogr Clin Neurophysiol*, 84(3):201–208, May 1992.

[148] A. Miki, T. Nakajima, M. Takagi, M. Shirakashi, and H. Abe. Detection of visual dysfunction in optic atrophy by functional magnetic resonance imaging during monocular visual stimulation. *Am J Ophthalmol*, 122(3):404–415, Sep 1996. Case Reports.

[149] A. T. Toosy, D. J. Werring, G. T. Plant, E. T. Bullmore, D. H. Miller, and A. J. Thompson. Asymmetrical Activation of Human Visual Cortex Demonstrated by Functional MRI with Monocular Stimulation. *Neuroimage*, 14(2):632–641, Sep 2001. Evaluation Studies.

[150] N. N. Sood, P. Basumatary, and H. C. Agarwal. Assessment of visual evoked response in chronic simple glaucoma. *Indian J Ophthalmol*, 35(5-6):274–277, 1987.

[151] A. I. Klistorner, S. L. Graham, and A. Martins. Multifocal pattern electroretinogram does not demonstrate localised field defects in glaucoma. *Doc Ophthalmol*, 100(2-3):155–165, 2000.

[152] C. Hu, L. Wu, D. Z. Wu, and F. Jiang. The multi-channel VEP topographies in patients with late-stage glaucoma. *Yan Ke Xue Bao*, 14(1):21–26, Mar 1998.

[153] A. Ducati, E. Fava, and E. D. Motti. Neuronal generators of the visual evoked potentials: intracerebral recording in awake humans. *Electroencephalogr Clin Neurophysiol*, 71(2):89–99, Mar 1988.

[154] M. Scherg. The number of dipole generators for the p100 vep component. private communication, 2005.

[155] R. B. Tootell, N. Hadjikhani, E. K. Hall, S. Marrett, W. Vanduffel, J. T. Vaughan, and A. M. Dale. The retinotopy of visual spatial attention. *Neuron*, 21(6):1409–1422, Dec 1998.

[156] P. Broca. Remarques sur le siege de la faculte du langage articule, suivies d'une observation d'aphemie (perte de la parole). *Bulletin de la Socit Anatomique*, 1(6):330–357, Apr 1862.

[157] J. Hirsch, M. I. Ruge, K. H. Kim, D. D. Correa, J. D. Victor, N. R. Relkin, D. R. Labar, G. Krol, M. H. Bilsky, M. M. Souweidane, L. M. DeAngelis, and P. H. Gutin. An integrated functional magnetic resonance imaging procedure for preoperative mapping of cortical areas associated with tactile, motor, language, and visual functions. *Neurosurgery*, 47(3):711–721, Sep 2000.